



The Nuclear Shell Model Towards the Drip Lines

B. A. BROWN

*Department of Physics and Astronomy and National Superconducting Cyclotron Laboratory,
Michigan State University, East Lansing, Michigan 48824-1321, USA*

Abstract

Applications of the nuclear shell model to nuclei out to the proton and neutron drip lines are presented. The assumptions and hamiltonians for the mean-field and shell-model configuration mixing models are summarized. The properties discussed include binding energies, separation energies, displacement energies, intruder states, proton and neutron halos, diproton decay, spectroscopic factors, interaction cross sections, E1 and E2 transitions, beta decay, quadrupole moments and magnetic moments.

Contents

1	Introduction	519
2	Magic Numbers	520
2.1	Excited states in even-even nuclei	520
2.2	Single-particle energies and shell gaps	524
3	Model Space and Computations	528
4	Hamiltonians	530
4.1	Introduction	530
4.2	Basic assumptions	531
4.3	The renormalized G matrix	533
4.4	Empirical approaches	533
4.5	Mean-field hamiltonians	537
4.6	The p-shell model space	537
4.7	The sd-shell model space	538
4.8	The pf-shell model space	539
4.9	The s-p-sd-pf-shell model space	540
4.10	The sd-pf-shell model space	540
4.10.1	Pure $N\hbar\omega$ model space	541
4.10.2	Mixed $\hbar\omega$ model space	541

5 Comparison of Experiment and Theory	542
5.1 Single-particle energies	542
5.2 Ground-state binding energies and separation energies	546
5.2.1 Global binding energies	546
5.2.2 sd-shell binding energies	549
5.2.3 Separation energies	552
5.3 Proton-rich nuclei	555
5.3.1 Displacement energies	556
5.3.2 Binding energies of proton-rich nuclei	560
5.3.3 Proton halos	560
5.3.4 Diproton decay	560
5.4 Intruder states	561
5.4.1 Intruder states near ^{12}Be	562
5.4.2 Intruder states near ^{32}Mg	564
5.5 Spectroscopic factors	566
5.6 Interaction cross sections	570
5.7 E1 transitions	575
5.8 Quadrupole moments and E2 transitions	575
5.9 Beta decay	579
5.9.1 Fermi decay	579
5.9.2 Gamow-Teller beta decay	580
5.9.3 Super Gamow-Teller transitions	583
5.10 Magnetic moments	583
6 The Model-Space for Heavier Nuclei	586
7 Summary and Outlook	587

1 Introduction

There are about 270 stable isotopes and about 50 naturally occurring radioactive isotopes. Nuclear reactions with these isotopes found in nature have provided experimental information on about 2500 nuclei. There are about 4000 other more exotic nuclei whose properties remain largely unknown which extend on the nuclear chart out to the proton drip line (where nuclei become unstable to proton decay) and the neutron drip line (where nuclei become unstable to neutron decay). These exotic nuclei are involved in stellar nucleosynthesis, and their properties are important for understanding of the rapidly growing number of observations in astrophysics from ground and satellite based observatories.

The experimental methods for studying the properties of exotic nuclei have grown. New facilities for producing radioactive beams are now available or are being built, and the designs for much larger facilities are underway such as RIA (Rare Isotopes Accelerator) in the USA, and the GSI upgrade and EURISOL (European Isotope Separation On-Line) in Europe. There is a large amount of data on the nuclei near stability, and it is the mandate of nuclear theory to describe all of these in a way which is fundamental and accurate enough to be able to extrapolate to more exotic nuclei. The extrapolation is needed to guide experiments, to test nuclear structure models, and for direct application to nuclear astrophysics where experiment is not known. In addition, nuclei provide one of nature's most abundant examples of mesoscopic systems. Nuclear theory provides the foundation for understanding the great variety of nuclear structure properties which change rapidly as the number and type of constituent nucleons are varied.

Theoretical solutions to the nuclear many-body problem are partly phenomenological, and thus theory and experiment are closely tied together. Theory takes its inspiration from experiment in guiding the structure of the models and their parameters; the nuclear shell model is the primary example [1], [2], [3]. Nuclear experiment takes its inspiration from theory in helping to choose which experiments are most important to prove or disprove model assumptions.

In this review I will examine how the nuclear shell model has been applied to the properties of nuclei near stability, and how its applications are extended to nuclei out to the proton and neutron drip lines. The shell model starts with the concept of closed-shell nuclei which are described by mean-field models. I will discuss the applicability of mean-field models to binding energies, single-particle energies and radii. The shell model allows for configuration mixing beyond the mean field I will describe the assumptions which go into configuration mixing calculations, and how they will be affected by their application to nuclei near the drip lines.

I will restrict myself mainly to a region of medium-light nuclei for which the most work on configuration mixing has been carried out. This will include nuclei up to $Z = 30$ and $N = 50$. For these nuclei we can expect many new experimental results out to the proton and neutron drip lines over the next decade. I will not emphasize the very lightest nuclei below about $A = 10$, for which more exact models have been recently developed and are being applied. These include the “no-core” calculations involving many oscillator shells, [4], [5] and the Green’s function Monte Carlo and variational methods [6], [7]. It is important to compare the results for the standard shell-model methods (which must be used for heavier nuclei) with these more fundamental results for light nuclei in order to better understand the foundation of the nuclear shell-model.

Isospin symmetry is quite good in nuclei. It is broken by the long-range Coulomb interaction and by small charge-dependent parts of the strong interaction. Thus, the structure of a given proton-rich nucleus is similar to its isospin mirror in which the roles of protons and neutrons are interchanged (e.g. ^{18}Ne with $Z = 10$ and $N = 8$ compared to ^{18}O with $Z = 8$ and $N = 10$). Also there are associated isospin multiplets (e.g. the $T = 1$ triplets in ^{18}Ne , ^{18}F and ^{18}O). In this review I will discuss the properties of nuclei with $N \geq Z$ (neutron-rich and $N = Z$ nuclei) out to the neutron drip line. A separate section is devoted to the special models and features which apply to proton-rich nuclei. Due to the repulsive Coulomb interaction, proton-rich nuclei are less stable than their mirrors. The configurations of mirror

nuclei are similar except in situations where low- ℓ orbitals become loosely bound. (In the above example the Thomas-Ehrman shift of the $1/2^+$ ($1s_{1/2}$) state in ^{17}F relative to ^{17}O is important for the structure of ^{18}Ne relative to ^{18}O .)

The region of nuclei covered in this review is shown in Fig. (1). The drip lines in this chart are determined experimentally except for the proton-rich nuclei with $Z > 28$ which is taken from [8], [9], and for the neutron-rich nuclei with $N > 22$ which is based upon [10]. Until recently the experimental information on nuclei was dominated by reactions on the stable nuclei found in nature – the dark boxes in Fig. (1). Radioactive beam facilities will provide a means for studying reactions and properties of essentially all of the nuclei out to the drip lines in Fig. (1).

I begin with a review of those nuclear properties which are relevant to the shell-model magic numbers. The magic nuclei are indicated by the filled circles in Fig. (1). Next, I discuss the assumptions which go into the mean-field and configuration mixing models. As a guide to the ordering of the single-particle states which are discussed, I show in Fig. (2) the single-particle energies for nuclei with $N = Z$ obtained from the SKX Skyrme Hartree-Fock model [11]. Finally, I discuss the comparison of a wide variety of experimental data to the models, starting with binding energies and single-particle energies and progressing to examples of detailed nuclear properties.

This review concentrates on nuclear structure with a few examples of application to astrophysics. Many other examples of astrophysical applications can be found in the conference proceedings of “Nuclei in the Cosmos” [12]. In its application to nuclei near the drip lines, the shell model encounters new phenomena which will be discussed in this review such as changes in the single-particle energies [13], neutron halos [14], [15] and diproton decay [16], [17]. Many acronyms have been constructed – to help the reader, the ones used commonly in the text are given in Table 7 of the appendix along with the section in which they are first discussed.

2 Magic Numbers

2.1 Excited states in even-even nuclei

Some even-even nuclei have first excited states which lie at a relatively high excitation energy compared to the neighboring even-even nuclei. This is an indication that the gap between single-particle levels is relatively large for both protons and neutrons for these particular Z and N values. These values of Z and N are the magic numbers in the nuclear shell model. In the simplest approximation, these nuclei are modeled by closed-shell configurations. (Nuclei for which the gap is large for only protons or neutrons will be called semi-magic or semi-closed-shell nuclei.) Table 1 provides a list of those nuclei which have relatively high-lying first excited states, along with the nominal closed-shell configuration. The nuclei in Table 1 are those with $N \geq Z$. Several of these have mirror proton-rich nuclei near the proton-drip line – ^{14}O , ^{22}Si , ^{36}Ca and ^{48}Ni – the latter has only recently been discovered [18].

Shell-model calculations start with the assumption that one or more of these magic nuclei is inert – they have a closed-shell configuration. For example, the sd shell-model space [24], [3] assumes that ^{16}O and ^{40}Ca are inert. When one considers these closed-shell nuclei in a model space which goes beyond the assumed closed-shell configuration, they are found to have significant non-closed-shell admixtures. For example, ^{12}C in the p-shell model space [25] has 40% of the closed-shell configuration, ^{16}O in the $(0+2+4)\hbar\omega$ model space has about 50% of the closed-shell configuration [26] and ^{56}Ni in the pf-shell model space [27] has about 50% of the closed-shell configuration. (The model spaces and notations are discussed in Sec. 3). Nevertheless, for some purposes these nuclei may be taken as effectively inert, as long the interactions and operators in the model space are renormalized to compensate for the simplification.

A shell-model calculation with some choice of inert cores can be considered successful if it can

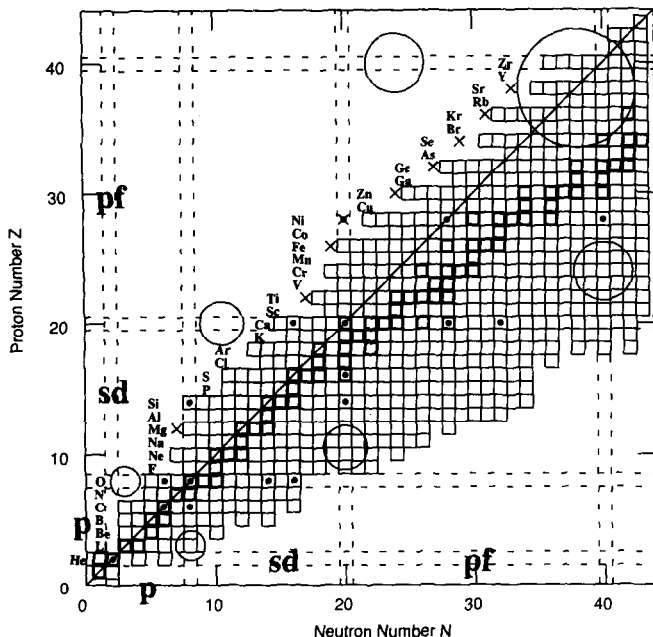


Figure 1: Region of the nuclear chart discussed in this review. Nuclei which are stable to proton and neutron emission are shown by a box. Nuclei above the diagonal line for $N = Z$ are proton-rich and end at the proton drip line. Nuclei below the diagonal degree line are neutron-rich and end at the neutron drip line. Nuclei which exist in nature are indicated by the dark box. The magic nuclei are indicated by a filled circle in the center. The nuclei which are candidates for diproton emission (beyond the proton drip line) are indicated by crosses. The magic number associated with the LS major shell are indicated by dashed lines, and regions where the valence protons and neutron fill the p, sd and pf LS shells are indicated. The circles show the regions of intruder ground-state configurations.

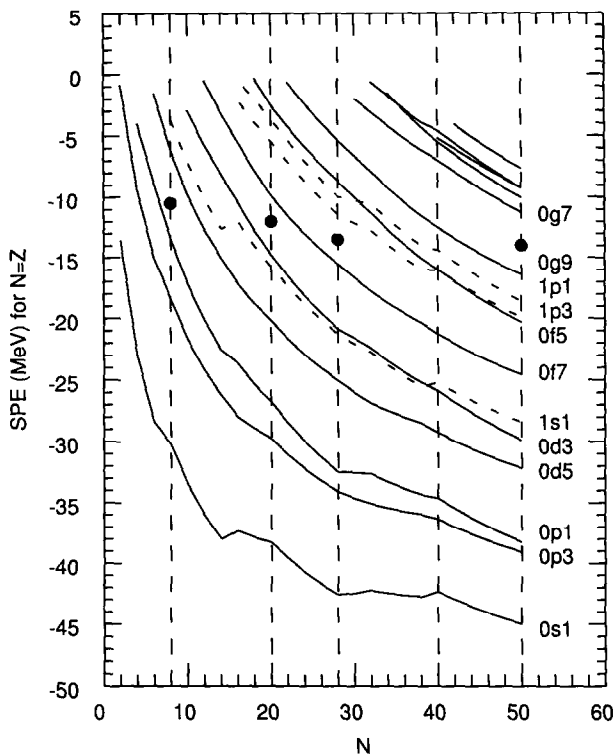


Figure 2: Neutron single-particle energies for nuclei with $N = Z$ as a function of neutron number obtained with the SKX spherical Hartree-Fock calculation. The vertical dashed lines show some of the magic number discussed in the text. The large circles show the approximate Fermi energies for ^{16}O , ^{40}Ca , ^{56}Ni and ^{100}Sn . The orbits are labeled by $(n, \ell, 2j)$.

Table 1: Even-even nuclei with high-lying first excited states. The excitation energies are from the compilations [19], [20] except for ^{22}O from [21], ^{24}O which is the theoretical USD value [22] and ^{34}Si from [23].

Nucleus	Z	N	E_x (MeV)	J^π	Proton Configuration	Neutron Configuration
^4He	2	2	20.2	0^+	$(0s_{1/2})^2$	$(0s_{1/2})^2$
^{12}C	6	6	4.44	2^+	$(0s)^2(0p_{3/2})^4$	$(0s)^2(0p_{3/2})^4$
^{14}C	6	8	6.09	1^-	$(0s)^2(0p_{3/2})^4$	$(0s)^2(0p_{3/2})^4(0p_{1/2})^2$
^{16}O	8	8	6.05	0^+	$(0s)^2(0p)^6$	$(0s)^2(0p)^6$
^{22}O	8	14	3.17	2^+	$(0s)^2(0p)^6$	$(0s)^2(0p)^6(0d_{5/2})^6$
^{24}O	8	16	4.18	2^+	$(0s)^2(0p)^6$	$(0s)^2(0p)^6(0d_{5/2})^6(1s_{1/2})^2$
^{34}Si	14	20	3.30	2^+	$(0s)^2(0p)^6(0d_{5/2})^6$	$(0s)^2(0p)^6(0d_{5/2})^6(1s_{1/2})^2(0d_{3/2})^4$
^{42}Si	14	28	?		$(0s)^2(0p)^6(0d_{5/2})^6$	$(0s)^2(0p)^6(0d_{5/2})^6(1s_{1/2})^2(0d_{3/2})^4(0f_{7/2})^8$
^{36}S	16	20	3.29	2^+	$(0s)^2(0p)^6(0d_{5/2})^6(1s_{1/2})^2$	$(0s)^2(0p)^6(0d_{5/2})^6(1s_{1/2})^2(0d_{3/2})^4$
^{40}Ca	20	20	3.35	0^+	$(0s)^2(0p)^6(0d_{1s})^{12}$	$(0s)^2(0p)^6(0d_{1s})^{12}$
^{48}Ca	20	28	3.83	2^+	$(0s)^2(0p)^6(0d_{1s})^{12}$	$(0s)^2(0p)^6(0d_{1s})^{12}(0f_{7/2})^8$
^{56}Ni	28	28	2.70	2^+	$(0s)^2(0p)^6(0d_{1s})^{12}(0f_{7/2})^8$	$(0s)^2(0p)^6(0d_{1s})^{12}(0f_{7/2})^8$
^{52}Ca	20	32	2.56	2^+	$(0s)^2(0p)^6(0d_{1s})^{12}$	$(0s)^2(0p)^6(0d_{1s})^{12}(0f_{7/2})^8(1p_{3/2})^4$
^{60}Ca	20	40	?		$(0s)^2(0p)^6(0d_{1s})^{12}$	$(0s)^2(0p)^6(0d_{1s})^{12}(0f_{1p})^{20}$
^{70}Ca	20	50	?		$(0s)^2(0p)^6(0d_{1s})^{12}$	$(0s)^2(0p)^6(0d_{1s})^{12}(0f_{1p})^{20}(0g_{9/2})^{10}$
^{68}Ni	28	40	1.77	0^+	$(0s)^2(0p)^6(0d_{1s})^{12}(0f_{7/2})^8$	$(0s)^2(0p)^6(0d_{1s})^{12}(0f_{1p})^{20}$
^{78}Ni	28	50	?		$(0s)^2(0p)^6(0d_{1s})^{12}(0f_{7/2})^8$	$(0s)^2(0p)^6(0d_{1s})^{12}(0f_{1p})^{20}(0g_{9/2})^{10}$

describe a large subset of the observed energy levels and transitions for the nuclei covered by the model space with hamiltonians and operators which are close to those expected from the properties of the free nucleons. Even the most successful (finite) model will eventually encounter states which are not described. These are often called intruder states, and they are attributed to configurations outside the model space. Usually the intruder states start at an excitation energy which is typical of the first excited state in the closed-shell nuclei. But a weakening of the shell gap and correlations can lead to cases where the intruder state comes close to or below the model-space ground state. For example, the first excited $1/2^-$ state at 100 keV in ^{19}F is an intruder in the sd-shell model space, and the $1/2^+$ ground state of ^{11}Be is an intruder in the p-shell model space – both have parities which are not allowed in the respective model spaces. If the intruder state has the same parity as those in the model space, explicit mixing may be important. The history of the shell model has been to consider progressively larger and larger model spaces so that states which would be called intruders in a small model space become fully incorporated into a larger model space.

The first shell-model work in the sd shell involved truncations around the $N = 14$ and $N = 16$ shell closures which exist in the ^{22}O and ^{24}O neutron configurations and the ^{34}Si and ^{36}S proton configurations. However, when both protons and neutrons are active, the strong proton-neutron interaction washes out the $N = 14$ and $N = 16$ closures, and one must consider the full sd model space. For example, for ^{28}Si the ground state obtained with the USD interaction in the full sd shell has only 20% of the nominal $(0d_{5/2})^{12}$ closed-shell component. As will be discussed, the proton-neutron interaction modifies the single-particle energies as well as introducing proton-neutron correlations (configuration mixing).

Likewise in the pf shell, the first shell-model work focused on the truncations around the $N = 28$ shell closure which exists in ^{48}Ca and also to a lesser degree in ^{56}Ni . For example, many of the levels in the nuclei between the 20 and 28 magic numbers are qualitatively described by the simple $(0f_{7/2})^n$ model space [28]. However, a much more complete description of the nuclei in the region of ^{56}Ni is obtained in the full pf shell model. It is interesting to note that ^{52}Ca also has a fairly good closed shell

which is attributed to the filling of the $0p_{3/2}$ orbit, but as protons are added the $N = 32$ closure quickly goes away due to the proton-neutron interaction. A more complete description of the nuclei around $N = 8$ and $N = 20$ requires the larger p-sd and sd-pf model spaces.

^{16}O and ^{40}Ca are the classic LS closed shells. LS closed-shell means that the magic number is associated with the filling of the orbits for a given value of the oscillator major quantum number $N_o = 2n + \ell$, that is, all orbital (L) and spin (S) quantum states up to a given ℓ value are filled. The LS major shell refers to the complete set of orbits for a given value of N_o : p ($N_o=1$), sd ($N_o=2$) and pf ($N_o=3$). For heavier nuclei the LS closed shell becomes weak, as seen in the relatively low-energy of the first excited state in ^{68}Ni ($N = 40$). Likewise ^{60}Ca may have a weak LS (pf shell) closed-shell. For higher mass number the shell gap is determined by the lowering of the highest j orbital due to the spin-orbit interaction, e.g. the filling of the $0f_{7/2}$ orbit in ^{48}Ca . In the region $N = 28 - 50$ the $1p_{3/2}$, $1p_{1/2}$, $0f_{5/2}$ and $0g_{9/2}$ orbitals are closely spaced and could be considered as a jj major-shell model space. The set of orbits in which the highest j from the oscillator shell is removed ($0f_{7/2}$ in the example) and the highest j from the next higher oscillator shell is added ($0g_{9/2}$ in the example) produces the classic jj closed-shell nuclei ^{132}Sn and ^{208}Pb . ^{78}Ni may also be a jj closed-shell nucleus but its first excited state is not yet known. ^{56}Ni is also a fairly good jj closed shell. The nature of ^{42}Si remains to be experimentally determined.

2.2 Single-particle energies and shell gaps

The closed-shell configuration is a single Slater determinant, and one can use Hartree-Fock theory to obtain the binding energy and single-particle energies. In Hartree-Fock theory for a closed-shell nucleus (Z, N) the single-particle energies (SPE) for states above the Fermi surface are related to the binding energy differences:

$$e_p^> = BE(Z, N) - BE^*(Z + 1, N), \quad (1)$$

and

$$e_n^> = BE(Z, N) - BE^*(Z, N + 1). \quad (2)$$

The SPE for states below the Fermi surface are given by

$$e_p^< = BE^*(Z - 1, N) - BE(Z, N), \quad (3)$$

and

$$e_n^< = BE^*(Z, N - 1) - BE(Z, N). \quad (4)$$

The BE are ground state binding energies which are taken as positive values, and e will be negative for bound states. ($BE^* = BE - E_x$) is the ground state binding energy minus the excitation energy of the excited states associated with the single-particle states. The shell gap, defined as the energy difference between the lowest SPE for a state above the Fermi surface minus the highest SPE for a state below the Fermi surface, is:

$$g_p = e_p^> - e_p^< = 2BE(Z, N) - BE(Z + 1, N) - BE(Z - 1, N), \quad (5)$$

and

$$g_n = e_n^> - e_n^< = 2BE(Z, N) - BE(Z, N + 1) - BE(Z, N - 1). \quad (6)$$

The experimental SPE for ^{16}O , ^{40}Ca and ^{48}Ca based upon the assumption that these are closed-shell nuclei are shown in Figs. (3) and (4). The proton and neutron shell gaps for these and other nuclei are given in Table 2. The experimental SPE and gaps are compared with those from the SKX Skyrme HF and the NL3 Dirac Hartree calculations. One observes qualitative agreement with experiment and theory, but the deviations are significant and will be discussed in Sec. 5.1. When the SPE are known

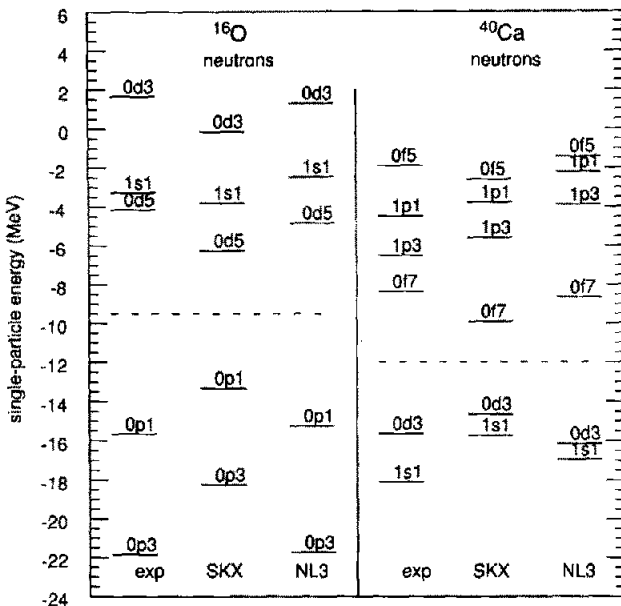


Figure 3: Experimental and theoretical neutron single-particle energies for ^{16}O and ^{40}Ca . The orbits are labeled by $(n, \ell, 2j)$, and the dashed line is the Fermi energy.

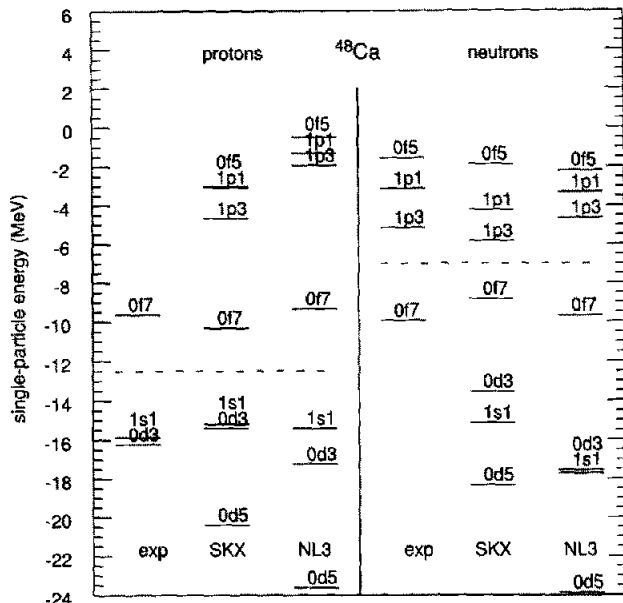


Figure 4: Experimental and theoretical proton and neutron single-particle energies for ^{48}Ca . The orbits are labeled by $(n, \ell, 2j)$, and the dashed line is the Fermi energy.

Table 2: Experimental and theoretical shell gaps. $j^>$ is the orbital just above the gap and $j^<$ is the orbital just below the gap.

Nucleus	Z	$j_p^<$	$j_p^>$	Exp gap (MeV)	SKX gap (MeV)	N	$j_n^<$	$j_n^>$	Exp gap (MeV)	SKX gap (MeV)
${}^4\text{He}$	2	$0s_{1/2}$	$0p_{3/2}$	21.8		2	$0s_{1/2}$	$0p_{3/2}$	21.5	
${}^{12}\text{C}$	6	$0p_{3/2}$	$0p_{1/2}$	14.0	6.1	8	$0p_{1/2}$	$0p_{1/2}$	13.8	6.2
${}^{14}\text{C}$	6	$0p_{3/2}$	$0p_{1/2}$	10.6	5.6	8	$0p_{1/2}$	$1s_{1/2}$	6.9	5.4
${}^{16}\text{O}$	8	$0p_{1/2}$	$0d_{5/2}$	11.5	7.1	8	$0p_{1/2}$	$0d_{5/2}$	11.5	7.3
${}^{22}\text{O}$	8	$0p_{1/2}$	$0d_{5/2}$	10.0	7.8	14	$0d_{5/2}$	$1s_{1/2}$	4.1	1.2
${}^{24}\text{O}$	8	$0p_{1/2}$	$0d_{5/2}$	11.0	7.6	16	$1s_{1/2}$	$0d_{3/2}$	3.8	3.2
${}^{28}\text{O}$	8	$0p_{1/2}$	$0d_{5/2}$		7.8	20	$0d_{3/2}$	$0f_{7/2}$		3.2
${}^{34}\text{Si}$	14	$0d_{5/2}$	$1s_{1/2}$	6.5	2.8	20	$0d_{3/2}$	$0f_{7/2}$	5.1	4.6
${}^{36}\text{S}$	16	$1s_{1/2}$	$0d_{3/2}$	4.7	0.4	20	$0d_{3/2}$	$0f_{7/2}$	5.6	4.6
${}^{40}\text{Ca}$	20	$0d_{3/2}$	$0f_{7/2}$	7.2	4.7	20	$0d_{3/2}$	$0f_{7/2}$	7.3	4.9
${}^{48}\text{Ca}$	20	$1s_{1/2}$	$0f_{7/2}$	6.2	4.9	28	$0f_{7/2}$	$1p_{3/2}$	4.8	3.1
${}^{52}\text{Ca}$	20	$1s_{1/2}$	$0f_{7/2}$		5.0	32	$1p_{3/2}$	$1p_{1/2}$		1.8
${}^{60}\text{Ca}$	20	$1s_{1/2}$	$0f_{7/2}$		4.9	40	$0f_{5/2}$	$0g_{9/2}$		3.1
${}^{56}\text{Ni}$	28	$0f_{7/2}$	$1p_{3/2}$	6.5	4.1	28	$0f_{7/2}$	$1p_{3/2}$	6.4	4.1
${}^{68}\text{Ni}$	28	$0f_{7/2}$	$1p_{3/2}$	5.9	4.3	40	$1p_{1/2}$	$0g_{9/2}$	2.8	2.6
${}^{78}\text{Ni}$	28	$0f_{7/2}$	$1p_{3/2}$		4.9	50	$1p_{1/2}$	$0g_{9/2}$		3.5
${}^{132}\text{Sn}$	50	$0g_{9/2}$	$0g_{7/2}$	6.1	5.3	82	$0h_{11/2}$	$1f_{7/2}$	4.9	4.7
${}^{208}\text{Pb}$	82	$2s_{1/2}$	$0h_{9/2}$	4.2	3.4	126	$2p_{1/2}$	$1g_{9/2}$	3.4	3.6

from experiment, these are usually used for shell-model calculations. For nuclei near the drip lines where the experimental SPE are not known, one needs a theoretical model for predicting or extrapolating the SPE. One way to do this is to use phenomenological mean-field models such as SKX or NL3, and it is thus important to understand the reasons for the deviations in known nuclei.

The shell gaps given in Table 2 give complementary information to the energies of the first excited states (Table 1) about the magic properties of nuclei. However, the shell gaps are sensitive to configuration mixing. In Fig. (5) the binding energy difference of Eq. (6) for even-even nuclei with $N \geq Z$ is plotted vs neutron number. The nuclei with $N = Z$ are connected by a dashed line and the isotopes by solid lines. The magic numbers are expected to exhibit a relatively large gap. However for $N = Z$, $N = 8$ does not appear as a magic number in this way, but rather follows the smooth curve between $Z = 2$ and $Z = 14$. This is probably related to dominance of alpha clustering in these light nuclei – the particularly strong interaction between two-protons and two-neutrons in the same state (such interactions are contained in shell-model configuration mixing). For $N = Z$ above $Z = 14$, the magic numbers 20 and 28 appear weakly. For $N \geq Z$, the magic numbers 20 and 28 often appear but not always. In particular for $Z = 12$ the magic number 20 is not present and for $Z = 16$ (S) the magic number 28 is not present (this is the lowest point for $N = 28$ in Fig. (5)), but is replaced by a peak at $N = 26$. The magic numbers 6, 14, 16, 32 and 40 are not present in the gap systematics. For all nuclei the effective gap as given by Eq. (6) is influenced by pairing and proton-neutron correlations.

The discussion in this section is based on the assumption that the even-even nuclei being discussed actually have closed-shell configurations, and that the states in the neighboring odd-even nuclei are pure single-particle states. This is actually not the case; the closed shells are broken and the single-particle states are fragmented. With shell-model configuration mixing we attempt to calculate the core breaking effects related to the orbits near the Fermi surface. The closed-shell nuclei and the single-particle energies discussed above serve as a starting point for this calculation. There will also be mixing from orbits further away from the Fermi surface, which must be treated explicitly or implicitly in terms

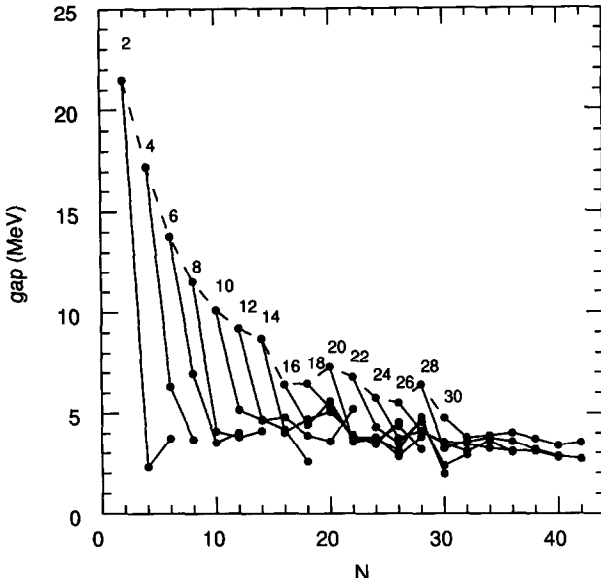


Figure 5: The experimental neutron shell gap for even-even nuclei as a function of neutron number. The values for nuclei with $N = Z$ are connected by a dashed line, and the isotopes labeled by their Z value are connected by solid lines.

of an effective mean-field, effective hamiltonians, and effective transition operators.

3 Model Space and Computations

The “model space” indicates the orbitals and the truncation within that set of orbitals which is assumed for a given calculation. Generally, the best and most complete results are obtained when the model space is as large as possible. However, the computation time increases exponentially with the size the model space, and empirical hamiltonians are better determined in smaller models spaces. Thus the choice of model space is a compromise between what one would like to describe and what is computationally practical. The specific distribution of n_v valence particles over a given set of valence orbits will be called a partition. The complete or “full” model space includes all possible partitions for a given set of orbits.

The many-body states which are obtained in a shell-model basis contain both intrinsic and center-of-mass motion. The operator for the center-of-mass motion contains R^2 and P^2 , where \vec{R} and \vec{P} are the coordinate and momentum of the center of mass. It can be shown in the oscillator model that the center-of-mass is always in the $L = 0$ ground state when the model space is restricted to LS major shells [29], [30], [31]. When more than one major shell is important, excitations out of the center-of-mass ground state can occur. The standard method of removing these spurious states is to add a fictitious center-of-mass hamiltonian [32], [33] which has the effect of raising the energy of the spurious states to a high excitation energy and removing them from the low-lying spectrum of interest.

The prime examples of model spaces in light nuclei are the complete LS major shells, p, sd and pf. There are several advantages to the use of complete LS major shells. The model space contains both $j = \ell \pm 1/2$ orbitals which are important for Gamow-Teller beta decay, magnetic moments and

M1 electromagnetic decay. In addition, admixtures of states which strongly effect the EL electric multipole operators involve the relatively high-energy giant L-multipole resonance, and might be treated perturbatively in terms of effective charges [34], [35]. Finally, there are no spurious states [29], [30], [31]. One can easily treat the complete p and sd shells, but the larger pf shell is often truncated by the maximum number of nucleons excited from the $0f_{7/2}$ shell [36], [37].

Shell-model configuration mixing can also be carried out for the combination of two complete LS major shells, such as p-sd and sd-pf. The basis states can be classified by the partition of n_v valence nucleons between lower and upper LS shells (n_l and n_u). The partition for which the number of nucleons in the upper shell has the smallest possible value allowed by the Pauli principle will be called the $0\hbar\omega$ configuration (meaning lowest energy within the oscillator basis). The $N\hbar\omega$ configurations are excited states in the oscillator basis in which N $\hbar\omega$ units of excitation energy are added to the lowest $0\hbar\omega$ configuration. The model space in which only one N value is considered at a time will be called the “pure $N\hbar\omega$ ” model space, and the configurations are discussed in terms of the N value. The series N , $N+2$, etc, all have the same parity and can be mixed by the hamiltonian. When this mixing is carried out it will be called the “mixed $\hbar\omega$ ” model space.

The ground and low-lying states are usually associated with $0\hbar\omega$ LS configurations. The regions of nuclei in which the valence protons and neutrons go into the p, sd and pf LS major shells are shown in Fig. (1). Regions around $N = Z$ in which both neutrons and protons go into the same major shell are the p, sd and pf for $2 < (N, Z) < 8$, $8 < (N, Z) < 20$ and $20 < (N, Z) < 40$, respectively. There are other regions in which the $0\hbar\omega$ configuration involves protons in one major shell and neutrons in another, such as the p-sd region for neutron-rich nuclei with $2 < Z < 8$ and $8 < N < 20$, and the sd-pf region for neutron-rich nuclei with $8 < Z < 20$ and $20 < N < 40$. All nuclei have states which involve $N\hbar\omega$ excitations between the LS major shells. These are usually excited states, but are sometimes ground states as in the region of intruder states indicated by the circles in Fig. (1). For example the low-lying $1/2^+$ state in ^{13}C and the $1/2^+$ ground state of ^{11}Be could be described as $1\hbar\omega$ excitations out of the p-shell, the latter being an example of an intruder state. These $1\hbar\omega$ excitations are sometimes called non-normal parity states since their parity is opposite to that expected for the $0\hbar\omega$ configurations. ^{16}O could be described by a closed p-shell configuration with the lowest negative-parity excited states being $1\hbar\omega$. Note that the lowest negative parity $T = 1$ states in ^{16}O will have analogue states ^{16}N and ^{16}F which are discussed as $0\hbar\omega$ (ground and low-lying) states in these nuclei.

The full $N\hbar\omega$ model space involves excitations of nucleons over many oscillator shells. For example, the $1\hbar\omega$ excitation of the ^{16}O closed shell involves the excitation of one particle from the p to the sd shell to make a 1p-1h state. A $2\hbar\omega$ model space for ^{16}O would include 1p-1h $s \rightarrow sd$ and $p \rightarrow pf$ excitations as well as 2p-2h $p \rightarrow sd$ excitations. The addition of the 0s and 1p0f shells in $2\hbar\omega$ is necessary for an exact treatment of all spurious states. Nevertheless in some situations one may be able to carry out pure or mixed $\hbar\omega$ calculation within the limited set of p-sd (or sd-pf) orbitals and remove spurious states in the low-lying spectra [38], [39].

The basic inputs to most shell-model configuration mixing codes are the single-particle matrix elements (SPE) and the two-body matrix elements (TBME). For example, in the sd shell there are 3 SPE and 63 TBME. This input for the sd-shell determines the energies and wave functions for about 10^6 levels in the mass region $A = 16 - 40$. The source of these matrix elements in terms of hamiltonians is discussed in the next section. The TBME are specified in terms of matrix elements of the scalar interactions V , $\langle j_1, j_2, J | V | j_3, j_4, J \rangle$ for all possible combinations of j_i orbitals in the model space. J is the total two-particle angular momentum. If isospin is conserved, then the TBME also are specified by their T value (0 or 1). If isospin is not conserved, then there are three sets of TBME for the combinations $pppp$, $nnnn$ and $pnpn$, where p and n stand for proton and neutron, respectively.

There are several methods for carrying out the many-body calculation. One of these involves defining the configurations within the model space in terms of an M-scheme basis [40]. Diagonalization of the hamiltonian in the M-scheme basis results in eigenfunctions with good J (and good T when the

hamiltonian conserves isospin). Another method involves configurations defined in terms of definite J_i coupling of the intermediate states to a total value J [29]. The dimension of the M-scheme is much larger than the J-scheme basis. For example, for 12 particles in the sd model space (^{28}Si) the $M = 0$ dimension is 93,710 and the $J = 0$ dimension is 839. Although the matrix is much larger in the M-scheme, the computation of the elements of the matrix is much easier. M-scheme and J-scheme codes are competitive, but there are situations where one is preferred over the other. A third type of code [33] starts with an M-scheme basis and generates a basis of good J states with an angular momentum projection operator.

Modern versions of the M-scheme code are ANTOINE [41], VECSSSE [42] and MSHELL [43]. Versions of the J-scheme code are RITSSCHIL and [44] and NATHAN [45]. OXBASH [33] is the only version of the projection method. OXBASH is convenient for a variety of truncations (e.g. the recent 24 orbit 2p-2h model space for ^{208}Pb [46]). The OXBASH computer package comes with a library of hamiltonians. When the OXBASH hamiltonians are used they should be referenced to original articles in the literature.

The final step in each of these methods is to diagonalize the matrix. The methods for matrix diagonalization have evolved from Householder method for dimensions of up to a few thousand (10^3), which was used in the 1960's for the p-shell model space [47], to the Lanczos method [48], [49] which is now the standard method for dimensions of up to a few million (10^6).

The reach of shell-model configuration mixing has recently been greatly extended by the use of Monte-Carlo techniques. This method is applicable to the full set of configurations for n_v valence particles in a given set of orbitals (one cannot truncate by the partition). The original Shell-Model-Monte-Carlo (SMMC) method developed by Koonin et al. [50], [51] is applicable to ground states and the statistical properties of excited states. The Quantum-Monte-Carlo-Diagonalization method (QMCD) developed by Otsuka et al. [52] is applicable to the spectra for several states of each spin. For example, a QMCD spectrum for 16 particles in the pf shell (^{56}Ni) with an M-scheme dimension of 1,087,455,228 has recently been obtained [27], [53].

The goal of all of the methods discussed above is to calculate the energies of states for a given hamiltonian to within at least 100 keV of numerical accuracy (although the conventional shell-model codes provide typically 1 keV of numerical accuracy) and to provide wave functions from which other observables can be calculated. There are also many approximate methods. One of these is based upon the exponential convergence of the energy as a function of partition truncation [54]. The deformed HF approximation can be carried out in the full HF basis, for example, with the Skyrme hamiltonian, or with a specific model space with a shell-model hamiltonian. In the latter case one can start with the same hamiltonian which goes into the shell-model diagonalization or QMCD method to test the accuracy of the approximation [55], [53]. There are also several extensions of the deformed HF such as HFB [56] the generator coordinate method [57], [58] and symmetry-projected HFB method [59], [60]. I will take the recent MSk7 results [10] as an example of binding energies which can be obtained by deformed HF calculations, but otherwise I concentrate in this review on the results obtained with “exact” shell-model configuration mixing which has been used most extensively for this region of light nuclei.

4 Hamiltonians

4.1 Introduction

The microscopic calculations discussed in this review are based on two different types of calculations. The first is the mean-field approximation which is applicable to all nuclei but which is based on the restriction to a single Slater determinant. The second is shell-model configuration mixing in which a

matrix based upon all possible Slater determinants within a relatively small subset of valence orbits are diagonalized.

The mean-field models are necessary for explicit calculations of the single-particle energies and density distributions. I will discuss results based upon the non-relativistic Skyrme Hartree-Fock approximation and the relativistic Hartree approximation – details are given in Sec. 4.5. The Woods-Saxon potential is an approximation to the mean-field potential in which the radius and diffuseness can be adjusted for each nucleus or a global set of parameters can be determined [61]. The harmonic-oscillator potential is an approximation to the Woods-Saxon potential. The oscillator potential is often used for calculations of TBME due to its analytical properties, and due to the fact that the center-of-mass motion in the many-body basis can be separated out exactly. The usual global parameterization for the proton oscillator length based upon the rms charge radii is $\hbar\omega = 45A^{-1/3} - 25A^{-2/3}$ and the square of the length parameter is $b^2 = 41.5/\hbar\omega$.

4.2 Basic assumptions

Shell-model configuration mixing is carried out by diagonalizing a hamiltonian which is usually specified by set of numbers for the single-particle energies (SPE) and the two-body matrix elements (TBME) for n particles in a given model space. Such configuration mixing does not explicitly involve the radial wave functions (they are only implicit in the SPE and TBME). The configuration mixing is in terms of the multi-particle “angular” structure in the model space. To apply shell-model configuration mixing results to the calculation of one-body densities, such as those for electromagnetic transitions, the radial wave functions must be separately introduced – one may use mean-field, Woods-Saxon or harmonic-oscillator radial wave functions, depending upon the physical situation (e.g. the harmonic oscillator would be inappropriate for loosely bound halo nuclei.)

Real three-body interactions are required in the Monte-Carlo calculations of the few nucleon systems and for nuclear matter [6]. There are also effective three-body interactions which arise from the model-space truncation [62]. There have been a limited number of calculations which include explicit three-body interactions [63]. But most shell-model calculations do not include three-body interactions, due to their uncertain structure as well as the greater difficulty in carrying out the calculations. It is understood that the three-body interactions influence the interpretation of the effective two-body matrix elements and potentials.

Usually there is no explicit consideration of the kinetic energy in the shell-model configuration mixing, and it is contained implicitly in the SPE. In this sense the configuration mixing can be considered as an application of zeroth-order degenerate perturbation theory. The unperturbed energies in the spherical single-particle basis is highly degenerate, and the degeneracy is broken by a diagonalization of the residual interaction. When applied over a wide mass region, the actual change in the kinetic energy is contained in the effective single-particle energies generated by the residual interaction. Some work has been started on “dynamical” shell-model calculations [64], [65], [66], [67], which include the no-core calculations for light nuclei [4], [5] in which the kinetic energy operator is explicitly considered. Although there are several problems to overcome, a full synthesis of the HF and configuration-mixing methods should be developed [68]. One possibility along this line is to remove all of the average monopole terms, (see Sec. 4.4), from the TBME and to replace them with the HF mean-field binding energy and SPE [69].

It is conventional in shell-model configuration mixing calculations to use the same set of SPE and TBME over the entire mass region covered by the model space with at most a smooth scaling of the TBME. For example, the USD interaction in the *sd*-shell model space assumes the form $TBME^A = TBME^{A=18}(A/18)^{-0.3}$, where the power was determined empirically [24]. The scaling is a result of the change of the (implicit) radial wave function as a function of mass (A). If one takes the simplest oscillator dependence of $\hbar\omega = 41A^{-1/3}$, then the TBME calculated with a delta function vary as $A^{-1/2}$

and the TBME for the long-range Coulomb interaction varies as $A^{-1/6}$. Actual nuclear interactions of intermediate range would vary roughly as $A^{-1/3}$. This smooth scaling is an approximation, and as we approach the drip line one might expect to observe deviations from experiment due to the larger radial extent of the valence wave functions. However, the geometric scaling results do not account for all of physics; there will be additional changes which are more difficult to evaluate due to the density-dependence of the interaction as well as to the more close-lying continuum.

A common element of most configuration-mixing calculations in light nuclei is that the interactions used conserve isospin and are specified in terms of TBME which have good J and T . The effects of the Coulomb interaction are usually treated by adding a Z -dependent constant. It can be deduced from the energy shift between analogue states. In practice, this means that a shell-model result for a given isotopic chain (fixed Z) gives the relative binding energy and excitation energy as a function of neutron number. To obtain the absolute binding energy, a constant must be added to connect it to a given experimental value which can be taken as that of the $T = 0$ ground state for even Z and that of the $T = 1/2$ ground state for odd Z . The levels in mirror nuclei are identical in this approximation. The experimental levels in mirror nuclei are typically shifted by 100 keV or less, which is small compared to the accuracy of most configuration-mixing calculations (200 keV or more). There are larger shifts in light nuclei associated with the Thomas-Ehrman shift of low ℓ orbitals, and these should be treated more carefully in terms of the structure change between mirror nuclei. Configuration mixing in light nuclei can be carried out in a proton-neutron basis [70], but the main interest is in the special problem of overlaps in Fermi beta decay [71] and in isospin forbidden processes [72]. I will discuss mean-field models for the displacement energies in Sec. 5.3.1.

When the model space includes only one radial quantum number n for a given ℓ value, there is a simple relationship between the nuclear density $\rho(r)$, the occupation of the orbitals $\langle n_k \rangle$, and the spherical single-particle states, $\rho(k)$: $\rho(r) = \sum_k \langle n_k \rangle |\phi_k(r)|^2$, where the sum k runs over all occupied orbitals. In the oscillator model there is a fixed relationship between $\hbar\omega$ and the rms radius and the convention is to fix $\hbar\omega$ from the observed charge radii, which has the average mass-dependence $\hbar\omega = 45A^{-1/3} - 25A^{-2/3}$. Likewise, the parameters of the Hartree-Fock or Woods-Saxon potentials are chosen to reproduce the observed densities and radii.

More generally, the model space used for configuration mixing may include several n values for a given ℓ , and the density also includes sums over off-diagonal terms, $\phi_k(r)\phi_{k'}(r)$. One is effectively modifying the spherical radial wave functions in the shell-model basis, and one should check that the constraints imposed by Hartree-Fock theory are not violated by the configuration mixing. Various methods have been introduced in order to enforce the “Hartree-Fock condition” [73], [64], [74]. This point, however, requires more investigation. Ideally one should use an interaction for the shell-model calculation which has the correct saturation properties, and this may require interactions which are explicitly density dependent.

The main method for going beyond the oscillator model is provided by the one-body HF potentials and their Woods-Saxon approximations. One attempts to “marry” the nuclear many-body problem to the one-body problem by approximations which have proven quite successful. Consideration of nuclear densities, such as those used for the interaction cross sections discussed in Sec. 5.6, use HF results which are constrained by orbital occupations obtained with shell-model configuration mixing. The HF potential may be used to obtain the SPE for exotic nuclei which are then used in configuration-mixing calculations. Reactions leading to the unbound states are modeled on the basis of one-body potentials [75]. Giant resonances at high excitation and their coupling to low-lying states are treated in continuum QRPA with HF potentials [76]. The proton and neutron decay widths for unbound states are obtained by using single-particle widths for unbound states in one-body potentials multiplied by the spectroscopic factors from configuration mixing. This latter method is successful for the calculation of proton decay widths [77]. There is also work on the many-body shell model embedded in the one-body continuum

[78]. Brueckner HF (HFB) theory has been used to treat the effects of the one-body continuum on the pairing properties of nuclei [13].

What is missing is the many-body continuum which can be treated only in some special cases. For those nuclei such as ^{11}Li , which may be associated with three-body clusters, three-body models may be used [14]. But it is not easy to include the Pauli exchange effects or to account for the excitation of the subsystems (^9Li in the example).

4.3 The renormalized G matrix

The starting point for shell-model hamiltonians is the renormalized G matrix based upon modern NN interactions [62]. For an assumed closed core, the Brueckner G matrix theory is used to obtain a set of TBME for the model space. This takes into account the short-range repulsive behavior of the interaction via the ladder diagrams. The G matrix can then be renormalized to include the effects of mixing with configurations outside the model space – the core-polarization diagrams. One usually takes the experimental SPE (when available) together with the renormalized G matrix TBME. These calculations for a few valence particles or holes around the closed shell are very successful [62]. But as the number of valence particles increases, the comparison with experiment deteriorates [62], [3].

An example is the spectrum of ^{48}Ca calculated in the pf model space with the SPE from the experimental spectrum of ^{41}Ca and the TBME from the renormalized G matrix [62]. The calculated energy of the 2^+ state is much lower than experiment (there is no $N = 28$ sub-shell closure in the theory). The problem can relate to the effective energy spacing between the $0f_{7/2}$ and $1p_{3/2}$ orbitals as a function of neutron number. With the G matrix, the spacing is nearly constant as a function of neutron number, whereas the observed properties of the $N = 27 - 29$ calcium isotopes require a larger spacing in ^{48}Ca compared to what is found in ^{41}Ca . The change is single-particle energy does not necessarily indicate a defect in the G matrix theory, but is more probably related to an effective change in the ^{40}Ca core as neutrons are added. $^{40,42,44}\text{Ca}$ have rather large $2\hbar\omega$ (sd to pf) admixtures in their ground states. As neutrons are added to the pf shell, the excitations of nucleons from the sd to the pf shell become blocked by the neutrons in the pf shell (the amount of sd-shell excitation is also influenced by the structure of the neutron configuration). This change in the amount of core-excitation can have an influence on the effective single-particle energies. This essence of this picture can be observed within the $0d_{3/2}-0f_{7/2}$ model space [79] in which ^{40}Ca is not assumed to be a closed shell. A full calculation of the effect in the larger sd-pf model space has not yet been carried out.

There is an analogous situation related to the rapid change in the spacing between the $1s_{1/2}$ and $0d_{5/2}$ neutron single-particle energies between ^{16}O and ^{22}O [21] which may be related to a large amount of p to sd core excitation in the $N=Z$ nuclei ^{16}O [26] which gets blocked by the addition of six neutron in ^{22}O . In addition, there are real and effective three-body forces whose effect accumulates with more valence particles. The three-body forces are an essential part of the mean-field hamiltonians, but for practical purposes are almost never included in shell-model configuration mixing. (A new shell-model code is being developed to include three-body interactions [80] to be used for the no-core calculations in light nuclei [5].)

4.4 Empirical approaches

Successful shell-model calculations over a wide mass region are based upon hamiltonians which start from the G matrix but which are empirically renormalized to account for the divergence encountered with the G matrix. The success of this approach is based upon the fact that the shell-model spectra and excitation energies are related to only a relatively few TBME or linear combinations of TBME. One of the oldest and simplest examples is the $0f_{7/2}$ shell [81] where this one orbital is rather isolated. For the $0f_{7/2}$ shell there are only eight TBME and one SPE which can be used to obtain the energies and

wave functions of several hundred levels in the $A = 40 - 56$ mass region [28] (of course a more complete model space for these nuclei is possible now). In small model spaces such as the p-shell, essentially all of the TBME can be obtained empirically, and these will be referred to as effective-TBME (ETBME) hamiltonians.

A common element in the determination of all empirical hamiltonians is an iteration procedure. One chooses a good starting hamiltonian such as the renormalized G matrix and uses this to calculate the wave functions and energies for all energy levels under consideration. These wave functions provide an expansion of each theoretical energy in terms of a linear combination of SPE and TBME which can be associated with experiment to make a least-squares-fit matrix. If the TBME are expressed in terms of potentials or monopole combinations, the TBME can be written as a linear combination of these terms. The values of the SPE and TBME (or terms) from this fit provide the input for the next iteration. The iterations are continued until convergence (when the input TBME are the same as the output TBME). If there are few parameters and the model space is small the iteration procedure is fast. The most ambitious projects such as USD [24] and GXPF [82] have taken years to complete.

In larger model spaces the number of TBME is large and they cannot all be well determined by existing data. The data are sensitive to particular linear combinations of SPE and TBME. The well determined linear combinations can be obtained by finding the eigenvalues of the least-squares-fit matrix [83], [84]. The eigenvalues provide the order of importance and the eigenfunctions provide the linear combination. One then replaces the well-determined linear combinations of TBME by their empirical values, and the renormalized G matrix can be used for the remaining combinations (the choice of cut off in the order of importance is partly subjective). These will be called ETBME+G hamiltonians. The linear-combination method was used to obtain the USD sd-shell hamiltonian [24], and has been more recently used for the GXPF pf-shell hamiltonian [82]. Details of the method are given in [84], [52] and [82].

Some of the most important linear combinations of TBME are those for the monopole interaction which determined the mass-dependence of the effective SPE. The monopole interactions are defined by:

$$\bar{V}_{j,j'}^T = \frac{\sum_j (2J+1) \langle j, j', J, T | V | j, j', J, T \rangle}{\sum_j (2J+1)} \quad (7)$$

Some empirical interactions such as KB3 [36] and KB3G [37] in the pf shell are mainly based upon modifications of some monopole terms, and will be referred to as “G+MON” hamiltonians.

One can also consider effective two-body potential models for the empirical shell-model hamiltonian. In the early shell-model calculations it was found that the modified surface delta interaction (MSDI) empirically worked better than the delta function [85]. “Surface delta” actually means that the radial part of the TBME calculation was ignored and replaced by a constant (the same for all radial wave functions). This was an early form of a density-dependent interaction. The “modified” part means that a constant is added to the delta function and is equivalent to a monopole correction.

The bare G matrix can be well represented in terms of one-boson-exchange potentials. Examples of these are the M3Y [86], [87] (“Michigan sum of three-range Yukawa”) potential from the Reid soft-core NN interaction and the H7B [88] (“Hosaka sum of seven-range boson-exchange”) potential from the Paris interaction. These potentials represent the (bare) G matrix in a very compact form. They differ from the potential for the bare NN interaction due to the inclusion of short-range correlations in the Brueckner theory. The TBME obtained from these potentials are quite similar to those obtained from the full G matrix calculations with more modern NN interactions such as CD Bonn [62], [89] as shown in Fig. (6) for the 2300 TBME obtained for an ^{16}O closed shell in the 0s-0p-1s0d-1p0f model space. The $T = 1$ TBME with CD Bonn are the same as those obtained with M3Y or H7B within a few percent, and the $T = 0$ TBME are on the average about 15% weaker with the CD-Bonn.

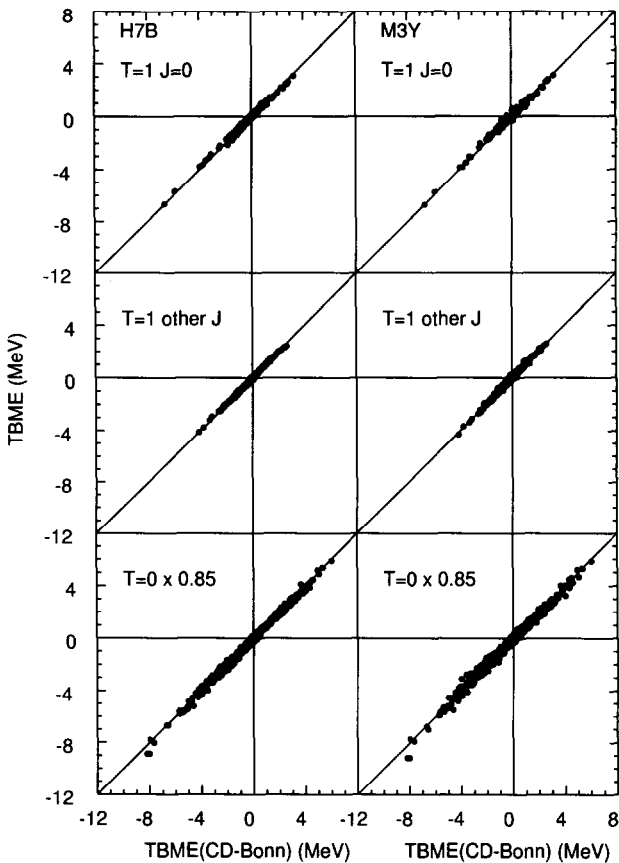


Figure 6: TBME for the s-p-sd-pf model space based on the CD-Bonn G matrix (x-axis) compared with those calculated with the M3Y (y-axis right-hand side) and H7B (y-axis left-hand side) potential models. For $T = 0$ the M3Y and H7B are multiplied by 0.85.

Table 3: Table of model spaces and interactions names. The types of potentials for the s-p-sd-pf and sd-pf models space are discussed in the text.

Model space	A	Interaction	Type	Reference
all	all	SKX	Skyrme	[11]
	all	MSk7	Skyrme	[10]
	all	NL3	Relativistic	[93]
0p (p)	5-16	(6-16)TBME	ETBME	[25]
	5-16	PJT	ETBME	[94]
	5-16	PJP	POT	[94]
	8-16	(8-16)POT	POT	[25]
	8-16	(8-16)TBME	ETBME	[25]
	10-16	PWBT	ETBME	[73]
1s0d (sd)	16-40	USD	ETBME+G	[24]
	16-40	SDPOTA	POT	[90]
1p0f (pf)	40-50	FPMG	G+MON	[95]
	40-50	FPD6	POT	[96]
	40-50	KB3	G+MON	[36]
	40-60	KB3G	G+MON	[37]
	40-60	GXPF	ETBME+G	[82]
s-p-sd-pf	10-20	MK		[97]
	10-20	WBP		[73]
	10-20	WBT		[73]
sd-pf	near $N = 20$	WBMB		[98], [99]
		RCNP		[100]
		Utsuno et al.		[39]
		Dean et al.		[38]

Empirical hamiltonians can also be based upon two-body potential models in which the strengths of the various channels (central, spin-orbit and tensor) are obtained from a fit to energy data. These will be called potential “POT” models for the shell-model hamiltonian. The simplest form of the potential models are the delta functions and MSDI mentioned above. A more elaborate form is the modified-surface-one-boson-exchange-potential (MSOBEP) [90] which will be discussed in Sec. 4.7. Other types of fits related to the potential models can be based upon the relative matrix elements [91] and Talmi integrals [92], [90].

These empirical hamiltonians would be of little interest if they just were made to reproduce a certain set of energy levels. But their usefulness relies on the fact that they have proven to be a powerful way to generate realistic wave functions (from which one calculates transition rate observables) and to extrapolate the known properties of nuclei to the unknown. When one observes something which does not agree with these extrapolations, it is usually an indication of “new physics” involving degrees of freedom which are not in the assumed model space. The observation of such “new physics” in neutron-rich nuclei is the essential aspect of the current and proposed radioactive-beam experimentations.

The names of some commonly used effective hamiltonians and the model-space they are associated with are given in Table 3. These hamiltonians have been determined by a least-squares fit to binding energy and excitation energy data. This was accomplished by varying the full set of two-body matrix elements (ETBME), by varying well determined linear combinations of two-body matrix elements and keeping the rest fixed at some G matrix values (ETBME+G), by adding monopole corrections to the G matrix (G+MON), and by varying potential parameters (POT). Details will be discussed in the

subsections below.

4.5 Mean-field hamiltonians

The Skyrme approximation [101], [102] is an *s*– and *p*–wave expansion of an effective two-body interaction together with an *s*–wave density dependent interaction:

$$\begin{aligned} V_{\text{Skyrme}} = & t_0(1 + x_0 P_\sigma) \delta + \frac{1}{2}(t_1 + x_1 P_\sigma)(\mathbf{k}'^2 \delta + \delta \mathbf{k}^2) \\ & + t_2(1 + x_2 P_\sigma) \mathbf{k}' \cdot \delta \mathbf{k} + \frac{1}{6}t_3(1 + x_3 P_\sigma) \rho^\alpha(\mathbf{R}) \delta \\ & + iW_0(\sigma_i + \sigma_j) \cdot \vec{\mathbf{k}} \otimes \delta \vec{\mathbf{k}}, \end{aligned} \quad (8)$$

where $\delta = \delta(\mathbf{r}_i - \mathbf{r}_j)$, $\mathbf{k} = (1/2i)(\nabla_i - \nabla_j)$ is the relative momentum operator acting on the wave function to the right and \mathbf{k}' is the adjoint of \mathbf{k} . P_σ is the spin-exchange operator and $\mathbf{R} = (\mathbf{r}_i + \mathbf{r}_j)/2$. The form of the Skyrme interaction allows one to calculate the potentials analytically in terms of the densities which makes the self-consistent calculations quite fast – it has recently been used to calculate the binding energies and shapes of 9200 nuclei [10]. I will discuss results of two recent Skyrme hamiltonians.

The HF solution for closed-shell nuclei assumes only a single Slater determinant, but the actual structure of these nuclei is known to be much more complex. The success of the Skyrme model might be justified in the frame-work of the density-functional models which have been widely used in atomic, molecular and condensed matter physics [103], [104].

Goriely et al. [10] obtained the parameters for MSk7 from a least squares fit to the binding energies of 1772 nuclei. Deformed HF+BCS calculations were carried out [105]. Of the ten parameters in Eq. (8), seven were varied (x_0 and x_1 were fixed at -0.5 and α was fixed at $1/3$ to give a nuclear matter incompressibility of $K = 231$ MeV), the spin-orbit energy density retains the terms involving t_1, t_2, x_1 and x_2 , a four-parameters δ -function pairing force was added, and a two-parameter Wigner correction term was added.

The SKX parameters were obtained from a least squares fit to eleven closed-shell nuclei (^{16}O , ^{34}Si , ^{40}Ca , ^{48}Ca , ^{48}Ni , ^{88}Sr , ^{100}Sn , ^{132}Sn and ^{208}Pb), five rms charge radii and 65 single-particle energies. Spherical calculations were carried out (with the MSk7 the eleven nuclei correspond to spherical nuclei [10]). Of the ten parameters in Eq. (8), nine were varied (although only six linear-combinations are well determined) and α was fixed at $1/2$ to give a nuclear matter incompressibility of $K = 270$ MeV (an alternative version SKXm with $\alpha = 1/3$ and $K = 238$ MeV was also determined [11]). The SKX spin-orbit energy-density leaves out terms involving t_1, t_2, x_1 and x_2 , and a generalized two-parameter spin-orbit force based upon the Hartree reduction was used [106]. SKX uses the Friedman-Pandharipande neutron matter equation of state [107] as a constraint (it has recently been shown that the neutron skin is sensitive to the properties of the neutron equation of state [108], [109]). SKX also introduces a new parameter which is needed to reproduce the mirror displacement energies, either by cancelling the Coulomb exchange term (SKX) or by the addition of a charge symmetry breaking (CSB) interaction (SkXcsb [110]).

The relativistic mean-field is an alternative to the Skyrme HF. The relativistic description of nuclear systems uses a field theoretical approach (quantum hydrodynamics) where the interaction of nucleons is described by an exchange of mesons. [111] I will use the non-linear parameter set NL3 [93] which gives a good description of binding energies and radii ($K = 270$ MeV).

4.6 The p-shell model space

The p model space includes the $0p_{1/2}$ and $0p_{3/2}$ valence orbits. The work of Cohen and Kurath on the ETBME and potential models fits to 40 p-shell energies was one of the first to establish the success

of these methods. They derived several interactions: the (6-16)TBME and (8-16)TBME versions of ETBME fit and the (6-16)POT version of the POT fit. In the Oxbash interaction library these are given the names CKI, CKII and CKPOT, respectively. The CK interactions are still reasonable starting points for p-shell calculations.

More recent versions of the p-shell effective interactions are discussed in [94] which take into account a more complete set 77 p-shell energies in the mass region $A = 5 - 16$. In the Oxbash library these new p-shell interactions are given by the names PJT (a ETBME-type interaction called PTBME in [94]) and PJP (POT-type interaction related to PNOALS in [94] but with no mass dependence in the single-particle energies). PJT and PJP have an mass dependence of $\text{TBME}^A = \text{TBME}^{A=16}(A/16)^{-0.17}$, where the power was determined as a best fit to the $A = 5 - 16$ p-shell energy data. Since the reference [94] is not always available I give the PJT and PJP hamiltonians in table 8 of the appendix. Among the other p-shell hamiltonians, is the one from [112] which considered magnetic moments in the hamiltonian fit, which I will call PMOM.

The energy-fit to the entire region of p-shell nuclei ($A = 5 - 16$) have an rms deviation between experimental and theoretical energies of about 600 keV, Table X in [73], [94]. This rather large value may be related to the halo and cluster structure of the lightest p-shell nuclei. Thus for the region of nuclei above about $A = 10$, separate p-shell hamiltonians have been developed based upon fits to levels of p-shell nuclei with $A \geq 10$, such as the ones obtained by Warburton and Brown for their WBP and WBT interactions [73]. The rms deviation between experimental and theoretical energies for $A \geq 10$ is typically 350 keV.

4.7 The sd-shell model space

The sd model space includes the $1s_{1/2}$, $0d_{5/2}$ and $0d_{3/2}$ valence orbits. The renormalized G matrix for the sd-shell was developed in the mid 1960's by Kuo and Brown [113], [114], [115]. These G matrix interactions give reasonable agreement with the experimental $A = 18$ and $A = 38$ spectra. When the G matrix is used to calculate the spectra for the sd-shell nuclei with more than two particles or holes, the agreement with the experimental energy spectra deteriorates rapidly as the number of particles or holes is increased [24]. There were several attempts to find improved empirical hamiltonians. By 1976 Chung and Wildenthal [84], [116] had obtained empirical hamiltonians for the lower-part of the sd-shell (CWP for particles outside of ^{16}O) and the upper part of the sd shell (CWH for holes in ^{40}Ca). By 1984 Wildenthal had found a unique set of ETBME which were able to describe the the entire sd shell – referred to as the USD (universal sd-shell, called W in the Oxbash library) interaction [24]. The TBME of the USD interaction scale as $\text{TBME}^A = \text{TBME}^{A=18}(A/18)^{-0.3}$. The USD interaction was obtained by varying 47 best-determined linear combinations of TBME parameters to fit 447 energies in the mass region $A = 18 - 39$ with an rms deviation of about 185 keV [24], [3]. The 19 least-well-determined parameters where fixed to the $A = 18$ Kuo G matrix [114].

The two-body matrix elements for the USD and G-matrix interactions are compared in Fig. (7). Even though the difference between the empirical matrix element and G matrix is not large, the effect of the difference builds up quickly with particle (or hole) number, and it is important to take into account the empirical adjustments to obtain agreement with spectroscopic data [3]. The differences between the fitted TBME and those from the G matrix may be attributed to many-body effects not included in the G matrix calculation, such as effective three-body interactions and core breaking in ^{16}O and ^{40}Ca .

While the USD interaction is very successful for applications to sd-shell nuclei, it is not immediately applicable outside the sd shell. Moreover, while the same ETBME+G approach can be used for heavier nuclei, the number of TBME grows quickly for the corresponding larger model spaces. In contrast, two-body potential models are in principle applicable for all nuclei, and thus potential models for the sd-shell were investigated [90]. The first step of this investigation was to transform the jj -coupled TBME into tensor-coupled LS matrix elements [117]. The 63 TBME in the sd-shell can be written

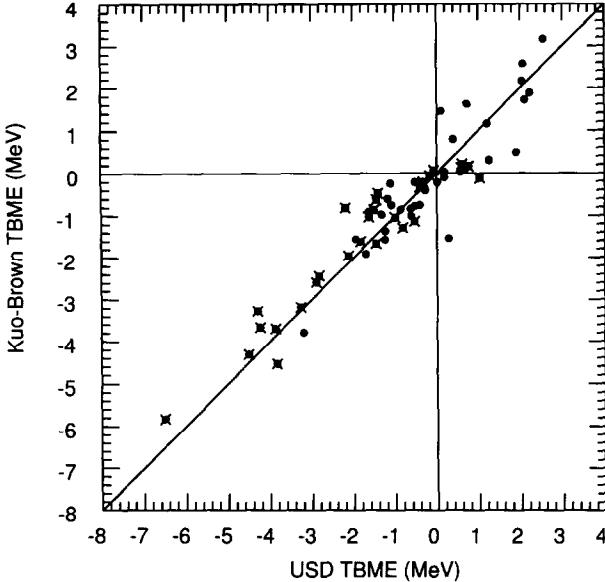


Figure 7: Comparison of the USD TBME for the sd-shell with those from the Kuo-Brown renormalized G matrix. The diagonal TBME are indicated by a cross.

as linear combinations of 20 central, 8 spin-orbit, 16 tensor and 18 antisymmetric spin-orbit (ALS) terms [90]. If the effective interaction is derivable from an isospin-conserving potential that depends only on the relative and center-of-mass coordinates between two nucleons in the nucleus, then the antisymmetric spin-orbit component must vanish. Several investigations of the ALS component have been carried out [118], [119]. For the USD interaction it was found that the ALS component is not very important; setting this component to zero increased the rms deviation from 185 to 215 keV [90]. The central, spin-orbit and tensor potentials were represented by a fixed one-pion exchange term (OPEP) plus medium range OBEP whose strengths are fitted to the sd-shell energy level data. Furthermore, it was found that the fit is improved if the potential is made density dependent, and if monopole terms were added in the central potential. Thus a 14-parameter, density-dependent OBEP was determined which could reproduce the 447 sd-shell energy data with an rms deviation of about 260 keV. I will discuss some results from the potential called SDPOTA in [90].

4.8 The pf-shell model space

The pf model space includes the $1p_{3/2}$, $1p_{1/2}$, $0f_{7/2}$ and $0f_{5/2}$ valence orbits. The Kuo-Brown renormalized G matrix [120] is the traditional starting point for the pf shell TBME. As mentioned above, when the G matrix is used for configuration mixing in ^{48}Ca , the spectrum is in poor agreement with experiment. McGrory et al. [121] found that the G matrix interaction could be improved by the addition of a monopole interaction between the $0f_{7/2}$ orbital and the other pf shell orbitals. The G+MON approach was used for the KB3 interaction by Poves and Zuker [36] and in addition, some of the diagonal $0f_{7/2}$ TBME were changed. KB3 has been widely used for the lower part of the pf shell, but its extrapolation to heavier pf shell nuclei is not very good [27]. KB3 has recently been improved to a new interaction KB3G by the addition of an overall mass dependence to the TBME of the form TBME^A

= TBME^{A=42}(A/42)^{-1/3}, and the addition of more monopole corrections [37]. The new monopole corrections are based upon the effective SPE around ⁴⁸Ca and ⁵⁶Ni. (KB3G is a further development of KBF [122], [123], [124]).

The potential model, MSOBEP, developed for the sd-shell [90] was successfully applied to obtain a six parameter density-dependent interaction for the lower part of the pf shell FPD6 [96], [125]. When applied more recently in the QMCD approach to ⁵⁶Ni, the FPD6 interaction still works quite well [27], [53]. The effective SPE obtained for FPD6 for ⁴⁸Ca and ⁵⁶Ni however can be improved by the addition of monopole interactions (beyond that already contained in FPD6) [37]. The full ETBME+G approach to the pf shell interaction has recently been made possible by the QMCD method and has been applied to all pf shell nuclei over the mass range 47–65 [82]. It will be tested by future calculations and experiments in the more exotic neutron-rich pf shell nuclei.

4.9 The s-p-sd-pf-shell model space

The s-p-sd-pf model space includes the 0s_{1/2}, 0p_{3/2}, 0p_{1/2}, 1s_{1/2}, 0d_{5/2}, 0d_{3/2}, 1p_{3/2}, 1p_{1/2}, 0f_{7/2} and 0f_{5/2} valence orbits with $\hbar\omega$ truncations appropriate for nuclei near ¹⁶O as described below. Near ¹⁶O, the most important part of this model space is the inner part p-sd. The p-sd hamiltonian depends upon four types of TBME:

$$\begin{aligned} (A) & \langle p, p | V | p, p \rangle, \\ (B) & \langle sd, sd | V | sd, sd \rangle, \\ (C) & \langle p, sd | V | p, sd \rangle, \\ (D) & \langle p, p | V | sd, sd \rangle. \end{aligned} \quad (9)$$

Most hamiltonians have been developed for pure N $\hbar\omega$ configurations which only depend on interactions (A), (B) and (C). Warburton and Brown [73] use the USD interaction for (B) and determined interactions (A) and (C) by ETBME+G fits (WBT) and MSOBEP potential model fits (WBP) to experimental energies in the mass region $A = 10 – 22$. WBT and WBP give similar results and are often used interchangeably – their results can be compared as a guide to theoretical error.

An earlier version of the potential model fit is the MK interaction of Millener and Kurath [97]. The MK interaction as used by Millener [126] consists of the p-shell (8–16)TBME for (A), the sd-shell CWP interaction [84], [116] for (B), and the MK potential for (C) (the CWP and USD interactions are very similar for nuclei near ¹⁶O). An interaction which is related to MK is called PSDMK2 in [127]. It is sometimes used (incorrectly in terms of spurious states) within just the p-sd set of orbitals.

For WBT, WBP and MK, the actual calculations are carried out in the larger set of orbits s-p-sd-pf. The addition of 0s and 1p0f is necessary to fully remove the spurious states. Also above $A = 16$ the pf shell becomes explicitly important for the $1\hbar\omega$ excitations. For the additional TBME needed in this extended set of orbits WBP and WBT uses the H7B bare G matrix [88] and MK uses the and the bare Kuo-Brown G matrix [114].

The mixed $\hbar\omega$ model space also depends upon the off-diagonal interaction (D). For WBT and WBP the (D) matrix elements are determined from the WBP potential obtained for (C). The MK interaction uses the bare Kuo-Brown G matrix for (D). Another version of the Warburton-Brown interaction called WBN [128] uses the H7B bare G matrix [88] multiplied by 0.8 for (D).

4.10 The sd-pf-shell model space

The sd-pf model space includes the 1s_{1/2}, 0d_{5/2}, 0d_{3/2}, 1p_{3/2}, 1p_{1/2}, 0f_{7/2} and 0f_{5/2} valence orbits with $\hbar\omega$ truncations described below. This model space has been used for the region of nuclei around $N = 20$. It would be best to consider the larger p-sd-pf-sdg model space (in analogy with the s-p-sd-pf model

space for ^{16}O discussed above), but for practical reasons (e.g. the number of orbits and dimensions which can be considered in the shell-model codes) a limitation to just sd-pf is imposed. Hamiltonians have been designed for both pure $N\hbar\omega$ and mixed $\hbar\omega$ model spaces.

4.10.1 Pure $N\hbar\omega$ model space

The sd-pf hamiltonian depends upon four types of TBME:

$$\begin{aligned} (A) & \langle sd, sd | V | sd, sd \rangle, \\ (B) & \langle pf, pf | V | pf, pf \rangle, \\ (C) & \langle sd, pf | V | sd, pf \rangle, \\ (D) & \langle sd, sd | V | pf, pf \rangle. \end{aligned} \quad (10)$$

Hamiltonians have been developed for both pure and mixed $\hbar\omega$ configurations.

The WBMB hamiltonian for the pure $N\hbar\omega$ model space was developed by Warburton, Becker, Millener and Brown [98]. WBMB has been used for several studies of neutron-rich beta decay [129], [130], [131] and for a study of the island-of-inversion around ^{32}Mg [99] (more recently extended to larger neutron number in [132]). For WBMB the USD sd-shell interaction [24] is used for (A), and the FPMG pf-shell interaction [95] is used for (B). The cross-shell (C) and off-diagonal TBME (D) was calculated from the Millener-Kurath potential [97] with some adjustments in diagonal cross-shell matrix elements based upon the $1\hbar\omega$ states in ^{40}Ca . WBMB is designed for use in the pure $N\hbar\omega$ model space which does not involve the (D) interaction. WBMB is sometimes applied in the mixed $\hbar\omega$ model space for a qualitative understanding of the mixing. A more recent version of WBMB has replaced the FPMG pf-shell interaction with the FPD6 pf-shell interaction.

Retamosa et al., [100] have also constructed a sd-pf interaction which has been used for $Z = 8 - 13$ [100] and $Z = 14 - 20$ [133] which I will call the RCNP interaction. They again use the USD for (A) but take pf in [36] for (B). (C) is obtained from the Lee-Kahanna-Scott G matrix [134], and then monopole corrections are added to fit some selected experimental energy data together with the prescriptions of Duflo and Zuker [135] for the most exotic nuclei. The sd-pf shell interaction continues to evolve. Recently the observation of the $3/2^-$ excited state in ^{35}Si has lead to further monopole corrections to the RCNP interaction [136].

4.10.2 Mixed $\hbar\omega$ model space

Early work which demonstrated the importance of intruder states was carried out by mixing $0\hbar\omega$ and $2\hbar\omega$ in a reduced set of orbitals [137], [138], [139], [140], [141]. The QMCD calculations of Utsuno et al. use the full sd-0f_{7/2}-1p_{3/2} model space. Their interaction starts with one similar to WBMB which is appropriate for the pure $N\hbar\omega$ model space. USD for (A), the Kuo-Brown renormalized G matrix [120] for (B) and the Millener-Kurath potential as modified in [98] for (C) and (D). When applied to the full sd-0f_{7/2}-1p_{3/2} model space this interaction must be renormalized. The 0d_{5/2}-0d_{3/2} and 0d_{d5/2}-0f_{7/2} monopole terms for $T = 0$ and 1 were adjusted and the USD pairing matrix elements are reduced [39] in order to account for several experimental features of the neutron-rich nuclei around $N = 20$ such as the fact that ^{26}O unbound [142], [143].

The full sd-pf model space has been considered in the SMMC calculations of Dean et al. [38], [144]. They used a renormalized G matrix interaction for the sd-pf model in which the monopole interactions are modified to reproduce the SPE from the Duflo-Zuker parameterization [135].

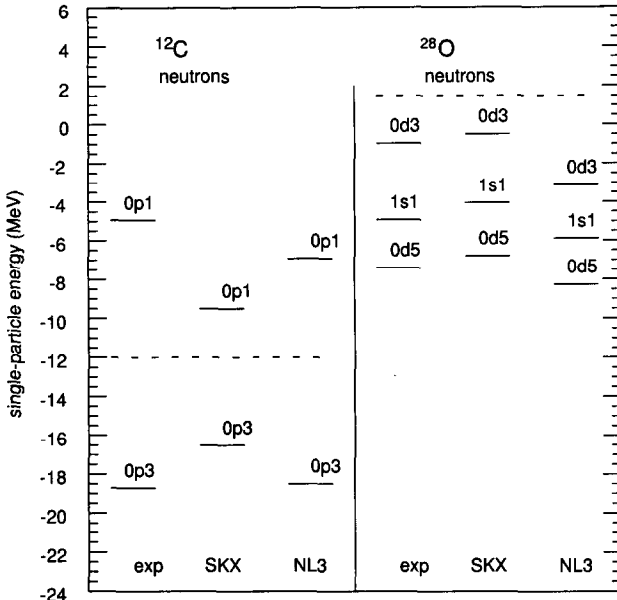


Figure 8: Experimental and theoretical neutron single-particle energies for ^{12}C and ^{28}O . The experimental values for ^{28}O are based upon those extrapolated with the USD sd-shell interaction. The orbits are labeled by $(n, \ell, 2j)$, and the dashed line is the Fermi energy.

5 Comparison of Experiment and Theory

In this section I discuss comparisons between experiment and theory in roughly increasing order of theoretical complexity, starting with the mean-field properties for the binding energies and single-particle energies. Next I consider $0\hbar\omega$ shell-model configuration mixing for the binding energies and separation energies. The special features of proton-rich nuclei are discussed in Sec. 5.3. The separation energies will show features which can only be explained by the intruder states associated with $N\hbar\omega$ excitations discussed in Sec. 5.4. The final sections cover data on spectroscopic factors, E1 transitions, quadrupole moments, E2 transitions, magnetic moments, beta decay and interaction cross sections.

5.1 Single-particle energies

The experimental single-particle energies for ^{16}O , ^{40}Ca and ^{48}Ca are compared with the SKX Hartree-Fock and NL3 Dirac Hartree calculations in Figs. (3) and (4). Both mean-field calculations are in qualitative agreement with experiment, but overall the NL3 results are in better, in particular for the gap at the Fermi surface. The interpretation of the agreement or disagreement of the mean-field models with experiment depends upon how the results are to be used in conjunction with shell-model configuration mixing. I illustrate this by the example of ^{12}C shown in figure (8).

Gloeckner and Zamick [145] used the ^{12}C example to show that the effective gaps defined by Eqs. (5) and (6) from the binding energies of the lowest states in the odd-even nuclei, ^{11}C , ^{11}B , ^{13}C and ^{13}N in this case, are larger than the intrinsic mean-field gaps. In Fig. (8) I show the experimental neutron

gap in ^{12}C assuming a closed-shell ($0\text{p}_{3/2}$)⁴ configuration for protons and neutrons compared to SKX and NL3. In SKX the gap is close to the typical spin-orbit splitting of 6 MeV and the experimental value is about twice as large and similar to NL3. When the full p-shell model space is used for ^{12}C , the empirical interactions of Cohen and Kurath have an effective spin-orbit splitting of about 6 MeV (e.g. the difference between the single-hole energies in ^{16}O , Fig. (3)), and when the p-shell calculation is restricted to a closed shell configuration the gap is about 6.0 MeV. With shell-model configuration mixing the ^{12}C ground state has about 40% of the closed-shell component and the binding energies of ^{11}C and ^{13}C relative to ^{12}C agree with experiment. The reason for the large effect gap is that ^{11}C and ^{13}C are not pure hole and particle states. In order to recover the true single-particle gap from experiment one must take the energy weighted sum over the spectroscopic factors from ^{12}C to all states in ^{11}C and ^{13}C . One can try to obtain mean-field SPE from a consideration of the experimental spectroscopic pickup and stripping data, but it is difficult to know if the data set is complete, especially if the strength is fragmented over many levels.

From this example we would conclude that NL3 is most appropriate for calculations in which ^{12}C is treated as a closed shell, and that SKX is most appropriate for calculations in which ^{12}C is treated in the full p model space. Similar p-sd and sd-pf mixing calculations for ^{16}O and ^{40}Ca , respectively, are much more difficult, but it is likely that the large gaps observed in ^{16}O and ^{40}Ca compared to SKX is also related to core-breaking effects. For ^{16}O , $2\hbar\omega$ admixture in the ground state with the WBP interaction [73] increases the gap by about 2.5 MeV.

This type of configuration mixing between appears to be particularly large for $N = Z$ nuclei. A neutron (or proton) excess increases the stability of the closed shell nuclei, so that the closed shell mean-field approximation is better and the SKX SPE become closer to the experimental values (based upon an assumed closed-shell configuration) in nuclei such as ^{24}O , ^{34}Si and ^{48}Ca . As an extreme example I compare in Fig. (8) the sd-shell neutron SPE for ^{28}O from SKX with those extrapolated from the USD configuration mixing calculations (see Sec. 5.2.1).

The difference between SKX and NL3 can be mainly related to the effective mass (m^*/m), which is about 1.0 for SKX and 0.6 for NL3. The effective mass for the Skyrme interaction can be tuned by the parameters [102] and those for SKX are determined primarily from the SPE of heavy nuclei where the spacing around the Fermi surface requires an effective mass of about 1.0 [11]. I show as examples the case of ^{132}Sn in Fig. (9) and ^{208}Pb in Fig. (10). For NL3 on the other hand, an effective mass of about 0.6 is intrinsic to the model. An effective mass of 0.6 gives SPE in heavy nuclei which are spread out compared to experiment as shown by NL3 in Figs. (9) and (10). Typical Brueckner G matrix interactions also give an effective mass of about 0.6, and the reason for an empirical value of near unity in heavy nuclei is attributed to configuration mixing due to coupling of the single-particle states to surface vibrations [146], [147]. Thus the appropriate mean-field calculation depends upon whether the configuration mixing is to be incorporated implicitly in the mean-field parameters, or explicitly in the wave functions. In this sense configuration mixing in ^{132}Sn and ^{208}Pb is required to recover the correct SPE starting from the NL3 interaction, whereas SKX requires these nuclei to be treated as closed shells.

Pairing in semi-magic nuclei also produces an effective gap which is larger than the spacing between single-particle levels. A simple example is provided by pairing in the Ni isotopes. The $1\text{p}_{3/2}-0\text{f}_{5/2}$ SPE spacing in ^{57}Ni is 0.77 MeV, whereas if ^{60}Ni is treated as a closed $1\text{p}_{3/2}$ shell the effective gap from Eq. (6) is 3.57 MeV – this is due to the configuration mixing between these two orbitals which is dominated by the pairing interaction.

In summary, there are two different types of configuration mixing effects in the observed SPE. The coupling to surface vibrations increases the effective mass and compresses the spectrum around the Fermi surface. On the other hand the pairing and proton-neutron correlations increase the gap at the Fermi surface. The use and validity of mean-field models depends upon the context in which they are to be used. There are other considerations associated with the form of the mean-field potentials and the approximations which are used. It appears that low- ℓ orbits above the Fermi surface are systematically

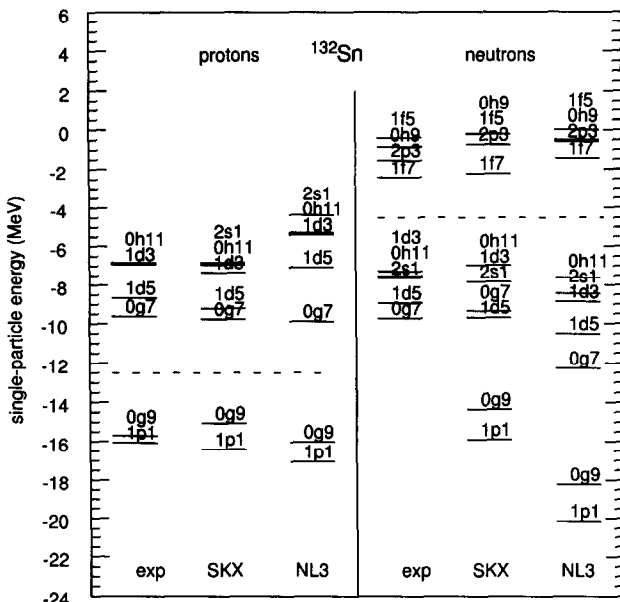


Figure 9: Experimental and theoretical proton and neutron single-particle energies for ^{132}Sn . The orbits are labeled by $(n, \ell, 2j)$, and the dashed line is the Fermi energy.

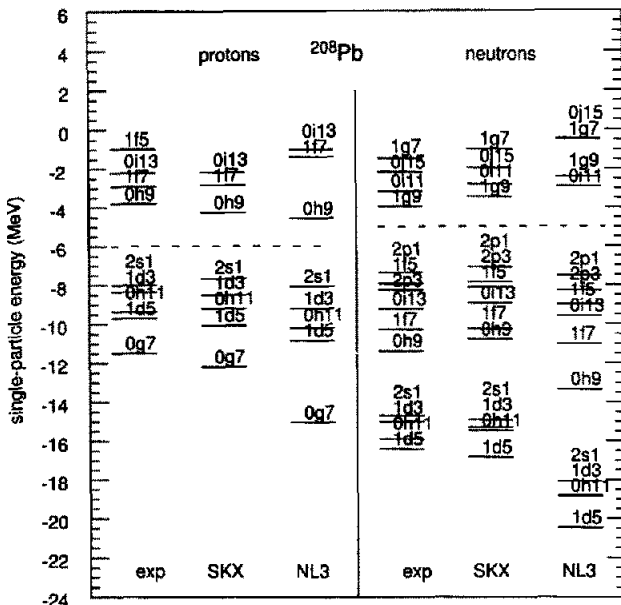


Figure 10: Experimental and theoretical proton and neutron single-particle energies for ¹³²Sn. The orbits are labeled by $(n, \ell, 2j)$, and the dashed line is the Fermi energy.

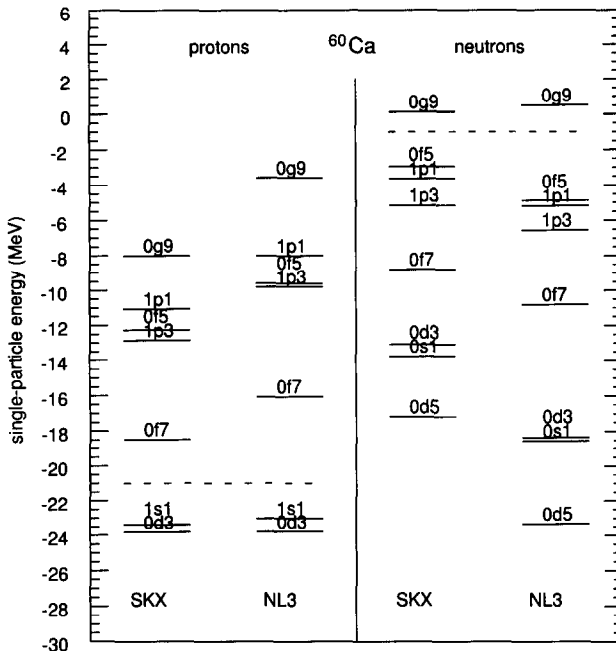


Figure 11: Theoretical proton and neutron single-particle energies for ^{60}Ca . The orbits are labeled by $(n, \ell, 2j)$, and the dashed line is the Fermi energy.

too high in the mean-field models compared to experiment. This is observed for the 0s and 1p orbitals in Fig. (3), and discussed for the low- ℓ orbitals in ^{208}Pb with SKX in [11]. This indicates that the “large-radius behaviour” of these mean-field potentials is too weak, thus not providing enough binding for these low- ℓ orbitals. There are also issues associated with rearrangement energies and center-of-mass corrections which generally go as $(1/A)$ and are most important for light nuclei [74]. The SKX and NL3 models provide perhaps the most reliable way to extrapolate the SPE from nuclei near stability to the most exotic nuclei near the drip lines. The predictions for the ^{60}Ca and ^{78}Ni SPE are given in Figs. (11) and (12), respectively. Other recent predictions for ^{60}Ca are given in [148]. It will remain for future experiments to test these extrapolations.

5.2 Ground-state binding energies and separation energies

5.2.1 Global binding energies

The binding energies for the region of nuclei up to $A = 60$ vary by hundreds of MeV, yet we will be discussing theoretical calculations which reproduce experiment to the level of several hundred keV to an MeV. The “coast to coast” situation for all nuclei between the drip lines is illustrated in Fig. (13) where the BE obtained with the MSk7 HF calculations [10] are shown for all nuclei between the proton and neutron drip lines centered on $Z = 20$ (left-hand side) and $N = 20$ (right-hand side) and compared to experiment where known.

The drip line is reached in each case when the derivative of the BE curve with respect to proton or

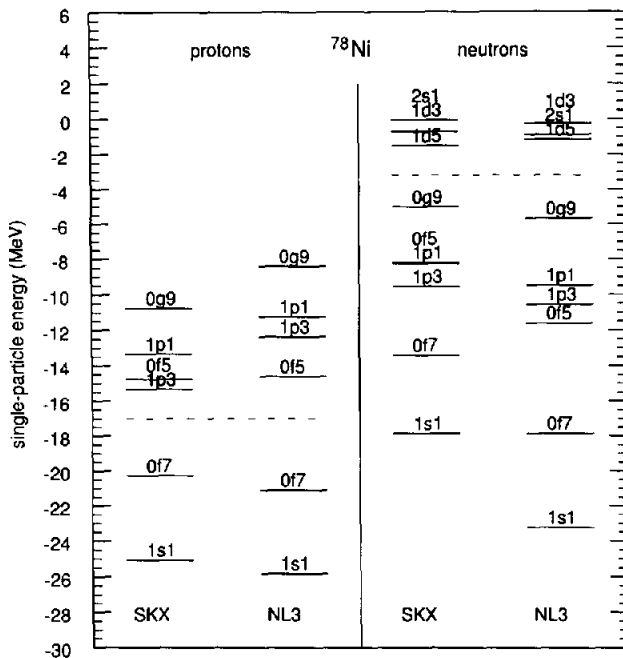


Figure 12: Theoretical proton and neutron single-particle energies for ^{78}Ni . The orbits are labeled by $(n, \ell, 2j)$, and the dashed line is the Fermi energy.

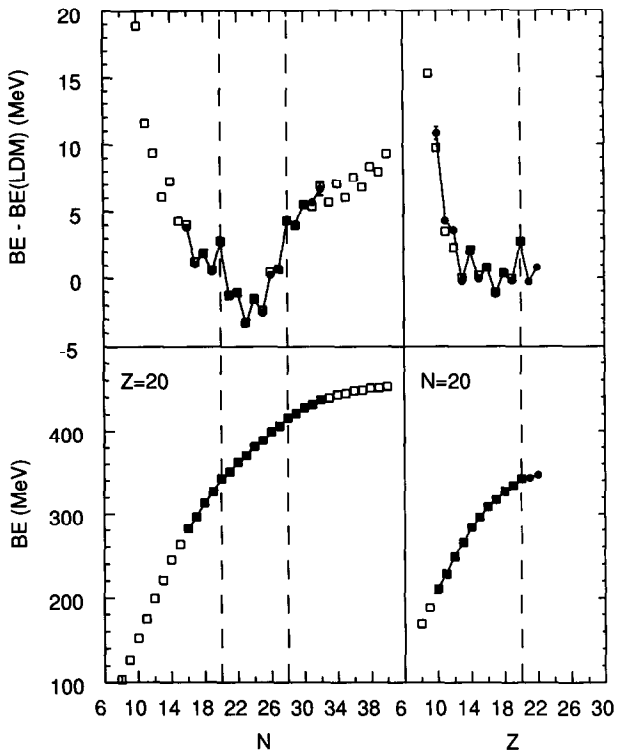


Figure 13: Theoretical (squares) and experimental (filled circles) binding energy for $Z = 20$ as a function of neutron number (left-hand side) and for $N = 20$ as a function of proton number (right-hand side). In the upper panels a smooth curve given by the liquid drop model is subtracted from theory and experiment. The magic numbers $N = 20$, $N = 28$ and $Z = 20$ are indicated by dashed lines.

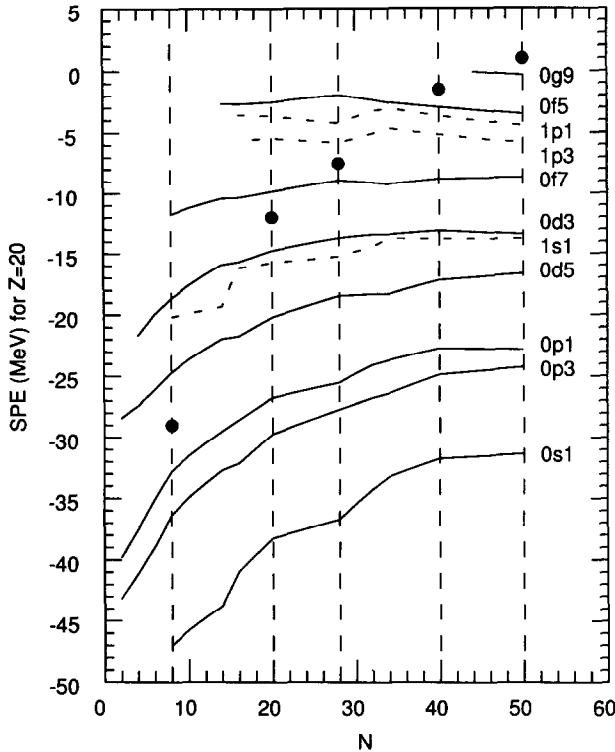


Figure 14: Neutron single-particle energies for the calcium isotopes obtained with the SKX spherical Hartree-Fock calculation. The vertical dashed lines show some of the magic number discussed in the text. The large circles show the approximate Fermi energies for ^{28}Ca , ^{40}Ca , ^{48}Ca , ^{60}Ca and ^{70}Ca . The orbits are labeled by $(n, \ell, 2j)$.

neutron number goes to zero. One observes in the bottom panels of Fig. (13) an apparently featureless and smooth curve with the data in agreement with theory. However, we are interested in a much higher level of detail which is illustrated in the top panel by subtracting a smooth curve given by the liquid drop model (LDM) from theory and experiment. I use for the LDM binding energy in MeV:

$$\text{BE}(\text{LDM}) = 15.56A - 17.23A^{2/3} - 0.69677Z^2A^{-1/3} - 23.285(N - Z)^2/A. \quad (11)$$

The top curve brings out the detail related the microscopic aspects of the nuclear shell model.

Fig. (2) is extended in Fig. (14) to the SKX single-particle energies for the calcium isotopes as a function of neutron number. Beyond ^{60}Ca one observes that the $0g_{9/2}$ orbital becomes bound, and thus ^{70}Ca will be bound with SKX. The even-even calcium nuclei between ^{60}Ca and ^{70}Ca will probably be bound due to pairing (which has been neglected in this particular SKX HF calculation).

5.2.2 sd-shell binding energies

The binding energies (BE) of the oxygen and fluorine isotopes are shown in Fig. (15). When the BE for a given neutron number N is smaller than that of the nucleus with $N - n$ it is unbound to n -neutron

decay. The experimental BE (filled circles connected by lines) are compared to those obtained with the USD (squares) and SDPOTA (crosses) interactions. Below $N = 16$ experiment and theory fall on top of each other within about 200 keV. Starting at $N = 16$ the extrapolated BE from the two interactions begin to show more difference. The sd-shell theory is 1–2 MeV more bound than experiment, suggesting that the residual interaction becomes slightly weaker toward the drip line compared to that inferred from nuclei near the valley of stability. However, the full interpretation will have to include the pf-shell admixtures which become important near $N = 20$ [149].

The BE from the SDPOTA interaction are in agreement with known limits of stability. ^{26}O is bound to two-neutron decay by 1.0 MeV with USD but unbound by 0.02 MeV with SDPOTA, only the latter is consistent with the experimental non-observation of ^{26}O [142], [143]. ^{28}F is unbound to one-neutron decay with both USD and SDPOTA, in agreement with experiment [150]. ^{29}F is bound to neutron decay with both USD and SDPOTA in agreement with its experimental observation [151]. From a comparison of USD and SDPOTA we would conclude that the theoretical uncertainty in the extrapolation to these most neutron-rich nuclei is about 1 MeV. In more recent theoretical investigations the effective interactions are often adjusted to give agreement with the stability properties of the oxygen isotopes.

The qualitative features of the binding energies for the oxygen isotopes can be understood in the extreme j-j coupling limit. I show in Fig. (16) the effective neutron single-particle energies (ESPE) as a function of neutron number in the j-j coupling limit. (The sd-shell calculations shown in Fig. (15) go beyond j-j coupling and include all possible sd-shell configurations, but the dominant configurations are those discussed below.)

Between $N=8$ and 14 the neutrons fill the $d_{5/2}$ orbit which is bound in ^{16}O by about 4 MeV. This, together with the attractive pairing energy, provides the sharp increase in binding energy observed between $N=8$ and 14. Between $N=14$ and 16 the neutrons fill the $s_{1/2}$ orbit which is less bound than the $d_{5/2}$. Thus one starts to see less increase in the binding energy at this point. Between $N=16$ and 20 the neutrons fill the $d_{3/2}$ orbit which has close to zero energy, and the binding energy curve becomes flat in this region. This flatness, of course, makes it difficult to predict exactly which nuclei will be stable to neutron decay. Beyond $N=20$ the neutrons occupy the pf shell orbits which are unbound. Hence the binding energy curve decreases beyond this point.

One notes in Fig. (16) that the shell gaps change with neutron number. Near ^{16}O the $0d_{5/2}$ and $1s_{1/2}$ orbits are close together, but for ^{22}O they have become about 4 MeV apart making $N = 14$ a magic number. The shift in the $1s_{1/2}$ ESPE between ^{16}O and ^{22}O is due the monopole interaction between the $0d_{5/2}$ and $1s_{1/2}$ orbitals which involve the diagonal TBME

$\langle 0d_{5/2}, 1s_{1/2}, J, T = 1 | V | 0d_{5/2}, 1s_{1/2}, J, T = 1 \rangle$. These TBME can be obtained from information on excited states in the light oxygen isotopes such as ^{18}O and ^{19}O . Data on excitation energies in nuclei near stability relevant to these TBME were included in the 447 energies used to obtain the USD and SDPOTA interactions.

With the renormalized G matrix the $0d_{5/2}$ and $1s_{1/2}$ orbits remain close together as a function of neutron number. Indeed, it is this apparent failure of the G matrix which makes the agreement with experiment diverge as a function of increasing neutron number (using the ^{16}O SPE). The origin of this difference between USD and the G matrix interactions is probably complex, involving different amounts of p-shell core breaking as one goes from ^{16}O to ^{22}O as well as three-body interactions, and it should not necessarily be taken as a failure of the basic G matrix approach.

For $N = 16$ the $1s_{1/2}$ - $0d_{3/2}$ gap also opens up as can be seen in Fig. (16), and this $N = 16$ becomes a magic number. As protons are added to the sd-shell the proton-neutron interaction further modifies the ESPE. In particular, by $Z = 14$ the $N = 16$ gap disappears. This change can be related to the large $0d_{5/2}$ - $0d_{3/2}$ TBME associated with the $V_{\tau\sigma}$ proton-neutron interaction [152]. The same mechanism is responsible for the loss of the $N = 32$ shell gap [153] (the $0f_{7/2}$ - $0f_{5/2}$ proton-neutron interaction) and for the sudden change of deformation in the Zirconium isotopes [154] (the $0g_{9/2}$ - $0g_{7/2}$ proton-neutron

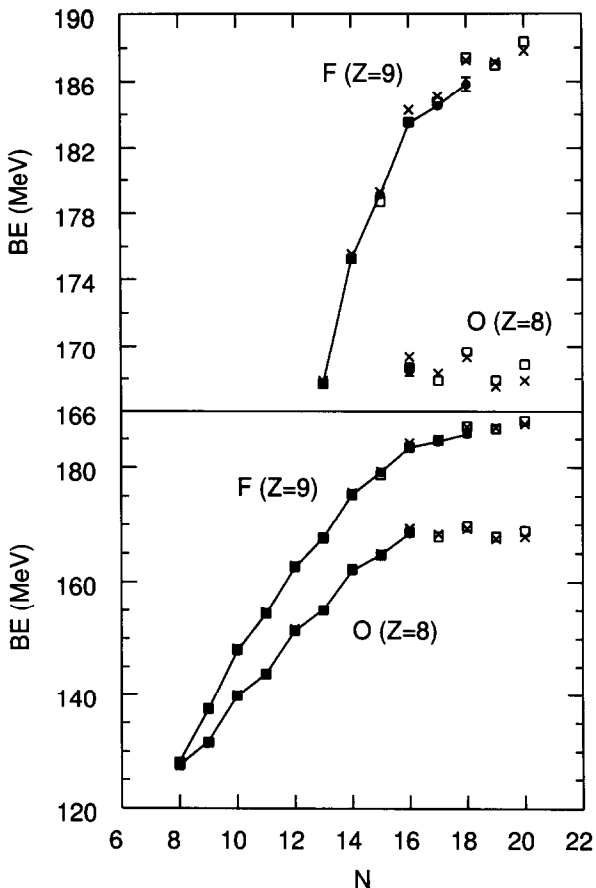


Figure 15: Binding energies for the oxygen and fluorine isotopes as a function of neutron number. The upper panel is an expanded part of the lower panel. The experimental values are the filled circles connected by lines. The theoretical values are given for the USD (squares) and SDPOTA (crosses) sd-shell interactions.

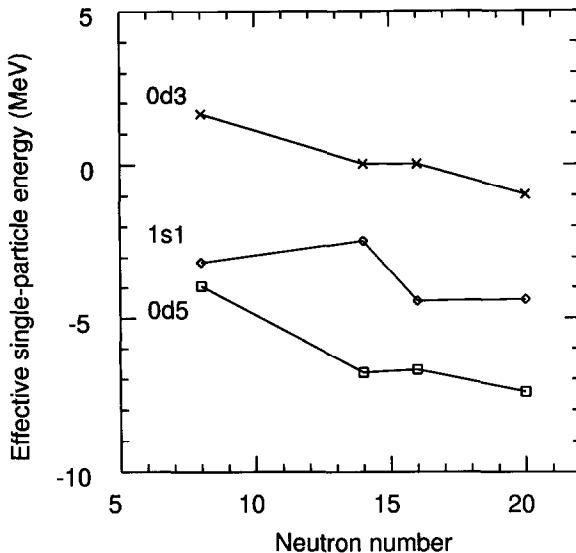


Figure 16: The effective single-particle energies for the oxygen isotopes as a function of neutron number obtained from the USD interaction. The orbits are labeled by $(n, \ell, 2j)$.

interaction).

Beyond ^{24}O , the ESPE depend on the $0\text{d}_{5/2}-0\text{d}_{3/2} T = 1$ (neutron-neutron) TBME. Data in the oxygen isotopes on excitation energies, relevant to these matrix elements, are not well known since they are associated with levels at high excitation and are mixed with intruder states. Hence beyond ^{24}O , the BE predictions rely components of the interaction which cannot be derived from data in nuclei near stability. For the USD interaction the Kuo-Brown G matrix was used for the poorly determined TBME, and for the SDPOTA interaction the fitted potential model was used for all TBME.

5.2.3 Separation energies

A more comprehensive comparison of binding energies can be given in terms of the one- and two-neutron separation energies. For these comparison I use the data compiled of Audi and Wapstra [155] which are supplemented by the recent mass measurements [156], [157].

The one-neutron separation energies obtained for the MSk7 HF model are compared to experiment for some selected Z values in Fig. (17). One finds good overall agreement with deviations of up to one MeV both for exotic nuclei and for those near the valley of stability. From the staggering one can observe deviations which can be attributed to pairing. This may be partly attributed to the simple global delta function assumed for the pairing [10], [105] and partly attributed to the BCS approximation which insufficient for light nuclei. The interaction might be improved by the use of a G matrix or empirical interaction. The BCS can be replaced by exact pairing solution [158]. The two-neutron separation energies for MSk7 are compared for experiment for all even Z values in Fig. (18). Again one observes deviations of up to 1–2 MeV for all nuclei. In this case the deviation may be attributed to the mean-field and the associated single-particle energies or to the deformed HF approximation for the residual proton-neutron interaction. One notices particularly large deviations for the oxygen ($Z = 8$) and calcium ($Z = 20$) isotopes near stability which are probably related to core

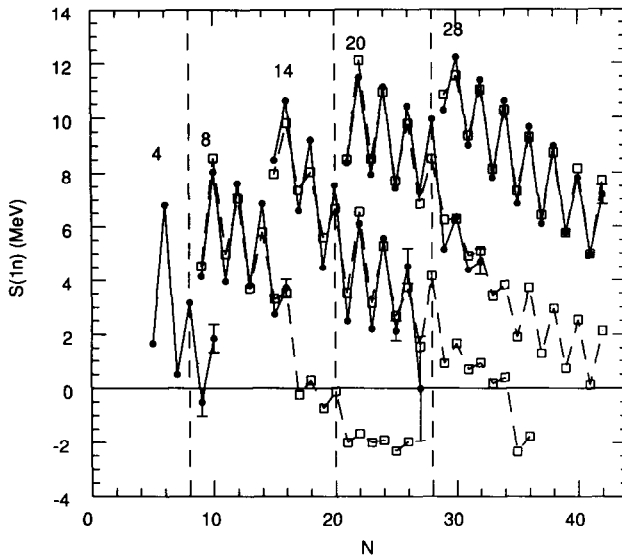


Figure 17: One-neutron separation energies for some selected Z values as a function of neutron number. The values for MSk7 HF (squares connected by dashed lines) are compared to experiment (circles connected by lines). The data are labeled by Z . The vertical dashed lines indicate the magic numbers 8, 20 and 28.

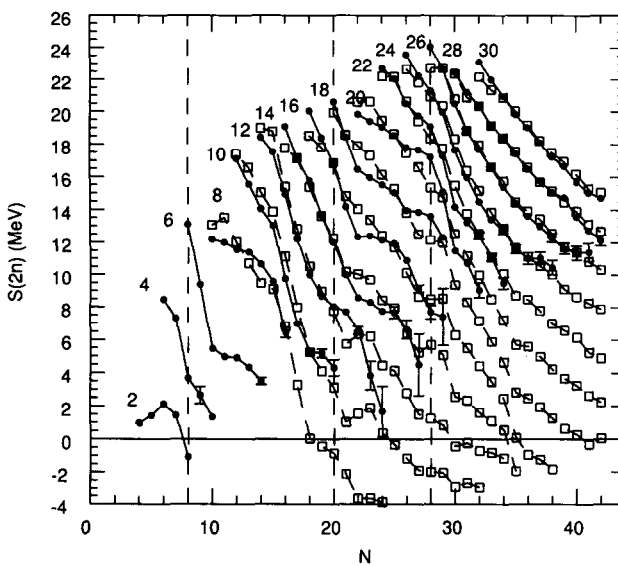


Figure 18: Two-neutron separation energies for even Z values as a function of neutron number. The values for MSk7 HF (squares connected by dashed lines) are compared to experiment (circles connected by lines). The data are labeled by Z . The vertical dashed lines indicate the magic numbers 8, 20 and 28.

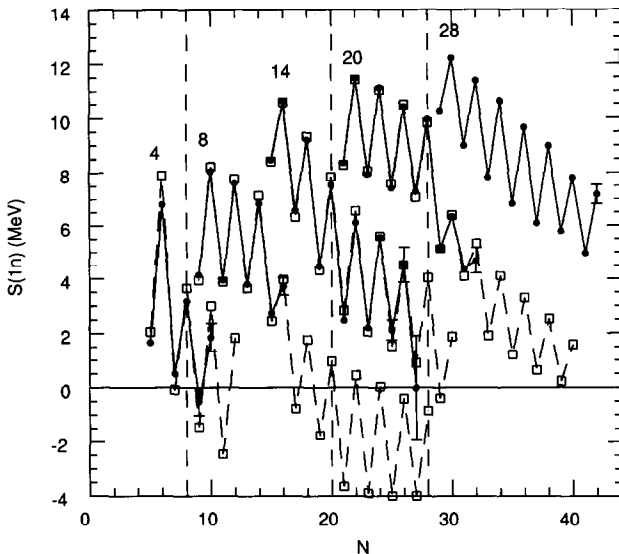


Figure 19: One-neutron separation energies for some selected even Z values as a function of neutron number. The results of shell-model configuration-mixing calculations discussed in the text (squares connected by dashed lines) are compared to experiment (circles connected by lines). The data are labeled by Z . The vertical dashed lines indicate the magic numbers 8, 20 and 28.

breaking in these nuclei.

The theoretical separation energies from shell-model configuration-mixing shown in Figs. (19) to (23) are based on $0\hbar\omega$ model spaces (which do not contain the intruder states) with hamiltonians WBT [73] for the p-sd shell, USD for the sd-shell [3], RCNP for the sd-pf shell ($N > 20$) [100], FPD6 [96] the calcium isotopes. Binding energies have been calculated for other pf shell nuclei [159] but not yet for the nuclei away from the valley of stability included in the figures.

One-neutron separation energies for some selected Z values are shown in Figs. (19) and (20). The overall agreement between experiment and theory is excellent. The largest deviations are for neutron-rich $Z = 4 - 5$ where the theoretical oscillation is larger than the experimental ones, which indicates that the pairing interaction is too strong. But in general the pairing properties of the nuclei near the neutron drip line (where the separation energies go to zero) are similar to those near the valley of stability. One can observe shell effects in odd-even oscillations which are well reproduced, for example, in the reduced pairing for $Z = 20$ and $N = 29 - 31$ which reflects the isolation of the $1p_{3/2}$ orbit.

The neutron drip line will be reached first for the odd- N one-neutron separation energies which are shown for even Z in Fig. (21). Note that this is the negative of the single-particle energy for states above the Fermi surface as defined by Eq. (2). Thus, for example, for $Z = 8$ the first three points are associated with the $0d_{5/2}$ SPE which is bound by about 4 MeV, the next point at $N = 15$ is related to the $1s_{1/2}$ SPE bound by about 3 MeV and the last three points (theory only) are related to the unbound $0d_{3/2}$ orbit. The largest deviation occurs for ${}^{29}\text{Ne}$ ($Z = 10$, $N = 19$) which is about 1 MeV more bound in experiment indicating the intruder nature of its configuration (see Sec. 5.4.2).

The two-neutron separation energies are given in Fig. (22) for even Z and (23) for odd Z . The most striking deviations are observed for $Z = 10 - 12$ and $N \geq 19$. There is a particularly large anomaly for $Z = 17$ and $N = 29$ in Fig. (23) indicating a sudden shape change at this point, but the

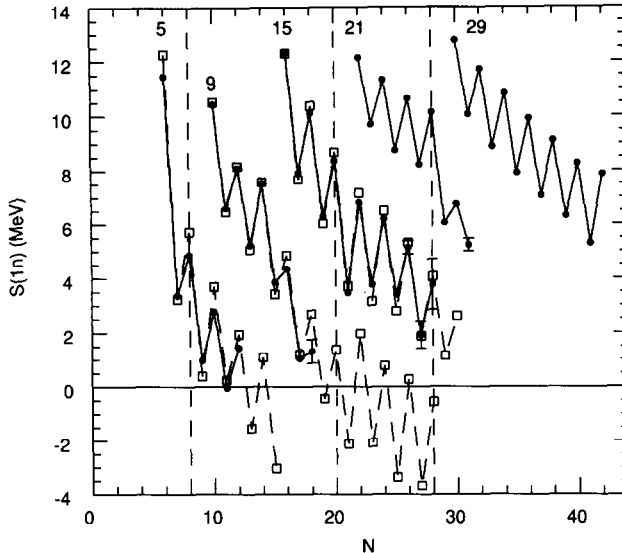


Figure 20: One-neutron separation energies for some selected odd Z values as a function of neutron number. The results of shell-model configuration-mixing calculations discussed in the text (squares connected by dashed lines) are compared to experiment (circles connected by lines). The data are labeled by Z . The vertical dashed lines indicate the magic numbers 8, 20 and 28.

experimental uncertainty is large, and this measurement should be confirmed. Also there is a flattening of the experimental curves for $Z = 24 - 27$ near $N = 40$, thus indicating an increase in deformation at this point and the importance of the $0g_{9/2}$ orbital (which is not in the calculations discussed here).

5.3 Proton-rich nuclei

As mentioned in the introduction, isospin symmetry is quite good in nuclei. It is broken by the long-range Coulomb interaction and by small charge-dependent parts of the strong interaction. Thus, the structure of a given proton-rich nucleus is similar to its isospin mirror in which the roles of protons and neutrons are interchanged (e.g. ^{18}Ne with $Z = 10$ and $N = 8$ compared to ^{18}O with $Z = 8$ and $N = 10$). Also there are associated isospin multiplets (e.g. the $T = 1$ triplet in ^{18}Ne , ^{18}F and ^{18}O).

In this section I will discuss some special features of proton-rich nuclei starting with a model for the difference in binding energy between mirror nuclei. The model applies to excited as well as ground states, but the discussion will be limited to ground states. Most of the calculations are based on the assumption that the structure (the valence configurations) of mirror nuclei are identical. This is not always the case, in particular when the structure is related to loosely-bound low- ℓ single-particle states. For example, the Thomas-Ehrman shift of the $1s_{1/2}$ orbital in ^{17}F is important for the changes in the structure of ^{18}Ne relative to ^{18}O . The Thomas-Ehrman shift of the $1s_{1/2}$ orbital is also responsible for level shifts in mirror excited states; one of the most dramatic cases is the astrophysically important 3^+ state in ^{18}Ne [160], [161], [162] which is shifted down by 0.86 MeV relative to its position in ^{18}O [163]. The isospin corrections to Fermi beta decay will be discussed in Sec. 5.9.1. Other special features of the proton-rich nuclei involve the narrow widths associated with one- and two-protons decays. The current status of diproton decay will be discussed in Sec. 5.3.4.

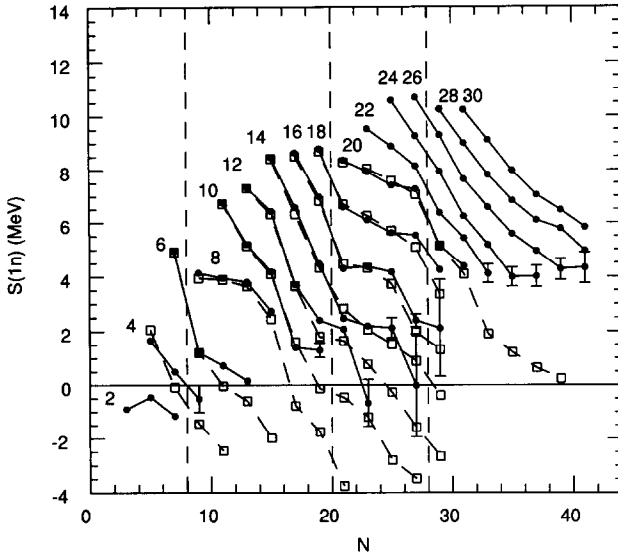


Figure 21: One-neutron separation energies for even Z and odd N values as a function of neutron number. The results from shell-model configuration-mixing calculations discussed in the text (squares connected by dashed lines) are compared to experiment (circles connected by lines). The data are labeled by Z . The vertical dashed lines indicate the magic numbers 8, 20 and 28.

5.3.1 Displacement energies

The displacement energy is the binding energy difference between mirror nuclei (those with the same atomic number A but with the proton number Z and neutron number N interchanged). For a given mass A and isospin T the displacement energy is:

$$D(A, T) = BE(A, T_z^<) - BE(A, T_z^>), \quad (12)$$

where $T = |T_z^<| = |T_z^>|$, $BE(A, T_z^<)$ is the binding energy of the proton-rich nucleus and $BE(A, T_z^>)$ is the binding energy of the neutron-rich nucleus. If the nuclear force is charge symmetric, then this binding energy difference can be related to the well-understood Coulomb interaction between the protons. However, it was shown by Nolen and Schiffer [164] that there is a systematic increase in the experimental displacement energies compared to those calculated with a charge symmetric strong interaction (the Nolen-Schiffer anomaly). In the usual HF calculation one has both direct and exchange terms in the Coulomb-energy density functional. For the exchange one uses the Fermi-gas approximation which is a good approximation to the exact calculation [165]. The ground-state displacement energies obtained with the Coulomb plus Coulomb-exchange HF approach (from the SKXce interaction of [11]) are shown on the right-hand side of Fig. (24). One observes the systematic deviation between experiment and theory associated with the Nolen-Schiffer anomaly. For the heaviest nuclei the ratio shown in Fig. (25) goes to a constant value of about 1.06. It is well known [164] that the displacement energies are sensitive to the rms charge radii; the SKX interactions reproduce the experimental charge radii of ^{16}O , ^{40}Ca and ^{48}Ca to better than one percent (see Fig. 10 of [11]). The displacement energies are also sensitive to the rms radius of the valence orbits, and the SKX interactions give radii for the $d_{5/2}$ orbit in ^{17}O and the $0f_{7/2}$ orbit in ^{41}Ca which are within 2% of those deduced from the magnetic electron scattering form factors [166].

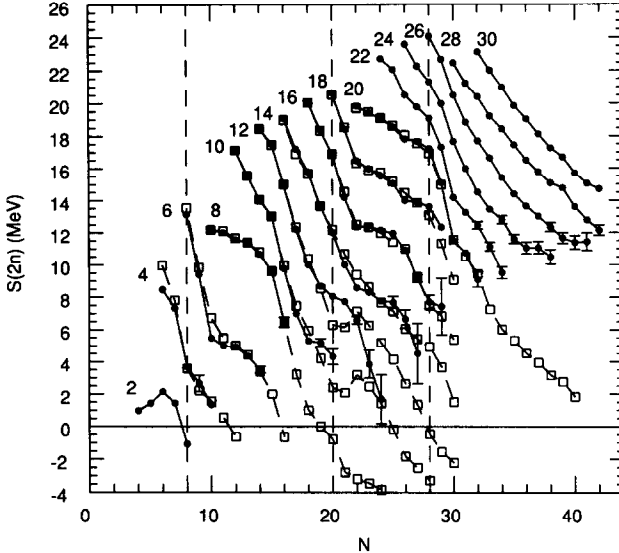


Figure 22: Two-neutron separation energies for even Z values as a function of neutron number. The results from shell-model configuration-mixing calculations discussed in the text (squares connected by dashed lines) are compared to experiment (circles connected by lines). The data are labeled by Z . The vertical dashed lines indicate the magic numbers 8, 20 and 28.

In the fit to closed-shell nuclei the displacement energy is represented by the pair of nuclei ^{48}Ni - ^{48}Ca . The binding energy of ^{48}Ni is not measured but can be extrapolated to within an uncertainty of a few hundred keV from the $0f_{7/2}$ shell displacement energy systematics [17], [167], [168], [8], [169]. The recent discovery of ^{48}Ni [18] is consistent with the mass obtained from the $0f_{7/2}$ extrapolations.

In order to improve agreement with experiment it was found that the HF theory could be improved in two ways. One of them consists of leaving out the Coulomb exchange term, with the result shown in the middle panel of Figs. (24) and (25). This may be interpreted as a correction from nuclear correlation (configuration mixing) which happens to cancel the exchange term. This has been discussed in the general HF framework by Bulgac and Shaginyan [170], [171], [172] in terms of a surface-vibration contribution to the Coulomb correlation energy. I note that the relativistic approach leaves out the Coulomb exchange by default, and that most Woods-Saxon programs [173], [174] leave out the Coulomb exchange.

Another way to improve agreement with experiment is to add a charge-symmetry breaking (CSB) term to the Skyrme interaction which can be expressed as a change to the proton-proton (pp) and neutron-neutron (nn) s -wave interactions:

$$V_{\text{Skyrme}}^{pp} = t_0(1 - x_0)(1 + x_a)\delta$$

and

$$V_{\text{Skyrme}}^{nn} = t_0(1 - x_0)(1 - x_a)\delta, \quad (13)$$

where x_a is a parameter to be determined.

The $A = 48$ closed shell nuclei require $x_a = -0.014 \pm 0.002$ for the interaction called SKXcsb. The results for the all displacement energies are shown on the right-hand side of Figs. (24) and (25).

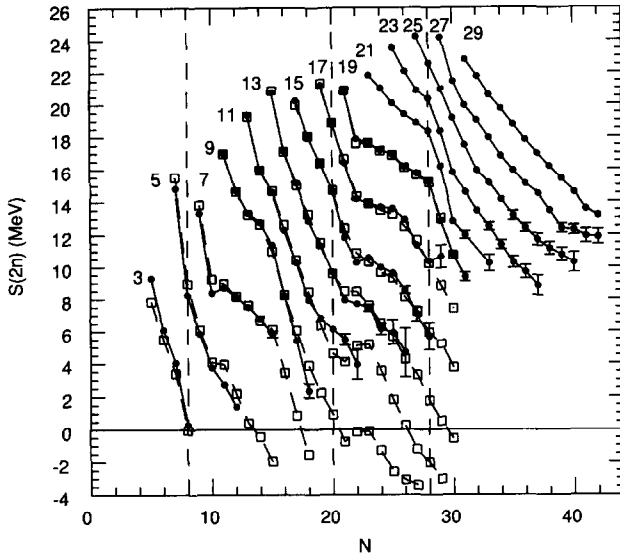


Figure 23: Two-neutron separation energies for odd Z values as a function of neutron number. The results from shell-model configuration-mixing calculations discussed in the text (squares connected by dashed lines) are compared to experiment (circles connected by lines). The data are labeled by Z . The vertical dashed lines indicate the magic numbers 8, 20 and 28.

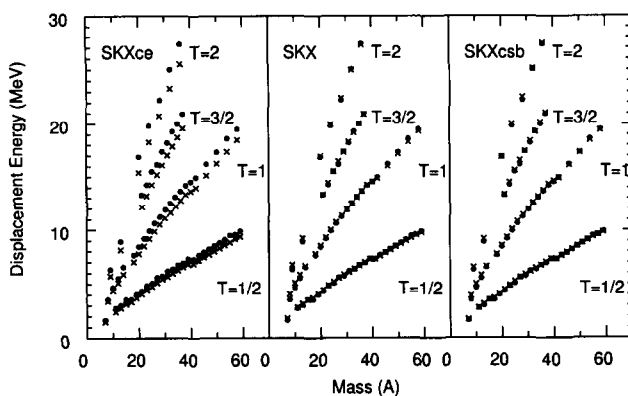


Figure 24: Ground-state displacement energies as a function of A for SKXce (with the normal Coulomb exchange term), SKX (without the exchange term) and SKXcsb (with the exchange term and with a CSB interaction). The experimental data are filled circles and the calculations are given as crosses.

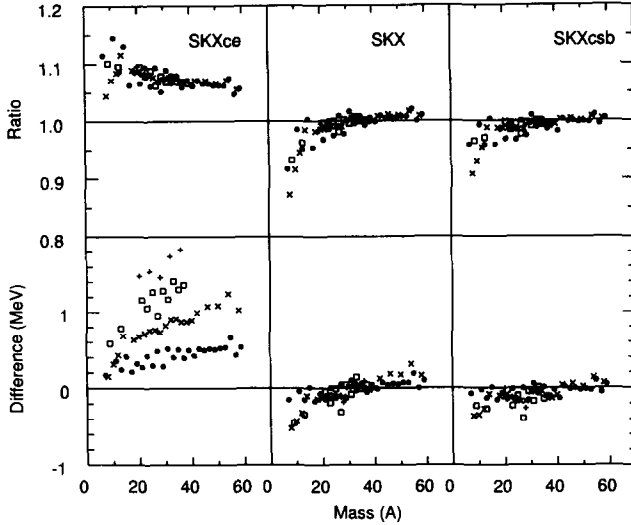


Figure 25: Top: the ratio experiment/theory for the data shown in Fig. (24); Bottom: the difference experiment-theory. The symbols are filled circles for $T = 1/2$, crosses for $T = 1$, squares for $T = 3/2$ and plus signs for $T = 2$.

A correct description of the displacement energies within the mean field approximation is obviously important for understanding the position of the proton drip lines. $A = 99$ is the heaviest $T = 1/2$ isobaric doublet for which the proton-rich nucleus is expected to be bound. The calculated displacement energies for $A = 99$ are -13.54 MeV (SKXce), -14.03 MeV (SKX) and -14.15 MeV (SKXcsb). The introduction of the extra terms in the Skyrme hamiltonian which are needed for the displacement energies, also has an influence on the neutron drip line; for example the binding energy of ^{176}Sn is predicted to be -1158.0 MeV (SKXce), -1149.0 MeV (SKX) and -1148.4 MeV (SKXcsb).

The SKXcsb interaction should ultimately be related to the CSB nucleon-nucleon (NN) scattering data. Analysis of the NN scattering data together with a model for the NN interaction gives [175], [176] a value of $\Delta a_{CSB} = a_{pp} - a_{nn} = 1.5 \pm 0.5$ fm for the difference in the pp and nn scattering lengths. Modern NN potentials such as the AV18 [177] and CDbonn99 [178] are designed to reproduce this difference. It is not easy to interpret the CSB contribution to the displacement energies directly in terms of a NN potential due the short-range nuclear correlations and their dependence on the strong NN potential. Probably the most realistic way to do this is to consider the CSB contribution to the displacement energies obtained with the variational Monte Carlo approach for $A = 7$ [6] and the BHF approach for $A = 15$ and $A = 17$ [178]. For example, the CSB displacement energy for the $A = 17$, $d_{5/2}$ state is 92 keV with AV18 [178] to be compared with 355 keV with SKXcsb. From these comparisons one finds that the effect of the empirical CSB interaction obtained for SKXcsb is a factor of 3–4 larger than expected from AV18 or CDbonn99. Thus one concludes that either there is a significant NNN or many-body CSB contribution whose origin is unknown, or that a major part of the displacement energy anomaly is due to nuclear correlations. Possible many-body CSB effects at the quark level have recently been examined [179], [180].

5.3.2 Binding energies of proton-rich nuclei

The systematics associated with the Coulomb displacement energies can be used to obtain theoretical binding-energies of proton-rich nuclei from the experimental binding energies of neutron-rich nuclei. The displacement energies of Eq. (12) can be modeled on smooth systematics [167], [168], [181]; shell-model configuration mixing which contains the Coulomb and CSB interactions [17], [8], [169]; or on the mean-field models such as the one discussed in the previous subsection. One can combine the experimental binding energy for the neutron-rich nucleus $BE(A, T_z^>)_{exp}$ together with the calculated value for $D(A, T)$ to give an extrapolation for the proton-rich binding energy:

$$BE(A, T_z^<) = D(A, T)_{theory} + BE(A, T_z^>)_{exp}. \quad (14)$$

For most of the nuclei out to the proton drip line the binding energy $BE(A, T_z^>)_{exp}$ of the mirror neutron-rich nucleus is known to 100 keV or better. This method has been used to predict the binding energies and the drip line for $Z = 19 - 28$ [17], [169], [167] and $Z = 28 - 38$ [169], [9]. The latter calculations have been used [9] to study the rapid-proton (rp) capture path in the astrophysical explosive hydrogen burning process [182]. The rp-process in light nuclei depends upon theoretical calculations of the displacement energies of ground and excited states and upon the spectroscopic factors which enter into the (p, γ) reaction [183], [184].

5.3.3 Proton halos

The Coulomb barrier prevents loosely-bound protons from extending as far as the loosely-bound neutrons. One of the most extreme cases to consider is that for a loosely-bound $1s_{1/2}$ state, since the centrifugal barrier is small. The $1/2^+$ first excited state of ^{17}F which is bound by only 100 keV provides a good example. The valence radius of this state is calculated to be 5.5 fm [185]; twice as large as the rms radius of the ^{16}O core (2.7 fm). The $B(E2)$ for the transition to the ^{17}F ground state ($1s_{1/2} \rightarrow 0d_{5/2}$) is much larger than any other “single-particle” transition in this mass region [185]. The halo nature of this state is important for the astrophysical $^{16}\text{O}(p, \gamma)^{17}\text{F}$ reaction [78].

The ground state of ^8B which has a separation energy of 140 keV provides perhaps the best example which can be studied experimentally in more detail. The calculated $0p_{3/2}$ spectroscopic factor between the ^8B (2^+) and $^7\text{Be}(3/2^-)$ ground states is about unity [174] which means that ^8B can be viewed as a single loosely-bound proton outside of ^7Be . The quadrupole moment of this state has been discussed theoretically [186], [187]. ^8B has been extensively studied theoretically and experimentally in regard to the low-energy solar reaction $^7\text{Be}(p, \gamma)^8\text{B}$ reaction and the neutrinos produced from the ^8B beta decay [188].

The $1s_{1/2}$ orbital becomes the ground state in nuclei with $Z=15$ and $Z=16$. The nuclei which are closest to the proton drip line, i.e., ^{26}P , ^{27}P and ^{27}S ; provide the best proton halos [181]. The proton halo for these nuclei is related to the removal of a $1s_{1/2}$ proton to the ground state of the silicon isotopes. The components of the knockout reaction leading to difference final states have been analyzed in gamma coincidence experiments. The momentum distribution for the ground-state component (obtained by subtraction of the total from those in coincidence with gammas) is narrow as predicted for a $\ell=0$ proton halo [189].

5.3.4 Diproton decay

Nuclei have been observed to decay by a variety of processes which include fission, beta decay, gamma decay, alpha decay and proton decay. Diproton decay, which involves the simultaneous emission of two protons decay [16], is perhaps the next on this list, but it has proven to be the most elusive. The condition for this mode of decay is that single-proton decay $^A\text{Z} \rightarrow^{(A-1)} (Z-1)$ be energetically forbidden, and that the Q value for two-proton decay $^A\text{Z} \rightarrow^{(A-2)} (Z-2)$ be in a narrow range such

that its lifetime or decay width is experimentally accessible. The pairing interaction contribution to the nuclear binding energy gives the possibility for this situation to occur. In light nuclei it is often the case that there are broad intermediate states available to single-proton decay ${}^A Z \rightarrow {}^{A-1} (Z - 1)$ which gives a combination of sequential and direct modes of two-proton decay. This is the case for ${}^6 \text{Be}$ [190], ${}^{12} \text{O}$ [191], [192], and ${}^{16} \text{Ne}$.

Some cases which have been discussed for the observation of only the direct decay mode are ${}^{17} \text{Ne}$ [193], ${}^{18} \text{Ne}$ [194], ${}^{19} \text{Mg}$ [195], ${}^{39} \text{Ti}$, ${}^{45} \text{Fe}$, [17], [196] ${}^{48} \text{Ni}$ [18], [17], ${}^{54} \text{Zn}$, ${}^{59} \text{Ge}$, ${}^{63} \text{Se}$, ${}^{67} \text{Kr}$ and ${}^{71} \text{Sr}$ [169]. These nuclei are indicated by the crosses in Fig. (1). Recently the two-proton decay of an excited 1^- state in ${}^{18} \text{Ne}$ to the ${}^{16} \text{O}$ ground state has been observed [194] in which there are no intermediate states are known (except for a possible influence from the tails of broad excited states).

Decay models have recently been developed [197], [195], which take into account the final state interaction of the two-protons and are thus more realistic than the original two-body cluster estimates [17], [198]. The R-matrix model of Barker [197] incorporates the final state interaction between the two-protons in terms of the s-wave phase shift. This model provides the observed width Γ as a function of the reduced width γ^2 (Eq. 1 of [197]). The reduced width can be approximated by $\gamma^2 = \theta^2 \gamma_{WL}^2$, where θ^2 is the dimensionless spectroscopic factor, and $\gamma_{WL}^2 = 3\hbar^2/(2Ma^2)$ is the Wigner limit, with a being the channel radius in the R-matrix model.

The s-p-sd-pf model space has recently been used to calculate the spectroscopic factor for the ${}^{18} \text{Ne}$ 1^- decay with $1\hbar\omega$ wave functions for ${}^{18} \text{Ne}$ and a closed shell of ${}^{16} \text{O}$ [199]. The spectroscopic factor is based upon the SU3 cluster model [200], [201] with results of $\theta^2=0.043$, 0.024 and 0.075 obtained for MK, WBT and WBP, respectively. With Barker's value of $a = 1.45(A_1^{1/3} + A_2^{1/3}) = 5.5$ fm ($A_1 = 16$ and $A_2 = 2$), the Wigner limit is $\gamma_{WL}^2 = 1.03$ MeV, and Barker's R matrix gives $\Gamma/\theta^2 = 810$ eV ($L = 1$, $Q_{2p} = 1.83$ MeV), resulting in diproton widths of 35, 19 and 61 eV for MK, WBT and WBP respectively. The experimental width for diproton emission is 21 ± 3 eV [194]. Although WBT yields the best agreement with experiment, there is probably an error of at least a factor of two in the decay model. The dominant decay mode of the ${}^{18} \text{Ne}$ 1^- state is by single-proton emission to the low-lying bound states of ${}^{17} \text{F}$. The shell-model calculation for this one-proton emission agrees with experiment within a factor of two. There is also a broad $3/2^+$ level at 5 MeV in ${}^{17} \text{F}$ whose low-energy tail could give some sequential proton decay – further experiments are needed to check this.

Results for the diproton decay of ${}^{19} \text{Mg}$ and ${}^{48} \text{Ni}$ are given by the three-body decay model [195]. The R-matrix value for the diproton decay of ${}^{19} \text{Mg}$ ($L = 0$) with $Q_{2p} = 1.408$ MeV gives a width of 50×10^{-7} MeV ($\theta^2=1$) compared to the three-body model result of 8×10^{-7} MeV (with $\theta^2=1$, the cluster spectroscopic factor is not yet calculated). However, the three-body model may contain an implicit spectroscopic factor for the simple $(0d_{5/2})^2$ model assumed. It is not clear how the many-body (shell-model) spectroscopic factor can be used in the three-body model.

${}^{48} \text{Ni}$ remains the most exciting case for finding the diproton decay of a ground state, its existence has only recently been confirmed [18]. The Q value for diproton decay has been extrapolated from the displacement energy systematics as $1.36(13)$ MeV [17] and the pf shell spectroscopic factor is $\theta^2=0.14$ [17]. Barker's R matrix model gives $T_{1/2} = 0.030$, 0.48 and 20 ms for $Q=1.49$, 1.36 and 1.23 MeV, respectively. The calculated beta decay half-life is 9.2 ms [17]. The three-body model [195] gives $T_{1/2} \approx 10$ ms for $Q=1.36$ MeV.

5.4 Intruder states

In a given model space for a given nucleus one will always eventually encounter an experimental level whose configuration is outside the model space description. These are often called intruder states. This is particularly important for the nuclei near the magic numbers which determined the boundary of the region covered by the model space. The meaning of intruder is relative to the defined model space and in this review intruder states will refer to those which have configurations which are outside $0\hbar\omega$ model

spaces. This corresponds to the excitations of protons and/or neutrons across one of the LS closed shells, p, sd or pf. (In heavy nuclei intruder usually refers to the excitation across the jj closed shells).

Particle-hole excitations (involving one or many particles and holes) across the shell gap near magic numbers always appear much lower in excitation energy than one would estimate from the single-particle hamiltonian due to the correlations. This situation is well known in nuclei near the valley of stability, in for example, ^{16}O which has a low-lying “4p-4h” band. In some situations these correlations result in a degeneracy or inversion relative to the normal spherical state, producing a ground state whose structure involves particle-hole excitations across the shell gap. The most well known regions where this occurs are for the nuclei around ^{12}Be and ^{32}Mg . These intruder ground states might be misinterpreted in terms of a vanishing shell gap. But there are two factors which play a role in their formation. One of them is a weakening of the shell gap as one approaches the drip line. This is related to the closer spacing of the least bound single-particle states and the lowering of the low- ℓ relative to their position in nuclei near the valley of stability. I will give some examples. Another factor is that the structure of the intruder state must involve the protons and neutrons in configurations with a large number of degrees of freedom for pairing and quadrupole correlations compared to that of the normal ground state. There are regions of heavier nuclei which have not yet been explored where this inversion may occur. The next location related to the LS closed shell would be around ^{62}Ti relative to the $N = 40$ gap. For heavier nuclei, the intruder states would be associated with jj closed shells. Although the jj intruder states come low in energy, for example in the nuclei around ^{186}Pb [202], I am not aware of a situation where they come below the normal ground state. One possibility is near ^{80}Zn for the $N = 50$ closed shell; it will be interesting to have more detailed experiments for this region. A theoretical and experimental understanding of intruder states is crucial for the r-process path.

Intruder states can be incorporated within the model space as recently shown by Utsuno [39] in the case of the ^{32}Mg region. A more qualitative understanding of intruder states in terms of shell gaps and correlation energies is provided shape coexistence models [203], [204], [205]. Shape coexistence includes as an extreme the superdeformed bands in deformed HF calculations involving orbitals far removed from those around the spherical Fermi surface [206].

5.4.1 Intruder states near ^{12}Be

The $1/2^+$ ground state of ^{11}Be is one of the oldest examples of intruder states [207]. It lies 300 keV below the $1/2^-$ state which is described in terms of the p-shell model space for this mass region. The intruder state has one neutron excited from the p shell into the sd-shell (leaving two neutron holes in the p shell). The shell gap for ^{16}O is about 11 MeV, but the intruder state comes much lower in energy. The wave functions generated in the larger $1\hbar\omega$ model space involving both p and sd shells have been used to interpret the reason for the inversion [208] in terms of three effects: (a) a reduction of the p-sd shell gap from its value of 11 MeV in ^{16}O to about 4 MeV in ^{12}Be , (b) an increase in the monopole pairing energy due to an opening up of the pairing degrees of freedom for the two neutron holes in the p shell, and (c) deformation due to the proton-neutron interaction. The spectroscopic evidence for the deformation will be discussed in Sec. 5.5.

I show in Fig. (26) the SKX and experimental neutron SPE relative to $0\text{p}_{1/2}$ for $N = 8$ as a function of Z . The error bar shown for the $1s_{1/2}$ state at $Z = 4$ indicates that this state is unbound and has a decay width. (A similar comparison for the absolute SPE with the SGII Skyrme interaction is shown in Fig. 1 of [208].) The SKX shell-gap decreases with Z mainly due to the lowering of the $1s_{1/2}$ orbit. This is due to the increase in the density of single-particle states as one approaches the top of the potential well. As mentioned previously the SKX gap for ^{16}O ($N = 8$) is smaller than experiment, and I attribute this to p-sd configuration mixing in ^{16}O . For the more neutron-rich nucleus ^{14}C ($N = 6$) the SKX agreement with experiment is better, indicating that the p-sd mixing is smaller in ^{14}C than ^{16}O .

In the $N = 7$ isotones the $1\hbar\omega$ excitation in which one neutron is excited from the p shell to the

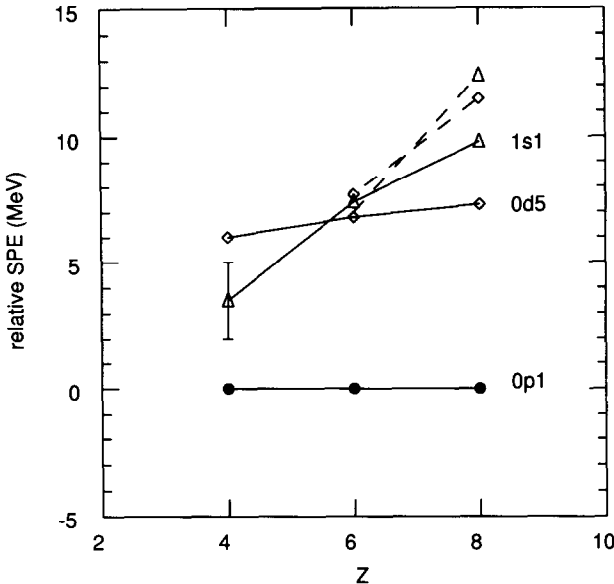


Figure 26: Neutron SPE for $N = 8$ for $0d_{5/2}$ (diamonds) and $1s_{1/2}$ (triangles) relative to $0p_{1/2}$ (filled circles). The symbols connected by lines represent SKX HF results, and the symbols connected by dashed lines are the data deduced from experimental binding energies.

sd shell starts out at 3.09 MeV in ^{13}C , drops to 2.02 in ^{12}B (the centroid of the $1^- - 2^-$ doublet) and then remains the ground state in ^{11}Be , ^{10}Li [209], [210] and ^9He [211]. This trend is consistent with shell-model calculations in the $(0+1)\hbar\omega$ model [211].

There are excited configurations in ^{14}C corresponding to $1\hbar\omega$ (the 1^- state at 6.09 MeV) and $2\hbar\omega$ (the 0^+ state at 6.59 MeV) excitations from the p-shell into the sd-shell. The $1\hbar\omega$ excitation energy is higher in $N = 8$ than $N = 7$ since for $N = 8$ there is only one neutron hole in the p shell and there is no energy gain from the p-shell pairing. The $2\hbar\omega$ excitation is lowered from its single-particle energy spacing by the energy gain from both proton and neutron pairing as well as from the proton-neutron interaction. In the calculation with the WBT and WBP interactions, the $2\hbar\omega$ excitation drops to 2.7 MeV in ^{13}B [212] and then becomes degenerate with the $0\hbar\omega$ configuration in ^{12}Be and ^{11}Li [213]. The consequence of this degeneracy for the spectroscopic factors is discussed in Sec. 5.5.

The discussion above involves pure $N\hbar\omega$ configurations or coexistence in which the mixing between, for example, $0\hbar\omega$ and $2\hbar\omega$, is not considered. It is possible to extend the model space to include mixing, but there are two problems to overcome. One is that most interactions (WBP and WBT in particular) are designed for the pure $N\hbar\omega$ model space. This interaction is implicitly renormalized to account for the $N\hbar\omega$ mixing which is not in the model space. The application to mixed $\hbar\omega$ will require a new interaction which is differently renormalized to be compatible with the larger model space. The second problem concerns the convergence of the spectrum in terms of the number of $\hbar\omega$ excitations. For example, to obtain a spectrum for ^{16}O one may mix $2\hbar\omega$ into the $0\hbar\omega$ ground state (which is computationally easy). The result of this procedure is that the mixed ground state is lowered in energy by about 11 MeV relative to that of the pure $0\hbar\omega$ (closed shell) configuration. The equivalent level of mixing and energy shift for the excited 0^+ “4p-4h” ($4\hbar\omega$) state would require the addition of $6\hbar\omega$ (which is computationally not so easy). It may take up to about $10\hbar\omega$ for convergence but this is beyond the present level of

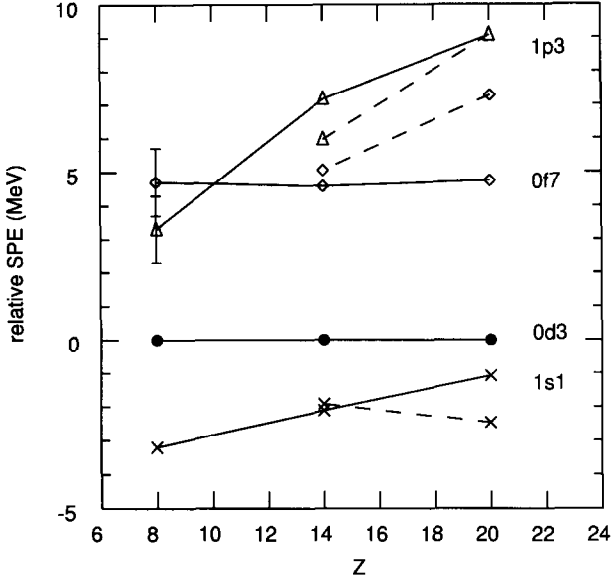


Figure 27: Neutron SPE for $N = 20$ for $0f_{7/2}$ (diamonds), $1p_{3/2}$ (triangles), and $1s_{1/2}$ (crosses) relative to $0d_{3/2}$ (filled circles). The orbits are labeled by $(n, \ell, 2j)$. The symbols connected by lines represent SKX HF results, and the symbols connected by dashed lines are the data deduced from experimental binding energies.

computation.

The Monte-Carlo methods can be applied to the full p-sd model space which would include up to 12p-12h within the p-sd shell, but would be very incomplete in terms of the full set of $\hbar\omega$ excitations needed for the treatment of and spurious states. Although technically possible, Monte-Carlo calculations for this model space have not been reported. Monte-Carlo calculations in the sd-pf model space for the region of ^{32}Mg have been carried out [38], [39] but in this case the resulting wave functions involve mainly neutron excitation from sd to pf for which the spurious state problem is not so severe.

Some calculations which include mixing up to $4\hbar\omega$ have been carried out. The truncation problem require that the energies of the higher $\hbar\omega$ configurations be shifted down in order to compensate for the truncation [26] or by reducing the shell gap [214].

5.4.2 Intruder states near ^{32}Mg

The anomalies in the binding energies, excitation energies, half-lives and radii of the most neutron rich sodium and magnesium isotopes relative to the $0\hbar\omega$ calculations have been known for some time [215], [216], [217]. The early deformed HF calculations indicated the importance of the pf shell [217] and the pf shell was soon incorporated into the model space [218], [137].

The WBMB interaction was used to calculate the energy of the pure $N\hbar\omega$ ($N=1-4$) configurations in a full $N\hbar\omega$ space for some nuclei and with the weak-coupling approximation for other nuclei in this mass region. The weak-coupling approximation provides some insight into the nature of these intruder states and ties them together with intruder states in other mass regions such as ^{16}O and ^{40}Ca [219], [220], [221], [222], [223] and with those in heavy nuclei [203], [204], [205]. In weak coupling one obtains the excitation energy of m-particle n-hole configurations relative to a closed shell in terms of the properties

of the pure m-particle and n-hole configurations in the nuclei m and n nucleons removed from the closed shell. The basic assumption is that the average particle-hole interaction \bar{V}_{ph} is weak and does not change the structure of the pure m-particle and n-hole configurations in when they are put together. The total particle-hole interaction is estimated by $mn\bar{V}_{ph}$. One can either calculate the energies of the configurations represented by the pure m-particle and n-hole configurations or use experimental binding energies to obtain them [55], [224].

Warburton and Brown [98] used the weak-coupling model in the region of ^{32}Mg to obtain the boundaries of the island of inversion. The result is that there is an island of nuclei, $^{32-34}\text{Mg}$, $^{31-33}\text{Na}$ and $^{30-32}\text{Ne}$, whose $1\hbar\omega$ and $2\hbar\omega$ configurations come lower in energy than the $0\hbar\omega$ configuration, and there are many others for which the $1\hbar\omega$ configuration is essentially degenerate with the $0\hbar\omega$ configuration analogous to the $1/2^-$, $1/2^+$ doublet in ^{11}Be . The three mechanisms discussed in the previous section also apply here: a reduction in the shell gap, the pairing correlations, and the proton-neutron (deformed) correlations.

The $\Delta_d = e(0f_{7/2}) - e(0d_{3/2})$ energy gap is an important ingredient in the relative spacing of the $0\hbar\omega$ (spherical) and $2\hbar\omega$ (deformed) configurations in ^{32}Mg [144]. I show in Fig. (27) the SKX and experimental neutron SPE relative to $0d_{3/2}$ for $N = 20$ as a function of Z . The experimental SPE for ^{34}Si are based upon the recent experiments for ^{33}Si [225] and ^{35}Si [136]. The error bars for the $1s_{1/2}$ state at $Z = 8$ indicate that these states are unbound and have a decay width. (For a comparison with other Skyrme interactions see Fig. 6 of [144].)

The SKX shell-gap is nearly constant with Z except for near $Z = 8$ where the low- ℓ $1p_{3/2}$ crosses over. This situation is similar to the low-lying $1s_{1/2}$ state for $N = 8$ shown in Fig. (26). The degeneracy of $1p_{3/2}$ and $0f_{7/2}$ for low Z increases the pairing correlations (see Fig. 24 in [144]) as well as allowing for larger deformation from the quadrupole mixing of these two orbits.

As discussed in Sec. 5.1, the SKX gap for ^{40}Ca ($N = 20$) is smaller than that deduced from experiment, and I attribute this to sd-pf configuration mixing in ^{40}Ca . For the neutron-rich nucleus ^{34}Si the SKX SPE are in better agreement with experiment, indicating that the sd-pf mixing is smaller in ^{34}Si than in ^{40}Ca . The SKX extrapolation to $Z = 8$ (^{28}O) gives a sd-pf gap of about 4 MeV. Shell-model configuration mixing also provides extrapolations for this gap which may sometimes be less reliable than the HF model. For example, the ESPE obtained with the Utsuno interaction shown in Fig. 5 of [39] has an sd-pf gap of only about 2 MeV at ^{28}O , which is inferred from the drip-line properties of the nuclei in this region [149], and is related to an increase in the $1s_{1/2}-0d_{3/2}$ spacing. But the interpretation in terms of a small shell gap may be influenced by the model space truncation (to $0f_{7/2}$ and $1p_{3/2}$) and to the uncertainty in the residual interaction in these exotic nuclei near the neutron continuum. The position of the single-particle states in these nuclei near the neutron drip line can be tested by finding the excited states of ^{24}O corresponding to the $1s_{1/2} \rightarrow 0d_{3/2}$ excitation to the 2^+ state and the $0d_{5/2} \rightarrow 0f_{7/2}$ and $1s_{1/2} \rightarrow 1p_{3/2}$ excitations to the low-lying dipole (1^-) states. In particular the 2^+ energy in ^{24}O is predicted at 4.18 MeV with USD and 5.5 MeV with the Ustuno interaction [21] (the neutron separation energy of about 3.7 MeV means that these states are probably unbound to neutron decay).

Calculations in the mixed $\hbar\omega$ sd-pf model space have recently been carried out [38], [39]. The results of [39] confirm the picture of the island-of-inversion but provide details concerning the mixing between $0\hbar\omega$ and $2\hbar\omega$ and the importance of $4\hbar\omega$. This is illustrated in Fig. (28) from Ref. [39]. This shows number of sd to pf neutron excitations beyond the $0\hbar\omega$ model for the silicon, magnesium and neon isotopes. The dashed line represents the idea of coexistence where $2\hbar\omega$ comes below $0\hbar\omega$ in magnesium and neon for $N = 20$ and $N = 22$ and two neutrons are excited. The QMCD calculations show that the island does not have steep cliffs, but that there is a more gradual beach. For ^{28}Ne with $N = 18$ there is close to 50% admixture of $0\hbar\omega$ and $2\hbar\omega$ which indicates the degeneracy of these two configurations [226]. ^{31}Na is in the middle of the island-of-inversion. It has recently been experimentally confirmed that there is a low-lying state [227] indicative of the collective structure first pointed out in $(0+2)\hbar\omega$ calculations [138]. The experimental information in this region of neutron-rich nuclei is expected to be

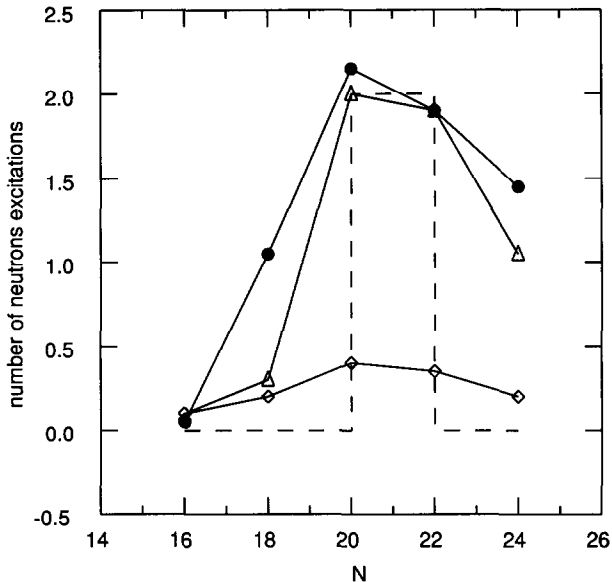


Figure 28: Number of sd to pf neutron excitations as a function of neutron number for neon (circles), Mg (triangles) and Si (diamonds) based on the QMCD calculations of [39]. The dashed line is the expectation for the pure $N\hbar\omega$ states in the island of inversion [99].

greatly expanded over the next decade.

5.5 Spectroscopic factors

Nucleon spectroscopic factors are among the most fundamental tests of shell-model wave functions [228]. Until recently experiments were only possible for one-nucleon transfer reactions on stable nuclei. [229]. With radioactive beams one can carry out transfer reactions with inverse kinematics [230]. In addition, a new method has been developed [231], [232] which makes use of the large cross sections for the knockout of the loosely-bound neutrons in high-energy reactions (typically above 50 MeV/nucleon). An example of the knockout reaction is ${}^9\text{Be}({}^{11}\text{Be}, {}^{10}\text{Be} + \gamma)X$ where one neutron is removed from the ${}^{11}\text{Be}$ radioactive beam leading to excited states in ${}^{10}\text{Be}$ which are tagged by the gamma rays in coincidence with ${}^{10}\text{Be}$ [233]. The reaction leading to the ground state of ${}^{10}\text{Be}$ is deduced from the difference between the total cross section and that in coincidence with gammas. The momentum distribution of ${}^{10}\text{Be}$ provides information on the ℓ value of the knocked out neutron. At these high energies the reaction mechanisms simplifies and they can be treated in the eikonal model [75], [234] as a sum of stripping and diffraction dissociation mechanisms.

Spectroscopic factors obtained from recent experiments for one-neutron removal in coincidence with gamma rays [233], [213], [212], [235], [236], [232] are summarized in Table 4. The results in Table 4 are for the lowest few states in the final nucleus, although other states up to the neutron decay threshold are observed as discussed in these references. The sum-rule for the neutron-removal spectroscopic factor is the total number of neutrons N . The difference between N and the theoretical strength given in Table 4 is that the remaining strength resides in more highly excited states in final nucleus most of which are unbound to neutron decay. The total one-neutron removal cross sections have for these and

other nuclei are in good agreement with the WBT (WBP) calculations [237]. To be consistent with the original references, the theoretical results in Table 4 are from WBT for ^{10}Li , ^{11}Be , ^{12}Be and ^{14}B ; WBP for $^{15,16,17,19}\text{C}$ and USD for ^{23}O and ^{24}F .

The spectroscopic factors for the low-lying states are those for the most loosely-bound nucleons near the Fermi surface. The spectroscopic factors were extracted using an overlap function which is generated by a single-particle state in a Woods-Saxon potential with a geometry of $r_0 = 1.25$ fm and $a = 0.70$ fm and with a well-depth determined by reproducing the one-nucleon separation energy in Table 4. The experimental spectroscopic factors are in good overall agreement with the theory based upon the WBP and WBT interactions. I will discuss the details below. The Woods-Saxon geometry has been chosen mainly for consistency and the absolute spectroscopic factors will be uncertain at the levels of 10-20% until a more microscopic model for the overlap function is used. For example, use of the SKX HF radial wave function for the $1s_{1/2}$ orbit in ^{15}C gives a spectroscopic factor of 0.90 compared to the Woods-Saxon value of 0.74 in Table 4 [236].

The results for ^{11}Be are important for understanding the structure of this $1\hbar\omega$ intruder ground state discussed in Sec. 5.4.1. The spectroscopic factors to the lowest 2^+ state measures the deformed component and is in good agreement with WBP and WBT. These spectroscopic factors have also been measured in inverse kinematics [230]. The spectroscopic factors obtained in a coupled channel analysis of the inverse reaction are in agreement with those from the knockout reaction.

A consequence of the intruder state in ^{11}Be is that the shell-model ground state of ^{12}Be is complicated. The $0\hbar\omega$ and $2\hbar\omega$ (intruder) configurations have degenerate energies with the WBP and WBT interactions which would give a ground state which is a 50% mixture of these. The ^{12}Be beta decay has also been used as a more indirect measure of the $2\hbar\omega$ admixture [238], [239], [127]. The spectroscopic factors in Table 4 are based upon this 50% mixture. The agreement with experiment is fair, and it can be improved by taking a ground state which is 33% $0\hbar\omega$ and 67% $2\hbar\omega$ in the framework of the WBT2 calculation [213]. The $0d_{5/2}$ strength suggested by the shell model is not yet detected since it leads to a neutron unbound $5/2^+$ state in ^{11}Be . An excited 0^+ state in ^{12}Be has been suggested at 2.7 MeV [240] which would be the component orthogonal to the mixed ground state. However, there is also a 1^- state at 2.7 MeV [241] and it would be important to confirm the existence of a 0^+ state at this energy and measure its structure in a one-nucleon transfer reaction. The structure of the mirror nucleus ^{12}O will be similar to that of ^{12}Be , but one should expect a larger $(1s_{1/2})^2$ component in ^{12}O due to the Thomas-Ehrman shift of the $1s_{1/2}$ relative to $0p_{1/2}$ orbitals observed in the $1/2^+$ and $1/2^-$ states of ^{13}N and ^{13}C .

Single-nucleon removal cannot be measured for ^{11}Li since ^{10}Li is unbound. But from the correlation of the two-neutrons in a reaction leading to ^9Li it has recently been inferred that the $0p_{1/2}$ and $1s_{1/2}$ components are about equal [242]. With WBP and WBT the energies of the $0\hbar\omega$ and $2\hbar\omega$ configurations are degenerate, and this leads to a wave function which is 50% $0\hbar\omega$ and 50% $2\hbar\omega$ (as in ^{12}Be). The results for the spectroscopic factors for the lowest four states listed in Table 4. The resulting spectroscopic factors summed over all states in ^{10}Li are 1.00, 0.67 and 0.33 for $0p_{1/2}$, $1s_{1/2}$ and $0d_{5/2}$, respectively. The $1s$ to $0p$ ratio is in fair agreement with experiment, but the smaller $0d_{5/2}$ component has not yet been detected experimentally. ^{11}Li and ^{12}Be have similar structure in terms of the mixed $0\hbar\omega$ and $2\hbar\omega$ properties, the main difference is that ^{11}Li is less bound than ^{12}Be . A calculation [243] for the excited states of ^{11}Li in $(0+2)\hbar\omega$ and $(1+3)\hbar\omega$ model spaces gives several states below 3 MeV in excitation ($3/2^-$, $3/2^+$, $1/2^-$, $1/2^+$).

The structure of ^{13}Be (unbound) [244] and ^{14}Be [245] are also complicated and will require the consideration of at least the 0, 1 and 2 $\hbar\omega$ configurations. The $0\hbar\omega$ structure of ^{14}Be with WBT has neutron components of 53% $(0d_{5/2})^2$, 40% $(1s_{1/2})^2$ and 7% $(0d_{3/2})^2$ which is consistent with a recent dissociation experiment [245].

Above Z=4 the $0\hbar\omega$ configuration is well separated below the higher $\hbar\omega$ configurations, and the experimental data are consistent with the dominance of the $0\hbar\omega$ neutron sd-shell components. The

Table 4: Spectroscopic factors for neutron-rich nuclei. 0d for the orbit indicates the sum of the $0d_{5/2}$ and $0d_{3/2}$. The separation energies are based on the Audi-Wapstra mass table [155]. The core energy is from experiment except for ^{10}Li , ^{22}O and ^{23}F which are taken from the calculations.

Initial State	Core State	Core J^π	Core Energy (MeV)	orbit	C^2S theory	C^2S exp	separation energy (MeV)	exp reference
$^{11}\text{Li } 3/2^-$	^{10}Li	2^-	0.0	$1s_{1/2}$	0.40		0.4	
				0d	0.09		0.4	
		1^+	0.6	$0p_{1/2}$	0.33		0.6	
		1^-	1.3	$1s_{1/2}$	0.15		1.3	
$^{11}\text{Be } 1/2^+$	^{10}Be	0^+	0.0	$1s_{1/2}$	0.74	0.87(13)	0.5	[233]
		2^+	3.4	$0d_{5/2}$	0.18	0.17(4)	3.9	
$^{12}\text{Be } 0^+$	^{11}Be	$1/2^+$	0.0	$1s_{1/2}$	0.51	0.53(7)	3.2	[213]
		$1/2^-$	0.3	$1p_{1/2}$	0.91	0.45(7)	3.5	
		$5/2^+$	1.8	$0d_{5/2}$	0.40		5.0	
$^{14}\text{B } 2^-$	^{13}B	$3/2^-$	0.0	$1s_{1/2}$	0.66	0.82(11)	0.9	[212]
				0d	0.31	0.27(6)	0.9	
$^{15}\text{C } 1/2^+$	^{14}C	0^+	0.0	$1s_{1/2}$	0.98	0.74(9)	1.2	[235], [236]
$^{16}\text{C } 0^+$	^{15}C	$1/2^+$	0.0	$1s_{1/2}$	0.60	0.64(12)	4.2	[232]
		$5/2^+$	0.7	$0d_{5/2}$	1.23	1.29(20)	4.9	
$^{17}\text{C } 3/2^+$	^{16}C	0^+	0.0	$0d_{3/2}$	0.03	0.33(17)	0.7	[232]
		2^+	1.8	$1s_{1/2}$	0.16	0.12(5)	2.5	
				0d	1.44	1.19(30)	2.5	
$^{19}\text{C } 1/2^+$	^{18}C	0^+	0.0	$1s_{1/2}$	0.58	0.7(3)	0.6(2)	[232]
		2^+	1.6	0d	0.48		2.2	
$^{23}\text{O } 1/2^+$	^{22}O	0^+	0.0	$1s_{1/2}$	0.80		2.7	
		2^+	3.4	0d	2.13		6.1	
		0^+	4.6	$1s_{1/2}$	0.11		7.3	
		3^+	4.8	0d	3.08		7.5	
$^{24}\text{F } 3^+$	^{23}F	$5/2^+$	0.0	$1s_{1/2}$	0.74		3.8	
				0d	0.10		3.8	
		$1/2^+$	1.8	$0d_{5/2}$	0.07		5.6	
		$7/2^+$	2.9	0d	0.44		5.6	
				$1s_{1/2}$	0.01		6.7	

main complication comes from the crossing of the $1s_{1/2}$ and $0d_{5/2}$ orbits between oxygen and carbon. Thus the excited $1s_{1/2}$ state in ^{17}O becomes the $1s_{1/2}$ ground state in ^{15}C . The neutron pairing interaction for $N \geq 10$ makes a ^{16}C ground state which is about 50% $(1s_{1/2})^2$ and 50% $(0d_{5/2})^2$ in agreement with experiment. The analogous structures in $^{18,20,22}\text{C}$ are not yet measured, but ^{22}C is expected to be a very interesting Borromean halo nucleus with a large $(0s_{1/2})^2$ component (relative to the ^{20}C ground state) (see also Sec. 5.6). Borromean refers to the fact that the total three-body system of ^{20}C plus two neutrons is bound in spite of the fact that all of the two-body subsystems are unbound.

The theoretical spectra for both ^{17}C and ^{19}C have a triplet of low-lying levels with spin $1/2^+$, $3/2^+$ and $5/2^+$. The ordering of these levels differ between WBP and WBT. WBP gives a $3/2^+$ ground state with $5/2^+$ at 0.03 MeV and $1/2^+$ at 0.30 MeV for ^{17}C , and a $1/2^+$ ground state with $5/2^+$ at 0.19 MeV and $3/2^+$ at 0.62 MeV for ^{19}C . WBT gives a $5/2^+$ ground state with $3/2^+$ at 0.08 MeV and $1/2^+$ at 0.27 MeV for ^{17}C , and a $5/2^+$ ground state with $1/2^+$ at 0.5 MeV and $3/2^+$ at 0.40 MeV for ^{19}C . The present experimental results give $3/2^+$ for the ^{17}C ground state and $1/2^+$ for the ^{19}C ground state. Thus the WBP interaction is favored in this respect and is used for the theoretical spectroscopic factors given in Table 4. (The spectroscopic factors obtained for WBP and WBT are very similar.)

^{17}C is an interesting case where the proton-neutron interaction makes the $3/2^+$ “seniority three” configuration the ground state below (but near) the $1/2^+$ and $5/2^+$ states. The situation is analogous to ^{21}Ne [19] which also has a $3/2^+$ ground state. In most cases ground-state to ground state spectroscopic factors are large, but in this unusual case the transfer selection rule allows only for $0d_{3/2}$ which is a small part of the wave functions and leads to a small spectroscopic factor. With WBP the largest components of the ^{17}C $3/2^+$ state are 32% for $[(0p_{3/2})^8, (0p_{1/2})^2, (0d_{5/2})^3]$ and 31% for $[(0p_{3/2})^8, (0p_{1/2})^2, (0d_{5/2})^2, (1s_{1/2})^1]$, with the remaining 37% contained in many smaller components. The experimental spectroscopic factor is small but not as small as theory (it is obtained indirectly from a subtraction of all ^{16}C from those detected in coincidence with a gamma rays). The ^{17}C spectroscopic strength is large for the ^{16}C 2^+ state with a mixture of $1s_{1/2}$ and $0d_{5/2}$ which is confirmed experimentally.

For ^{19}C the halo nature of the momentum distribution in one-neutron knockout reactions indicates a $1/2^+$ ground state [232]. There is some uncertainty in the spectroscopic factor due to the uncertainty in the separation energy, and I take the results given in Table 4 from Fig. 8 of [232]. (A precise mass measurement of ^{19}C is needed.) With WBP the largest component of the ^{19}C $1/2^+$ state is 48% for $[(0p_{3/2})^8, (0p_{1/2})^2, (0d_{5/2})^4, (1s_{1/2})^1]$ with the remaining 52% contained in many smaller components. The $[(0d_{5/2})^4, (1s_{1/2})^1]$ configuration appears theoretically at an excitation energy of 1.33 MeV in ^{21}O with the USD interaction [22] (which is part of WBP), and may be associated with an experimental state observed at the same energy [246]. In the framework of WBP (and WBT) its energy is lowered in ^{19}C due to the 1.6 MeV downward shift of the $1s_{1/2}$ state relative to $0d_{5/2}$ between ^{17}O and ^{15}C .

Table 4 also provides a sample of some shell-model predictions for neutron-rich sd-shell nuclei which are currently being measured. ^{23}O has a large $1s_{1/2}$ spectroscopic factor to the ground state of ^{22}O . There is also a very large $0d_{5/2}$ spectroscopic to the excited states which could be observed in their gamma decay. For ^{24}F I give the result for the theoretical 3^+ ground state, but the 2^+ state lies only 97 keV higher [22] (a recent experiment [247] suggest that this 2^+ level may be at 522 keV), and for only the first three states in ^{23}F (there is an additional 5.6 units of strength, mainly $0d$, in higher states).

Spectroscopic factors for the addition of neutrons to neutron-rich nuclei are important for the r-process path [248]. Although the data discussed here on neutron removal are not directly applicable, they do provide a test of the energy levels, spins and structure for the models and interactions.

Spectroscopic factors for the interesting region of nuclei around ^{32}Mg with its intruder states is open territory both experimentally and theoretically. Neutron transfer reactions are needed to establish the structure of the nuclei with $N = 19 - 21$. As mentioned in Sec. 5.4.2 the $1p_{3/2}$ orbit should be nearly degenerate with $0f_{7/2}$ around $Z = 10$ and can be experimentally detected by the narrow momentum part of the knockout cross section. The properties of ^{31}Mg and ^{33}Mg are unknown and reactions on the neighboring even-even nuclei leading to these will be important to carry out.

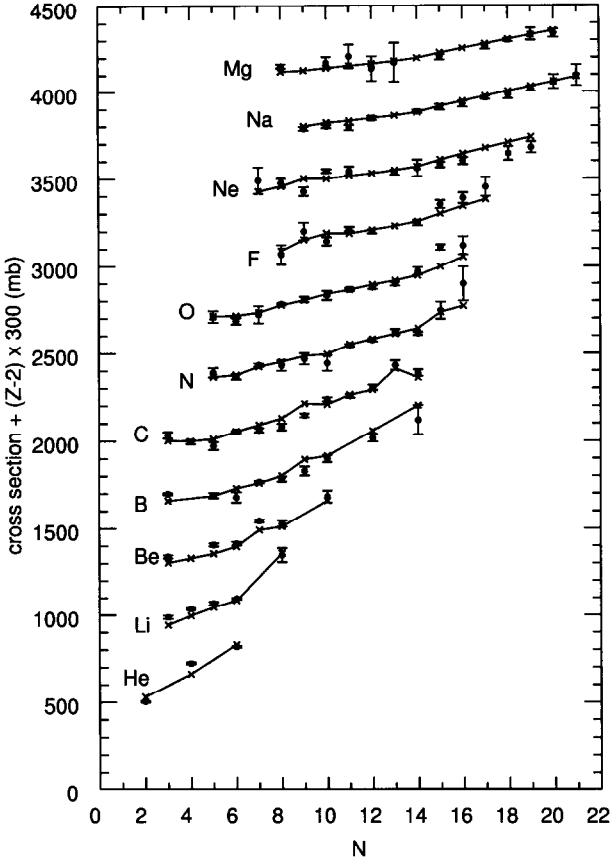


Figure 29: Experimental and theoretical total interaction cross sections. Note that the points are separated in Z by the addition of $300(Z - 2)$.

5.6 Interaction cross sections

The interaction cross sections of high-energy light radioactive beams provided one of the first clear indications for the existence of neutron halo phenomena [249]. Recent high-energy cross section data for $Z=6-9$ [250] together with other data [251] now provide a wider experimental picture for the interpretation of neutron halos and skins in light nuclei. One of the first microscopic theoretical interpretations for the cross sections data was given by the Glauber reaction model with matter densities obtained from a Hartree-Fock model [252]. The data are compared with an updated set of calculations based upon the SKX Skyrme interaction [11] in Fig. (29). The general features we discuss here emerge from all Skyrme interactions [253].

The reaction model is the zero-range Glauber model described in [252]. The experimental data for the cross sections on ^{12}C were taken from the compilation of Ozawa et al. [251] (The beam energies were 790-800 MeV/u for $Z = 2 - 5$ and 950-1020 MeV/u for $Z = 6 - 12$, with the exceptions of $^{10,11}\text{B}$ data taken at 950-960 MeV/u, and $^{9,10,11,15}\text{C}$, $^{12,13,17}\text{N}$, $^{13,14,15}\text{O}$, ^{17}F and ^{17}Ne data taken at 670-740 MeV/u.) The input to the Glauber model is an NN interaction with a range of $r_o = 1$ fm and effective

cross sections [254] of 40.0 mb for 680–740 MeV/u, 40.9 mb for 790 MeV/u and 44.0 mb for 950–1020 MeV/u.

The HF calculations start with an assumed simple filling of the orbits in the order $0s_{1/2}$, $0p_{3/2}$, $0p_{1/2}$, $0d_{5/2}$, $1s_{1/2}$ and $0d_{3/2}$. This is accurate enough for well-bound nuclei near stability. The single-particle energies from SKX agree with experiment to within 1–2 MeV [11]. As discussed in [252], when one approaches the neutron drip line the matter radii are sensitive to the single-particle energies and the related separation energies, especially for the low- ℓ orbits. The separation energy also depends upon the pairing and collective aspects of the residual interaction which are not present in the HF mean field. For the nuclei near the drip line one can constrain the orbit occupations and separation energies in the HF by the experimental data on binding energies and spectroscopic factors (supplemented by theoretical spectroscopic factors) discussed in the last section. The occupation constraint is imposed by calculating the HF density with fractional occupations. The separation energy constraint was made by multiplying the central HF potential so that the single-particle energy is equal to the one-neutron separation energy. This requires typically an adjustment of only a few percent in the potential strength.

For $Z \geq 8$, the neutron occupations are taken from the USD sd-shell wave functions. For $N = 16$ nuclei the $1s_{1/2}$ single-particle energy from the SKX HF calculation is close to the experimental separation energy [155]. No constraints were imposed for $N = 16$ or above. For $N = 15$ nuclei the $1s_{1/2}$ single-particle energies from the SKX HF calculation are about 1 MeV more deeply bound than the experimental separation energy and they were thus constrained to the experimental separation energies.

The calculated rms matter radii and interaction cross sections for $Z=2$ –11 are shown in Fig. (30) as a function of nucleon number A . The various isotopic chains are connected by lines (they are not labeled by Z but this can be inferred from the comparisons made with experiment in Fig. (29)).

In Fig. (30) one observes a correspondence between the rms matter radii and the interaction cross sections. There are several interesting trends. On the average the rms radii go as $A^{1/3}$ but there are significant deviations. The halo nuclei such ^{11}Li , ^{11}Be and ^{14}Be show a sharp increase. I would include in this set of halo nuclei ^{19}C and ^{22}C (whose interaction cross section has not yet been measured and is not included in the Fig. (29)). In addition, beyond $N = 14$ there is an upward bend which is due to shell effects in the HF potential which I will discuss below.

In Fig. (31) I show the proton, neutron and matter densities obtained with SKX for ^{22}C for which a $(0d_{5/2})^6(1s_{1/2})2$ configuration is assumed. (This is about 60% of wave function in the WBP and WBT $0\hbar\omega$ model space with the rest containing $0d_{3/2}$ components.) The $1s_{1/2}$ SPE is -1.74 with SKX. The HFB theory has recently been used to predict a “pairing anti-halo” effect in nuclei with $\ell=0$ valence states [255]. So this will be an interesting case to study experimentally. It is amusing that ^{22}C has just twice the number of protons and neutrons to the lower drip-line nucleus ^{11}Li , and it will be interesting to see if the pattern continues for other nuclei with $(N/Z) = (11/3)$, ^{33}F , ^{44}Mg , etc.

The interaction cross sections are compared with experiment in Fig. (29). In this figure $300(Z - 2)$ is added to experiment and theory in order to separate the various Z values in one figure. All of the calculated cross section are multiplied by 0.95 to obtain a optimum overall agreement with experiment. This 5% adjustment is probably within the range of that expected for the Glauber model approximation. The agreement with experiment is impressive. There are only two details which do not agree with experiment within error. One is the enhancement in the calculated ^{15}C ($N = 9$) cross section due to the relatively loose binding of the $1s_{1/2}$ orbit which does not show up in experiment. The other is the relatively large experimental cross section for ^{23}O ($N = 15$) which does not show up in the calculation. Other than this, the data supports the halo nature for some nuclei, as well as the upward bend after $N = 14$.

The theoretical kink at $N = 14$ is related to a change in the self-consistent HF potential. Up to $N = 14$ the $0d_{5/2}$ orbit is being filled and the neutron density increases at the nuclear surface. Beyond $N = 14$ neutron start to occupy the $1s_{1/2}$ orbit, part of its density lies in the nuclear interior on top of that already present from the filled $0s$ and $0p$ orbits. The HF matter densities and neutron potentials

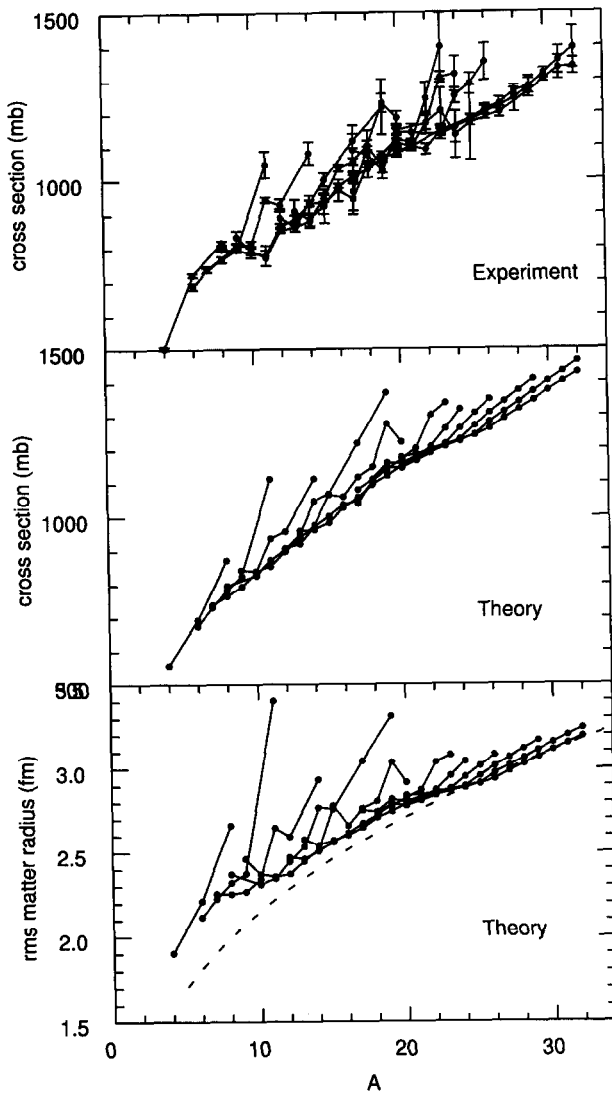


Figure 30: Top: experimental total interaction cross sections as a function of mass number; Middle theoretical cross sections; Bottom: theoretical rms matter radii. The dashed line represents a $A^{1/3}$ dependence.

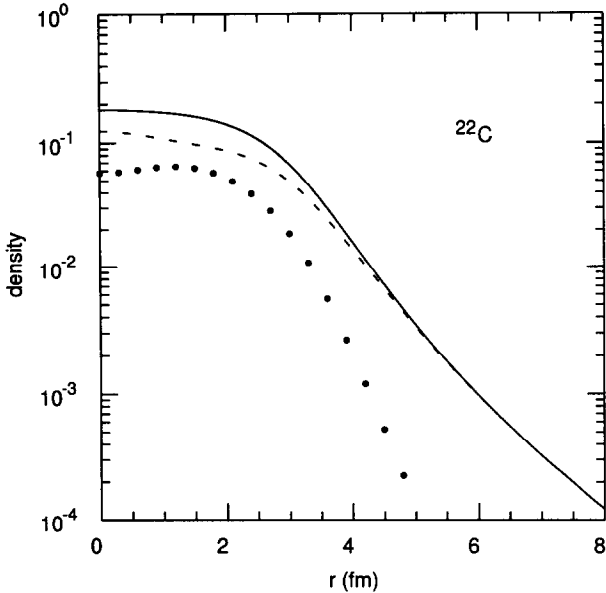


Figure 31: Proton (circles), neutron (dashed line) and total (solid line) SKX HF densities for ^{22}C . The density is in units of nucleons/fm 3 .

for the even-even oxygen isotopes from $N = 10$ to $N = 16$ are shown in Fig. (32). For $N = 10 - 14$ the surface density gradually increases as a function of neutron number and the resulting HF potential for neutrons is relatively constant as a function of neutron number. There is a discontinuous change in the potential when neutrons are added to the $1s_{1/2}$ orbit at $N = 16$ such that the neutron potential becomes suddenly weaker in the interior and hence pushes out the neutron density, especially for the $1s_{1/2}$ orbit itself.

The kink can be quantitatively defined by the ratio:

$$k = \frac{R_m(N = 16) - R_m(N = 14)}{R_m(N = 14) - R_m(N = 12)} \approx \frac{\sigma(N = 16) - \sigma(N = 14)}{\sigma(N = 14) - \sigma(N = 12)}, \quad (15)$$

where $R_m = \sqrt{\langle r_m^2 \rangle}$ is the rms matter radius and σ is the interaction cross section. The approximate equality between the value obtained from the rms matter radius and the interaction cross section follows numerically from the calculations. The numerical results for the oxygen isotopes ($Z = 8$) will be discussed. The SKX HF interaction gives $k = 2.0$. Other Skyrme interactions give k values between 1.9 and 2.1 as long as the single-particle energy of the $1s_{1/2}$ orbit is close to its experimental separation energy. The Woods-Saxon potential gives $k \approx 1.2$ which is a measure of the small skin or halo effect associated with the $1s$ orbit bound by about 3 MeV (the Woods-Saxon potential changes smoothly as a function of N). The NL3 relativistic Hartree model gives $k = 2.3$. So there is some mean-field model dependence in the k . For increasing Z , the sharp increase of the $1s_{1/2}$ occupancy at $N = 14$ is somewhat washed out due to the proton-neutron interaction in the sd-shell, and hence the k value slowly decreases with increasing Z . The experimental cross section data for nitrogen, oxygen and fluorine would favor a k value somewhat larger than the Skyrme value, but the data for $Z = 7 - 12$ as a whole agree well with the Skyrme value.

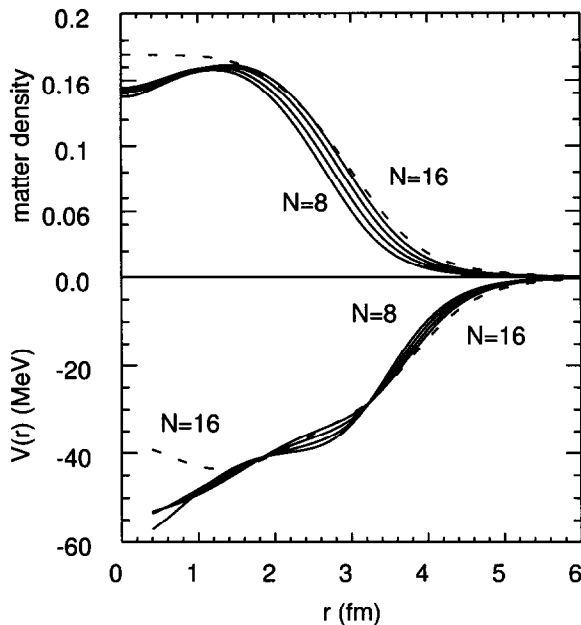


Figure 32: SKX HF matter densities and neutron potentials for $^{16,18,20,22,24}O$ corresponding to $N = 8, 10, 12, 14$ (sol. line) and $N = 16$ (dashed line).

5.7 E1 transitions

A consequence of the close spacing and halo nature of the $0s_{1/2}$ and $0p_{1/2}$ orbits found in $N = 7$ nuclei (discussed in Sec. 5.4.1) is that there is strong low-lying E1 strength in this region of nuclei. The outstanding early example is the $B(E1)$ for the $1/2^-$ to $1/2^+$ transition in ^{11}Be which has the largest E1 transition strength observed between low-lying bound states. Millener et al. [256] used the MK interaction together with Woods-Saxon radial wave functions to calculate this $B(E1)$ and obtained good agreement with experiment. In normal nuclei low-lying E1 transitions are weak due to the destructive interference between many single-particle components in the transition density – the coherent E1 strength where all of the single-particle matrix elements are in phase is in the high-energy giant dipole region. For the $1/2^-$ to $1/2^+$ transition in ^{11}Be the $1s_{1/2}$ - $0p_{1/2}$ contribution is much larger than usual because of the halo nature of these orbits, and hence this term dominates the other single-particle contributions producing a large $B(E1)$ [256].

Low-lying dipole strength has recently been discovered in ^{12}Be [241]. Sagawa et al. [257] have described this other E1 transitions in this mass region on the basis of the WBP and PSDMK2 interactions with HF radial wave functions.

5.8 Quadrupole moments and E2 transitions

A quadrupole deformation of the valence orbits (those in the model space) leads to a self-consistent deformation of the core orbits (the orbits in the closed shell). This is described in perturbation theory as the coupling of $2\hbar\omega J^\pi=2^+$ excitations of the core to the valence orbits [185], [34] and is represented within the model space as an effective charge for protons ($e_p = 1 + \delta_p$) and neutrons ($e_n = 0 + \delta_n$), where 1 and 0 are bare charges (all in units of e), and δ are the polarization charges. For the full LS model spaces (p, sd, pf) all of the low-lying collective states are treated explicitly, and the effective charge represents the coupling of the valence orbitals to the $\Delta N=2$ giant quadrupole resonance [34]. If one takes into account only the isoscalar giant resonance in nuclei with $N = Z$, then the protons and neutrons have the same same polarization charge $\delta_p=\delta_n$. The polarization charge is slightly orbital dependent with average calculated values of 0.4 to 0.5 for the sd-shell [34]. Coupling to the isovector giant quadrupole resonance in $N = Z$ nuclei increases the neutron effective charge and decreases the proton effective charge (the reason is that the average interaction between the valence neutron and core proton is larger than that between the valence proton and core proton). The calculated proton and neutron effective charges are $e_p = 1.3 - 1.4$ and $e_n = 0.5 - 0.6$, respectively for the upper sd shell [34]. The empirical effective charge averaged over orbits and mass in the sd-shell is $e_p = 1.29$ and $e_n = 0.49$, in reasonable agreement with the calculations.

These empirical values for the sd-shell are typical of those used in the shell-model configuration-mixing calculations for light nuclei. However, empirical effective charges (based upon a comparison of theory with a range of E2 data) may be influenced by truncations in the model space as well as other defects of the model wave functions (such as clustering and halo effects). In each case an attempt must be made to understand the origin and value of the effective charge.

As one goes away from nuclei with $N = Z$ toward the neutron drip line the neutron excess will influence the effective charge. Bohr and Mottelson [258] made a qualitative estimate: $e_p = 1 + (Z/A) - 0.32 - 0.02(N - Z)/A$ and $e_n = (Z/A) + 0.32 - 0.62(N - Z)/A$. Sagawa and Asahi [76] have carried out microscopic HF calculations for the carbon isotopes and obtained approximately $e_p = 1.29, 1.16$ and 1.03 for the $0p$ proton orbit in ^{12}C , ^{16}C and ^{20}C , respectively, $e_n = 0.50$ for the $0p$ neutron orbit in ^{12}C and $e_n = 0.33$ and 0.25 for the $0d$ orbit in ^{16}C and ^{20}C , respectively. The values for ^{12}C are typical of the $N = Z$ results discussed above. For neutron-rich nuclei the effective charges decrease. The decrease qualitatively follows from the Bohr-Mottelson estimate, but is also influenced by the single-particle binding of the valence orbits (a deep binding for protons and a loose binding for neutrons) [34].

In addition to the effective charge, one must consider realistic radial wave functions for the neutrons as they become more loosely bound. The increase of the E2 matrix elements due to the increase in size of loosely-bound valence neutrons partly cancels the decrease from the reduced effective charge. Recent calculations based on the HF radial wave functions and the WBT configuration mixing for the boron isotopes are in good agreement with experimental data for nuclei out to ^{17}B . I note, however, that the recent data for the ^{16}N 2^- Q moment is about a factor of two smaller than can be explained by current models [259].

Recent results for the Q moments of the neutron-rich sodium isotopes out to ^{29}Na are in reasonable agreement with the USD sd-shell model [260]. The Q moment of ^{31}Na [261] will be of particular interest in terms of its interpretation as a pf-shell intruder configuration.

I show the systematics of the 2^+ energies in Fig. (33) and $\text{B}(\text{E}2)$ values in Fig. (34). The data are taken from the compilation [262] with the addition of more recent results for ^{34}Mg [263], ^{58}Cr [153], ^{60}Cr [264], ^{64}Fe and ^{66}Fe [265]. The theoretical energies are based on $0\hbar\omega$ model spaces (which do not contain the intruder states) with hamiltonians WBT [73] for the p-sd shell, USD for the sd-shell [3], RCNP for the sd-pf shell ($N > 20$) [100], FPD6 [96], [266] for the pf shell with $N \leq 28$, and the truncated model-space results from [153] for the pf shell with $N > 28$. The $\text{B}(\text{E}2)$ values were obtained with the harmonic-oscillator radial wave functions and with effective charges of $e_p=1.29$ and $e_n=0.49$ [3] for the sd shell, $e_p=1.5$ and $e_n=0.5$ for the sd-pf shell [100], and $e_p=1.23$ and $e_n=0.54$ for the pf shell [53].

There is good overall agreement between theoretical and experimental energies with the exceptions of ^{12}Be ($N = 8$) and ^{32}Mg ($N = 20$) [267] which are related to their intruder structure. The high energy for the 2^+ state for $N = 32$ in ^{52}Ca is an indication of a sub-shell closure for $1\text{p}_{3/2}$ which quickly goes away as the proton-neutron interaction bring the $0\text{f}_{5/2}$ closer in energy to $1\text{p}_{3/2}$ as Z increases [153]. The sub-shell closure which appears at $Z = 40$ in the theory (since the pf shell ends at $Z = 40$) does not appear for iron ($Z = 26$) indicating the importance of $0\text{g}_{9/2}$ in this region. The RCNP hamiltonian [100], [133] predicts that the $N = 28$ shell closure in terms of 2^+ energy will remain for $Z \leq 20$ except for ^{40}Mg ($Z = 12$). New experiments will be of particular interest to test these predictions.

The $\text{B}(\text{E}2)$ values are not in such good agreement between theory and experiment. Neon and magnesium show an increase as they approach $N = 20$ rather than the theoretical decrease which is related to the gradual mixing with the intruder states. Utsuno et al. [39] are able to obtain the gradual mixing in the sd- $0\text{f}_{7/2}$ - $1\text{p}_{3/2}$ model space.

The $\text{B}(\text{E}2)$ values for ^{42}Ca ($N = 22$) and ^{44}Ca ($N = 24$) show a striking experimental enhancement over theory which is an indication of the mixing with intruder states in these nuclei near stability. This feature does not show up in the 2^+ energies. Indeed, it was noted in the early shell-model work that the pf-shell is not adequate for these nuclei [121], and that $2\hbar\omega$ sd-shell excitations are required [268], [269]. These $2\hbar\omega$ excitations are associated with low-lying intruder states in these nuclei. In spite of the advances which have been made in carrying out full sd-pf shell calculations for neutron-rich nuclei [39], [38], the expanded model space has not been applied to this region of nuclei near stability. These $2\hbar\omega$ excitations are probably also responsible for the deviations in the lighter titanium and argonne isotopes. There is another disagreement between experiment and theory for ^{46}Ar which was also noted in [270].

There are many other interesting E2 observable which I cannot cover adequately. The coexistence of shapes can be further explored by the studying the $\text{B}(\text{E}2)$ to higher 2^+ states in nuclei such as ^{34}Si [23], [136] and to states in odd-even nuclei, for example, ^{43}S [136].

The $\text{B}(\text{E}2)$ as measured by electromagnetic decay or Coulomb excitation provides information on the proton contribution to the E2 transitions. Complementary information on the neutron contribution can be obtained from inelastic hadronic scattering experiments [271], [272], [273]. It is important to understand how the proton and neutron degrees of freedom are coupled in nuclei near the drip line. Is it possible to have a deformed neutron halo and a spherical proton core or visa versa? In the valence shell

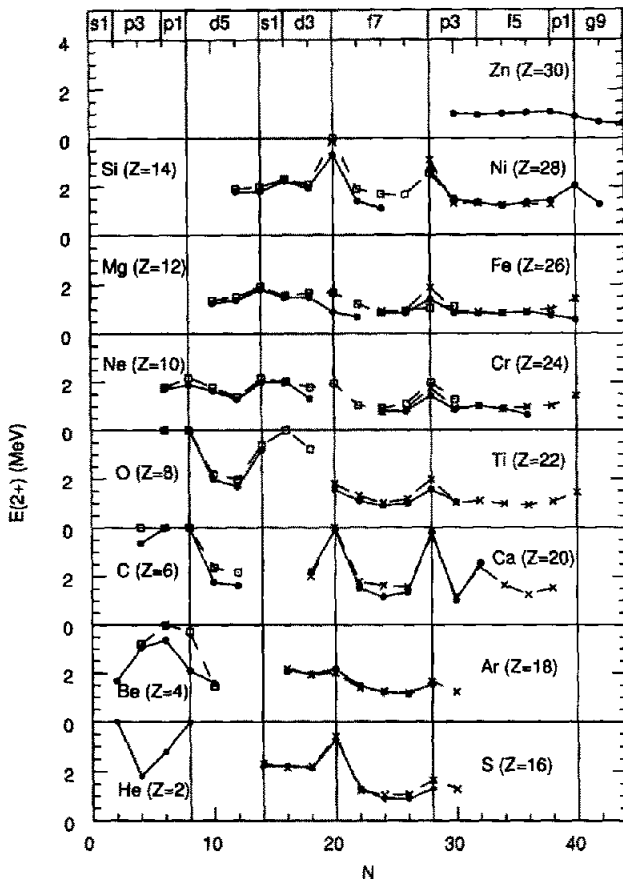


Figure 33: Energy of the lowest 2^+ states in MeV. The experimental energies shown by filled circles connected by solid lines. The theoretical energies are shown by squares connected by dashed lines for the nuclei on the left and by crosses connected by dashed lines for the nuclei on the right. 2^+ energies above 4 MeV are indicated at the top of the scale. The extreme single-particle ordering is given at the top.

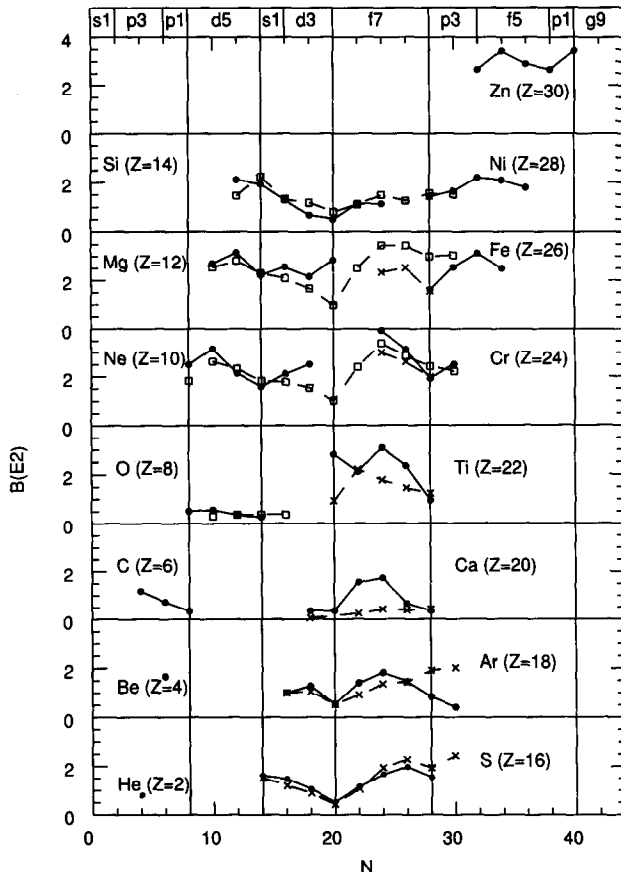


Figure 34: $B(E2)$ ($0^+ \rightarrow 2^+$) values for the excitation of the lowest 2^+ states. The $B(E2)$ in units of $e^2 \text{fm}^4$ are divided by $5Z^{4/3}$ so that they can be placed on a common scale. The theoretical energies are shown by squares connected by dashed lines for the nuclei on the left and by crosses connected by dashed lines for the nuclei on the right. The extreme single-particle ordering is given at the top.

model one must introduce generalized effective charges to account for the coupling of valence protons and neutrons to the core protons and neutrons [274]. Systematic experiments of the type started [275], [276], [277], [278] are needed to show how the neutron contribution evolves as one approaches the drip line.

5.9 Beta decay

The study of beta decay in nuclei is important for testing nuclear structure models, for the weak interaction rates needed in astrophysical processes, and for fundamental weak-interactions studies. The decay rate for allowed β^-/β^+ decay is given by:

$$ft_{1/2} = C/[(g_A/g_V)^2 B(GT_{-/+}) + B(F_{-/+})], \quad (16)$$

where f is the phase-space factor, $t_{1/2}$ is the partial half-life for the decay from an initial state (Ψ_i) to a specific final state (Ψ_f). To an accuracy of 1% C , is given by 6170. The dimensionless Gamow-Teller (GT) strength is:

$$B(GT_{-/+}) = |\langle \Psi_f | \Sigma_k \sigma^k t_{+-}^k | \Psi_i \rangle|^2 / (2J_i + 1), \quad (17)$$

and the dimensionless Fermi strength is:

$$B(F_{-/+}) = |\langle \Psi_f | \Sigma_k t_{+-}^k | \Psi_i \rangle|^2 / (2J_i + 1). \quad (18)$$

$|g_A/g_V| = 1.26$ is the ratio of the axial-vector to vector coupling constants for the nucleon as obtained from the neutron beta decay, and t_+ and t_- , are the nucleon isospin raising and lowering operators, respectively. The B values satisfy the sum rules

$$S(F) = \Sigma_f B(F_-) - \Sigma_f B(F_+) = (N - Z), \quad (19)$$

and

$$S(GT) = \Sigma_f B(GT_-) - \Sigma_f B(GT_+) = 3(N - Z). \quad (20)$$

In this section I will give some examples of the application of the nuclear shell model to the beta decay of exotic nuclei.

5.9.1 Fermi decay

When isospin is conserved the Fermi decay populates only the isobaric analog state in the daughter nucleus. When $|T_{zi}| = T_i$ then either $B(F_-)$ or $B(F_+)$ is zero and the B value for the other is $|N - Z|$. There is a small isospin nonconserving part to the nucleon-nucleon interaction due to the Coulomb and charge-dependent nuclear interactions, and this leads to a small correction to the Fermi matrix element which is conventionally expressed in the form $\tilde{B}(F) = (1 - d)B(F)$. The results of a recent calculation [279] for the correction factors d are shown in Fig. (35) (crosses connected by a line) and compared to the experimental values (filled circles) for those $0^+ \rightarrow 0^+$ (pure Fermi) decays which have been measured with high accuracy [280], [281]. The correction factor is the sum of two parts, $d = d_{IM} + d_{RO}$, one due to isospin mixing (IM) within the valence space for shell-model configuration mixing, and the other due to a mismatch in the radial wave functions leading to a radial overlap (RO) correction. (For these $B(F)$ values the constants and phase space factors associated with Eq. (16) need to be evaluated to an accuracy of 0.1%.) The experimental values have been adjusted by an overall factor to fit the calculations for the lowest Z values.

On an absolute scale, the experiment and theory deviate (from the unitarity of the KM matrix) by 0.3–0.4 percent [282], [283], [284], [280]. The reason for this deviation is not understood, but if no other

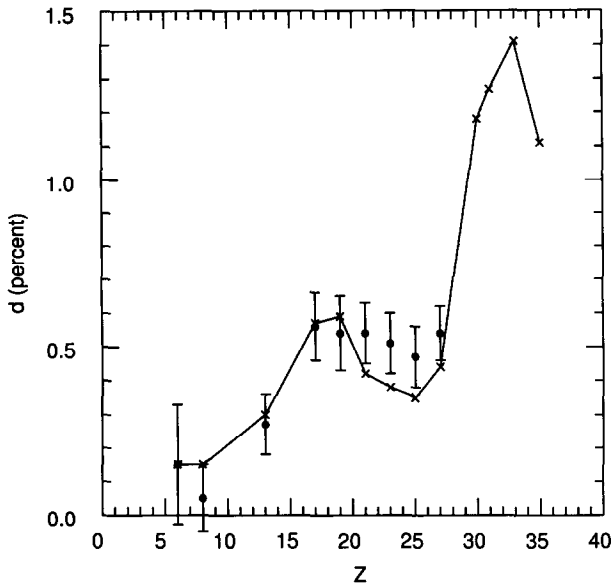


Figure 35: Isospin mixing corrections to the Fermi transitions. The crosses connected by a line are theoretical calculations. The filled circles are relative values deduced from experimental Fermi beta decay.

nuclear structure problems are found, it is a sign of new physics beyond the standard model of weak interactions. The new aspect of the calculations presented in Fig. (35) is the prediction of a jump in the d value at $Z=30$ and above. The jump is due primarily to an increase in the RO correction for high Z values. The IM corrections leads to isospin-forbidden transitions to excited 0^+ states [279] which will be explored in new experiments.

5.9.2 Gamow-Teller beta decay

One of the most comprehensive comparisons of experimental and theoretical GT strength has been carried out for the sd shell nuclei [285] with the USD interaction. In [285] the comparison between theory and experiment was made for several hundred individual transitions. It was found that the experimental strength is systematically quenched relative to the theoretical strength by a factor of about 0.59; that is, the experimental beta decay rate is hindered by a factor of 1.67 compared to theory. Where is the missing strength? Maybe some of the strength has been missed in the beta decay because the strength is shifted to higher energy states above the Q value window. The (p,n) experiments provide important complimentary information in this regard. For example, the strength for the ^{18}Ne beta decay can be compared with the strength observed in the mirror $^{18}\text{O}(\text{p},\text{n})$ reaction [286], [287]. Examination of the spectrum of Fig. 7 of [286] shows that the GT strength distribution (into the sharp states) is much like the predicted one. Detailed analysis of such spectra [287] show that the observed GT strength distribution agrees with that predicted by the 0d1s shell-model calculations and that the missing strength is not to be found in sharp states below 20 MeV of excitation. This quenching factor of about 0.6 appears to be rather universal as long as a complete $0\hbar\omega$ model space (e.g. full sd) is used. Calculations within the full pf shell require about the same reduction factor in order to reproduce the observed GT beta decay [125], [288]. Much theoretical work has been done to understand the origin of

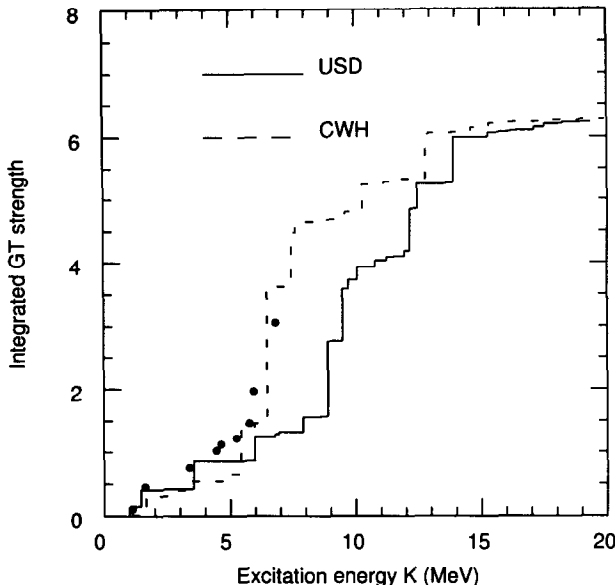


Figure 36: $B(GT)$ values for the $^{36}\text{Ca} \rightarrow {}^{36}\text{K}$ beta decay, summed as a function of excitation energy. The circles are experiment [293] and the calculations are for the USD (line) and CWH (dashes) interactions.

the quenching [289], [290]. From comparison of M1 and GT matrix elements, one can deduce that about two-thirds (in the amplitude) of this comes from higher-order configuration mixing (from non-sd shell parts of the wave function) while one-third comes from the delta-particle nucleon-hole admixture [291]. The position of the missing strength and its division between β^- and β^+ related to the higher-order mixing is unclear but is presumably spread out over excitation energies up to about 100 MeV, making it difficult to observe experimentally.

The lifetimes obtained for the beta decay of proton and neutron-rich nuclei in the sd shell are generally in excellent agreement with the USD calculations based upon the quenched effective operator. An exception to this occurred for nuclei around ${}^{31}\text{Na}$ where the experimental lifetimes for some nuclei are about an order of magnitude longer than those predicted by theory [292]. This was another early indication of the intruder nature of these states which have been discussed extensively in this review.

Studies of the GT strength function give a more detailed critique of theory. I show as an example in Fig. (36) the GT strength obtained from the beta decay of ${}^{36}\text{Ca}$. The $B(GT)$ values are obtained for individual states and then summed as a function of excitation energy. The experimental strength includes an analysis of the beta delayed proton spectra [294], [293]. The theoretical $B(GT)$ values include the empirical quenching factor of 0.60. The free-nucleon sum-rule strength is 12 units and the quenching brings this down to 7.2 units. The comparison in Fig. (36) shows features which are typical of the decay of proton- and neutron-rich nuclei. The phase-space associated with the beta decay Q value of about 11 MeV means that the experiment is only sensitive to strength up to about 8 MeV in excitation, this part comprising only about 1/3 of the total predicted strength. The half-life is determined mainly by the very small $B(GT)$ values in the lowest 2 MeV. In comparison with the USD curve in Fig. (36) one would conclude that experimental GT strength is too large compared to theory and that one does not need quenching [295]. However, an analysis of the ${}^{38}\text{Ca}$ data reveals [296] that the theoretical GT strength has indeed to be quenched. The shape of experimental distribution is in better agreement

Table 5: Calculated and measured beta-decay properties of proton-rich sd shell nuclei with $|T_z| \geq 2$

Parent Nucleus	$ T_z $	J^π	$T_{1/2}$ (ms)		Ex of IAS (MeV)		BR to IAS(%) ^b	Beta Delayed Decay Modes	Exp Ref
			Theory ^a	Exp	Theory	Exp			
^{20}Mg	2	0^+	102	95 ± 3	6.46	6.57	3.5	p	[301]
^{22}Al	2	4^+	88	59 ± 3	14.02	14.04	3.8	p,2p, α	[302]
^{24}Si	2	0^+	147	140 ± 8	5.87	5.91	11.1	p	[303], [304]
^{26}P	2	3^+	38	44.7 ± 0.5	13.37	13.08	2.8	p,2p, α	[305]
^{28}S	2	0^+	129	125 ± 10	5.96	5.95	14.5	p	[306]
^{32}Ar	2	0^+	87	98 ± 2	5.00	5.04	21.0	p	[307]
^{36}Ca	2	0^+	104	100 ± 2	4.24	4.26	40.7	p	[294]
^{23}Si	5/2	$5/2^+$	38	40.7 ± 0.4	11.59	11.78	4.9	p,2p,3p, α	[308]
^{27}S	5/2	$5/2^+$	9	15.5 ± 1.3	12.62	12.75	3.5	p,2p,3p, α	[309], [310]
^{31}Ar	5/2	$5/2^+$	12	15.1 ± 1.3	12.06	12.30	4.1	p,2p,3p, α	[311], [312]
^{35}Ca	5/2	$1/2^+$	23	25.7 ± 0.2	8.82	9.05	12.1	p,2p,3p	[298]
^{22}Si	3	0^+	28	29 ± 2	8.95		3.8	p,2p,3p	[313]

a) There is an uncertainty of about 10% due the uncertainty in the beta-decay Q value.

b) These are the theoretical values. Most experimental values quoted in the literature are inferred from the Ex(IAS) and $T_{1/2}$ or have a very large error.

with that obtained with the older CWH interaction [297] as shown for the ^{36}Ca decay in Fig. (36). The difference in shape between the USD and CWH GT distributions can be related to the $0d_{3/2}, 0d_{5/2}$ spin-orbit splitting in the upper sd shell [297]. Similar considerations are necessary in the interpretation of the more recent ^{35}Ca decay data [298]. The influence of the energy shift for the β^+ decay of the proton-rich calcium isotopes has been also been observed in the ^{34}Ar beta decay [299].

The GT strength functions in the pf shell are important for understanding beta-decay and electron capture during the late stages of stellar evolution. The data and calculations with the KB3 and KBF interactions are discussed in [124], [300].

Beta decay data have been obtained for most sd-shell nuclei out to the proton drip line. A summary of the calculated [314] and experimental half-lives are given in Table 5. Other calculations based on the USD interaction are given in [315]. The agreement for the half-lives is excellent. The half-life calculations include the universal GT quenching factor, and the agreement with experiment indicates that the basic quenching mechanism (from higher-order configuration mixing) is valid out to the proton drip line. The beta delayed particle emission can be quite complex, but it can be calculated within the shell model [314]. The beta delayed α emission predicted in [314] has been observed experimentally [302].

The quenching of GT strength is well established in for nuclei near the valley of stability and for proton-rich nuclei. But the operator may be closer to its free nucleon form for halo components of the beta transition in nuclei such as ^{11}Li [316] due to a reduction in the interaction overlap between the valence and core nucleons. There has been some (i.e. [317], [136]) but not extensive theoretical work on the beta decay of the most neutron-rich nuclei which involve the p-sd and sd-pf shells. First-forbidden beta decay will be more important for neutron-rich nuclei due to the increased phase space for these transitions – these involve significantly more complicated transition operators [318], [128].

5.9.3 Super Gamow-Teller transitions

By “Super” Gamow-Teller transition I mean a GT transition to a specific final state which has a large $B(GT)$ value compared to the bare nucleon (neutron decay) value of $B(GT)=3$. Although the sum-rule value can be quite large in nuclei with a large neutron excess, it is not easy to find many examples of Super GT transitions due to the splitting of GT strength. For example, for the GT_- transition from ^{208}Pb , which has been studied with the intermediate energy (p,n) reaction, the GT_+ should be small (because of the neutron excess) and hence $\Sigma_f B(GT_-) \approx 132$. However, for ^{208}Pb as well as most other cases observed, the total GT strength is fragmented over many final states, hence the GT strength to any specific final state is small.

In fact, there are only two transitions to specific final states observed so far which are larger than the neutron value of 3. They are $0^+, T = 1$, ^6He to $1^+, T = 0$, ^6Li decay with $B(GT_-)=4.72$ [319] and the $0^+, T = 1$, ^{18}Ne to $1^+, T = 0$, ^{18}F decay with $B(GT_+)=3.15$ [285]. The reduction from the sum-rule values of $S(GT) = 6$ are due to the quenching discussed above. In both of these examples, the final states are ground states and they come low in energy because of the attractive particle-particle interaction. As one moves away from the two-particle valence case and adds more valence particles, the strong GT strength moves up in energy and eventually becomes a “particle-hole” state which is pushed up by the residual particle-hole interaction. The high energy usually results in a fragmentation of strength due to mixing with 2p-2h configurations. Borge et al. [320] have presented the case for Super GT strength in the decays of ^8He , ^9Li and ^{11}Li . However, since the final states lie at a high excitation energy, the strength is probably fragmented over many final states. Op shell calculations for the ^9Li decays show this fragmentation [321]. Op shell calculations [319] for the ^8He decay predict a strength of 7.7 for a state at about 9 MeV in excitation [319] but the experiment is difficult to interpret because of the large width of the final state.

There are two remaining candidates for Super GT transitions – ^{56}Ni and ^{100}Sn . ^{56}Ni is known to decay to a low-lying final state in ^{56}Co , but the Q value is very small, and this particular final state has a very small $B(GT)$. We have predicted [322] a Super GT to a level just above the Q value with $B(GT) \approx 5.5$ which may be studied via the inverse reaction $p(^{56}\text{Ni}, ^{56}\text{Co})n$. ^{100}Sn has been predicted to decay by a Super GT to a should beta decay by a Super GT to a low-lying state in ^{100}In with $B(GT) \approx 8.5$ [323]. The main condition for the existence of these isolated Super GT transitions in ^{56}Ni and ^{100}Sn is that the spin-orbit gap between the $\ell + \frac{1}{2}$ and $\ell - \frac{1}{2}$ orbits be sufficiently small compared to the shell gap so that the 1p-1h states are isolated below the 2p-2h states.

The GT strength of ^{56}Ni and ^{100}Sn are both examples of a general class of transitions in nuclei with $N=Z$ [324]. The $N=Z$ nuclei are interesting because the GT sum rule only gives $\Sigma_f B(GT_-) = \Sigma_f B(GT_+)$, a result of isospin symmetry. The $\Sigma_f B(GT)$ are thus completely model dependent and are sensitive to nuclear correlations [324]. There are several equivalent ways to obtain the $B(GT)$ values in $N=Z$ nuclei; β^+ decay (where energetically allowed) or (n,p) reactions, β^- decay or (p,n) reactions, or (p,p') reactions. As one approaches ^{100}Sn , the beta decay Q values become larger due to the larger Coulomb displacement energy [325], hence much more of the GT strength can be observed in beta decay. Data for the interesting region between ^{56}Ni and ^{100}Sn will rely upon future radioactive beam experiments. GT strength in this mass region is important for beta decay and electron capture which takes place in the late stages of stellar evolution [124], [300], [326].

5.10 Magnetic moments

The precisely measured magnetic moments historically have served as a sensitive test of the shell-model wave functions. In this perspective I show on the left-hand side of Fig. (37) the experimental magnetic moments for nuclei near stability considered in [3] (those that are measured to 1% or better accuracy) compared to those obtained with the simplest possible (single Slater determinant) sd-shell

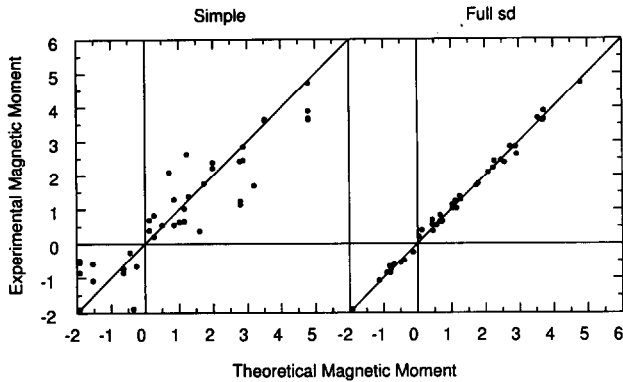


Figure 37: Comparison of experimental and theoretical magnetic moments in the sd shell. The theory on the right-hand side is based on the full sd-shell wave functions obtained with the USD interaction. The theory on the left-hand side assumes only the simplest single-particle wave function (a single Slater determinant). Both calculations use the free nucleon M1 operator.

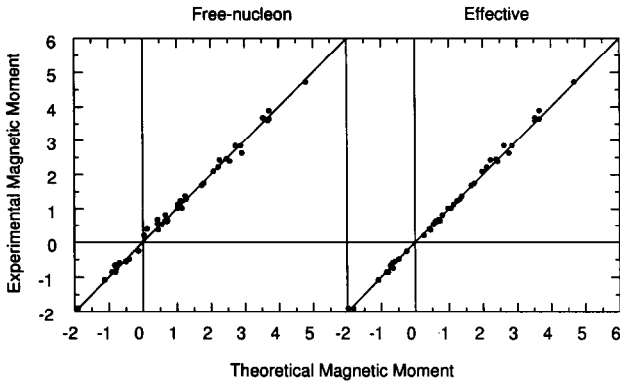


Figure 38: Comparison of experimental and theoretical magnetic moments in the sd shell. The theory is based on the full sd-shell wave functions obtained with the USD interaction. The results on the right-hand side are obtained with the free-nucleon M1 operator, and the results on the left-hand side are obtained with the effective M1 operator.

Table 6: Magnetic moments of $3/2^-$ states in the p-shell. Experiment (from [20] except for ^7Be [331] and ^9C [332]) is compared to those obtained with the results from three p-shell hamiltonians. Free-nucleon and effective g-factors [112] are used.

Nucleus	T	experiment	(6-16)TBME free	PJT free	PMOM free	PMOM effective
$\mu ^7\text{Be}$	1/2	-1.398	-1.288	-1.329	-1.377	-1.368
$\mu ^9\text{Be}$	1/2	-1.178	-1.268	-1.101	-1.090	-1.070
$\mu ^{11}\text{C}$	1/2	-0.964	-0.783	-0.850	-0.949	-0.924
$\mu ^9\text{C}$	3/2	(-)1.391	-1.482	-1.438	-1.511	-1.503
$\mu ^{13}\text{O}$	3/2	-1.389	-1.270	-1.355	-1.411	-1.388
$\mu ^7\text{Li}$	1/2	3.256	3.171	3.212	3.263	3.273
$\mu ^9\text{B}$	1/2		3.082	2.893	2.877	2.895
$\mu ^{11}\text{B}$	1/2	2.689	3.509	2.592	2.702	2.724
$\mu ^9\text{Li}$	3/2	3.439	3.376	3.352	3.425	3.430
$\mu ^{13}\text{B}$	3/2	3.177	3.022	3.125	3.191	3.209
$\mu ^{11}\text{Li}$	5/2	3.668	3.793	3.793	3.793	3.801
$\langle \sigma \rangle A = 7$	1/2	0.94	1.01	1.01	1.02	1.07
$\langle \sigma \rangle A = 9$	1/2		0.82	0.77	0.76	0.85
$\langle \sigma \rangle A = 11$	1/2	0.59	0.59	0.64	0.67	0.79
$\langle \sigma \rangle A = 9$	3/2	1.44	1.04	1.09	1.09	1.12
$\langle \sigma \rangle A = 13$	3/2	0.76	0.66	0.71	0.74	0.84

wave functions. The dramatic improvement obtained by using the full sd-shell with the USD hamiltonian is shown on the right-hand side. As mentioned previously, this improvement is related to using the LS model space which fully incorporates both members of the spin-orbit doublet $j = \ell \pm \frac{1}{2}$ which are strongly connected by the M1 (magnetic moment) operator. The mechanisms which quench the Gamow-Teller beta decay also apply to the spin part of the M1 operator. However because of its vector rather than axial vector nature, meson exchange corrections are more important for the M1 operator [289], [290]. There are enhancements from the mesonic exchange which tend to cancel the higher-order quenching (observed in Gamow-Teller) making the free-nucleon results shown in Fig. (37) already close to experiment. The agreement with experiment can be improved, as shown in Fig. (38) by the use of an effective M1 operator which is given in terms of effective spin and orbital g factors [3]. The effective operator is compared to calculations which include mesonic exchange and higher-order configuration mixing in [291]. More recently, magnetic moments have been measured in the sd shell for more exotic nuclei [327], [260], [328], [329], [330]. The deviation between experiment and theory is at the level of $\pm 0.05 \mu_N$ (e.g. 1% of the largest value).

A similar level of agreement between experiment and theory is obtained for magnetic moments in the p-shell [94], as shown in Table 6 for $3/2^-$ states. The magnetic moment for the $A = 9$, $T = 3/2$ mirror pair has been of recent interest [332], [333]. If good isospin is assumed, one can add the moments of mirror nuclei to deduce an isoscalar spin matrix element [334] $\langle \sigma \rangle = [\mu(\text{proton rich}) + \mu(\text{neutron rich}) - J]/(0.38)$. For $A = 9$ one obtains $\langle \sigma \rangle = [\mu(^9\text{C}) + \mu(^9\text{Li}) - 3/2]/(0.38) = 1.44$. This is compared with the results for other $3/2^-$ mirror pairs in Table 6. (The single-particle values are $\mu_p = -1.913$, $\mu_n = 3.793$ and $\langle \sigma \rangle = 1$.) The hamiltonians chosen are the (6-16)TBME of Cohen and Kurath, a more recent version of the ETBME fit called PJT [94], and one which also considered magnetic moments in the ETBME fit called PMOM [112]. Free-nucleon g-factors [$g_s(\text{proton})=5.586$, $g_s(\text{neutron})=-3.826$, $g_\ell(\text{proton})=1$ and $g_\ell(\text{neutron})=0$] and effective g-factors [$g_s(\text{proton})=5.543$, $g_s(\text{neutron})=-3.875$, $g_\ell(\text{proton})=1.030$ and $g_\ell(\text{neutron})=0.036$] obtained from the PMOM fit are used. There are considerable variations in the $\langle \sigma \rangle$ values which are reproduced by theory, with both experiment and theory

being largest for $A = 9$. The effects of higher-order configuration mixing [290], [289], [291] is to reduce (quench) the $\langle \sigma \rangle$ values. However, the $A = 9$ experimental $\langle \sigma \rangle$ value is anomalously large compared to theory. The isospin mixing effects discussed in [333] increase $\langle \sigma \rangle$ by about $0.10 \mu_N$. It is interesting that the ^7Be and ^9C moments are more nearly equal to each other experimentally than expected theoretically. A simple interpretation could be that the structure of ^9C looks like ^7Be plus two protons in the $1s_{1/2}$ orbit (which would not contribute to the moment). But this interpretation would require some evidence in the mirror nucleus ^9Li for a low-lying configuration of this type which does not now exist. The magnetic moment for ^{11}Li in Table 6 shows a deviation from the other p-shell nuclei which can be interpreted in terms of component in the ^{11}Li wave function which looks like ^9Li plus two neutrons in the $1s_{1/2}$ orbit.

Recently measured magnetic moments for ^{14}B , ^{15}B , ^{17}B and ^{17}N have been compared with the MK and WBP calculations [335], [336]. The recent experimental result [337] of $\mu = -1.6816(8) \mu_N$ for ^{11}Be $1/2^+$ is of particular interest for its intruder structure. It is also the first result for any $1/2^+$ moment in this mass region. With the free-nucleon operator its value is close to that of $-1.71 \mu_N$ obtained with the MK interaction and somewhat larger than that of -1.58 (-1.49) μ_N obtained with WBT (WBP) [337]. However, a quantitative interpretation of the experimental result will depend upon an understanding of the effective M1 operator for this loosely bound system. A precise experimental value for the ^{15}C $1/2^+$ moment is needed.

6 The Model-Space for Heavier Nuclei

This review has focussed on the properties of medium-light nuclei where one finds a gradual transition from the LS to jj model space. In this section I comment on some problems involving the model space in heavier nuclei. For the nuclei around $N = 40$, it is clear that the sdg major oscillator shell becomes important and in particular the $0g_{9/2}$ orbital. There is only a very small shell effect at the pf-shell neutron closure in ^{68}Ni which certainly disappears for higher Z and may also disappear for lower Z . It will be important in future experiments to see if there is some pf-shell effect left in ^{60}Ca .

The model space for nuclei between about $A = 60$ and $A = 100$ should involve at least the $0f_{5/2}$, $1p_{3/2}$, $1p_{1/2}$ and $0g_{9/2}$ orbitals. But configuration mixing within this set of orbitals may not be adequate for understanding the structure of nuclei in this region, due to the influence of the low-lying states associated with the quadrupole and Gamow-Teller operators.

The quadrupole degrees of freedom involve three regions of energy: (a) low energy transitions within the $(0f_{5/2}, 1p_{3/2}, 1p_{1/2}, 0g_{9/2})$ model space; (b) $0g_{9/2}$ to $0g_{7/2}$ and $0g_{9/2}$ to $1d_{5/2}$ excitations outside the model space whose energy lies around 3 MeV in ^{100}Sn ; and (c) the high-energy $\Delta N=2$ ($2\hbar\omega$) excitations (also outside the model space). Since (b) is low in energy, its influence might not be treated perturbatively, especially if the valence space configuration is strongly deformed. It will be interesting to see to what extent the $(0f_{5/2}, 1p_{3/2}, 1p_{1/2}, 0g_{9/2})$ model space will work, but a more complete valence space for this mass region may need to involve all of the pf and sdg orbitals. Similar questions arise for the completeness of jj major shells in heavier nuclei which are the basis for counting the number of valence bosons in the interacting-boson model [338], as well as other models which rely on a well-defined number of valence nucleons [339].

For the $0f_{5/2}$, $1p_{3/2}$, $1p_{1/2}$, $0g_{9/2}$ model space, there is an important first-order correction to the GT and M1 operators involving the $0g_{9/2}$ to $0g_{7/2}$ transition. This cannot be treated as a constant effective operator since its contribution depends upon the occupation of the $0g_{9/2}$ and $0g_{7/2}$ orbitals. This occupation number dependence is an important ingredient in understanding the N and Z dependence of the Gamow-Teller strength observed in the ^{100}Sn region [340], [341] relative to a model in which ^{100}Sn has a closed-shell configuration. Also, there is a higher absolute quenching of the GT matrix elements when ^{100}Sn is treated as a closed shell due to first-order $0g_{9/2}$ to $0g_{7/2}$ correction terms,

in addition to the usual higher-order quenching (as in the sd and pf shells). It may be possible to formulate a mass-dependent model for the effective GT and M1 operators. Or one may have to consider a more complete or full pf-sdg model space. An understanding of these quenching effects is crucial for reliable predictions of beta-decay matrix elements needed for astrophysics and weak-interaction physics (such as double-beta decay). Future experiments on the detailed beta decay properties of ^{100}Sn will be of primary importance in understanding these issues [323].

7 Summary and Outlook

Overall agreement between the theoretical and experimental properties presented in this review is excellent. The agreement with experiment does not significantly deteriorate at the drip lines. On the contrary, there are places of disagreement both for nuclei near stability and for exotic nuclei which are related to model-space truncation. For example, in the calcium isotopes near stability the enhanced B(E2) (compared to the pf shell model) indicates the importance sd-shell admixtures. These same type of admixtures are necessary for the intruder states in the neutron-rich nucleus ^{32}Mg . With the improved computational techniques the model spaces can be enlarged to sd-pf, and this has been successfully applied to some nuclei in the ^{32}Mg mass region. What is lacking is a consistent application of the sd-pf model space (or s-p-sd-pf-sdg) to all nuclei going from stability to the neutron drip line. This will be a gradual process of expansion. For example, determination of a “universal” pf-shell hamiltonian which is underway [82] together with the QMCD (or a similar) method will provide a unified set of results for the pf shell region of nuclei. It will be much more challenging to obtain unified interactions for the p-sd and sd-pf models spaces which will provide the extension of the $0\hbar\omega$ results in Figs. 17–23 and 33–34 to the mixed $\hbar\omega$ wave functions which explicitly contain the low-lying and ground-state intruder configurations.

The G matrix approach to the nuclear interactions relies upon the use of the harmonic-oscillator basis [62]. These serve as a starting point for the shell-model configuration mixing for all nuclei even out to the drip line. In nuclei near the valley of stability the shell model is successfully applied up to excitation energies above the nucleon decay thresholds; at the neutron drip line the neutron decay threshold goes to zero. Above the decay threshold, continuum rather than oscillator basis should be considered. The empirical modifications of the TBME might be partly attributed to the loose binding and the continuum for high lying states in nuclei near the valley of stability and for the low-lying states in nuclei near the drip neutron drip line. More fundamentally, one must extend the G matrix approach to understand the interaction between nucleons at high excitation and near the drip lines.

The goal in nuclear theory must be to expand and unify our current approaches so that the properties of all nuclei can be better understood and so that the predictive power becomes more accurate. To achieve this goal it is necessary to integrate the two main types of models: the mean field and the shell-model configuration mixing. The Skyrme HF in the spherical basis provides a starting point for the closed-shell binding energies and single-particle energies. The role of configuration mixing is then to give the extra correlations associated with core breaking. It will be important to treat nuclei such as ^{16}O and ^{40}Ca as open shell nuclei.

The properties of magic nuclei are of primary importance for starting shell-model configuration mixing. Recent results on single-particle energies around ^{132}Sn have greatly improved the configuration-mixing predictions for nuclei towards the neutron-drip line in this region. Similar results from radioactive-beam experiments for the single-particle properties of other nuclei such as ^{60}Ca and ^{78}Ni will provide launching pads for shell-model configuration mixing in these mass regions.

Acknowledgments

I thank Stefan Typel for providing the NL3 mean-field results, Michio Honma for providing some pf

shell results for FPD6, and Alfredo Poves and Frederik Nowacki for the RCNP separation energies. There were helpful communications with Fred Barker, Gregers Hansen, John Millener, Werner Richter, Ernst Roeckl and Brad Sherrill. Support for this work was provided from US National Science Foundation grant number PHY-0070911.

Table 7: Appendix: List of acronyms and abbreviations used in the text.

Term	Meaning	Section	Reference
	model spaces		
p-shell	0p _{3/2} and 0p _{1/2}	2.1	
sd-shell	0d _{5/2} , 0d _{3/2} and 1s _{1/2}	2.1	
pf-shell	0f _{7/2} , 0f _{5/2} , 1p _{3/2} and 1p _{1/2}	2.1	
LS shells	the major shells p, sd and pf	2.1	
0 $\hbar\omega$	lowest possible excitation between LS shells	3	
N $\hbar\omega$	N $\hbar\omega$ excitations between LS shells	3	
mixed $\hbar\omega$	N $\hbar\omega$ with several or all N mixed	3	
	interactions		
(8-16)POT	p-shell POT hamiltonian	4.6	[25]
(6-16)TBME	p-shell ETBME hamiltonian	4.6	[25]
(8-16)TBME	p-shell ETBME hamiltonian	4.6	[25]
CWP,CWH	sd-shell ETBME+G hamiltonians	4.7	[84], [116]
FPD6	pf-shell POT hamiltonian	4.8	[96]
FPMG	pf-shell G+MON hamiltonian	4.8	[95]
GXPF	pf-shell ETBME+G hamiltonian	4.8	[82]
H7B	“Hosaka sum of seven-range OBEP” potential	4.4	[88]
KB3	pf-shell G+MON hamiltonian	4.8	[36]
KB3G	pf-shell G+MON hamiltonian	4.8	[37]
M3Y	“Michigan sum of three-range Yukawa” potential	4.4	[86], [87]
MK	0 $\hbar\omega$ s-p-sd-pf-shell hamiltonian	4.9	[97]
MSk7	Skyrme-type hamiltonian	4.5	[10]
NL3	Dirac-Hartree hamiltonian	4.5	[93]
PJT	p-shell ETBME hamiltonian	4.6	[94]
PJP	p-shell POT hamiltonian	4.6	[94]
PWBT	p-shell ETBME hamiltonian	4.6	[73]
RCNP	0 $\hbar\omega$ sd-pf-shell hamiltonian	4.10	[100]
SDPOTA	sd-shell POT hamiltonian	4.7	[90]
SKX	Skyrme-type hamiltonian	4.5	[11]
USD	sd-shell ETBME+G hamiltonian	4.7	[24]
WBP	0 $\hbar\omega$ s-p-sd-pf-shell hamiltonian	4.9	[73]
WBT	0 $\hbar\omega$ s-p-sd-pf-shell hamiltonian	4.9	[73]
WBMB	0 $\hbar\omega$ sd-pf-shell hamiltonian	4.10	[98], [99]
	other		
BCS	Bardeen-Cooper-Schrieffer pairing approximation	4.5	
CSB	charge-symmetry breaking	5.3.1	
ETBME	effective TBME	4.4	
ETBME+G	ETBME with some replacement by the G matrix	4.4	
G+MON	the G matrix with monopole corrections	4.4	
HF	Hartree-Fock	4.5	
MSDI	modified-surface delta function interaction	4.4	[85]
MSOBEP	modified-surface one-boson exchange potential	4.4	[90]
OBEP	one-boson exchange potential	4.4	
POT	potential model fit	4.4	
QMCD	quantum Monte Carlo diagonalization	3	[52]
SPE	single-particle energy(ies)	2.2	
SMMC	shell-model Monte Carlo	3	[50], [51]
TBME	two-body matrix element(s)	3	

Table 8: The PJT and PJP p-shell hamiltonians for $A = 16$ from [94]. $0p_{1/2}$ is orbit 1 and $0p_{3/2}$ is orbit 2. These interactions have a mass dependence given by $TBME^A = TBME^{A=16}(A/16)^{-0.17}$.

	orbits	J T	PJT	PJP
SPE	1		4.3522	4.7345
	2		2.1422	1.9751
TBME	1 1 1 1	1 0	-3.5383	-4.1112
	1 1 1 1	0 1	-0.6188	0.2335
	1 1 2 1	1 0	2.0001	1.1399
	1 1 2 2	1 0	2.6524	2.1417
	1 1 2 2	0 1	-4.1265	-4.7316
	2 1 2 1	1 0	-6.0149	-6.4461
	2 1 2 1	2 0	-5.0237	-4.6554
	2 1 2 1	1 1	0.7552	0.6215
	2 1 2 1	2 1	-1.6697	-1.8895
	2 1 2 2	1 0	4.0113	3.6183
	2 1 2 2	2 1	-1.6633	-1.5997
	2 2 2 2	1 0	-3.3558	-3.2280
	2 2 2 2	3 0	-5.8166	-5.8791
	2 2 2 2	0 1	-3.2533	-3.1122
	2 2 2 2	2 1	-0.9119	-0.7584

References:

1. M. G. Mayer, Phys. Rev. **75** (1949).
2. O. Haxel, J. H. D. Jensen and H. E. Suess, Phys. Rev. **75**, 1766 (1949).
3. B. A. Brown and B. H. Wildenthal, Ann. Rev. of Nucl. Part. Sci. **38**, 29 (1988).
4. P. Navratil, J. P. Vary and B. R. Barrett, Phys. Rev. Lett. **84**, 5728 (2000), and references therin.
5. W. C. Haxton and C. L. Song, Phys. Rev. Lett. **84**, 5484 (2000).
6. B. S. Pudliner, V. R. Pandharipande, J. Carlson, S. C. Pieper, and R. B. Wiringa, Phys. Rev. C **56**, 1720 (1997).
7. R. B. Wiringa, S. J. Piper, J. Carlson and V. R. Pandharipande, Phys. Rev. C **62**, 014001 (2000).
8. W. E. Ormand, Phys. Rev. C **53**, 214 (1996); Phys. Rev. C **55**, 2407 (1997).
9. B. A. Brown, R. Clement, H. Schatz, W. A. Richter, A. Volya and W. A. Richter, unpublished.
10. S. Goriely, F. Tondeur and J. M. Pearson, At. Data Nucl. Data Sheets **77**, 311 (2001).
11. B. A. Brown, Phys. Rev. C **58**, 220 (1998).
12. Conference Proceeding for Nuclei in the Cosmos 2000, Nucl. Phys. **A688**, 1 (2001).
13. J. Dobaczewski and W. Nazarewitz, Phil. Trans. R. Proc. Lond. **A356**, 2007 (1998).
14. P. G. Hansen, A. S. Jensen and B. Jonson, Ann. Rev. Nucl. Part. Sci. **45**, 505 (1995).
15. I. Tanihata, Prog. Part. Nucl. Phys. **35**, 505 (1995).
16. V. I. Goldansky, Nucl. Phys. **19**, 482 (1960).
17. B. A. Brown, Phys. Rev. C **43**, R1513 (1991); C **44**, 924 (1991).
18. B. Blank et al., Phys. Rev. Lett. **84**, 1116 (2000).
19. P. M. Endt, Nucl. Phys. **A521**, 1 (1990); Nucl. Phys. **A633**, 1 (1998).
20. R. B. Firestone, V. S. Shirley, C. M. Baglin, S. Y. Frank Chu and J. Zipkin, *Table of Isotopes*, (Wiley Interscience Publication, 1996).
21. P. G. Thirolf et al., Phys. Lett. B **485**, 16 (2000).
22. <http://www.nscl.edu/~brown/sde.htm>
23. R. W. Ibbotson et al., Phys. Rev. Lett. **80**, 2081 (1998).
24. B. H. Wildenthal, Prog. Part. Nucl. Phys. **11**, 5 (1984).
25. S. Cohen and D. Kurath, Nucl. Phys. **73**, 1 (1965), Nucl. Phys. **A101**, 1 (1967).
26. E. K. Warburton, B. A. Brown and D. J. Millener, Phys. Lett. B **293**, 7 (1992).
27. T. Otsuka, M. Honma and T. Mizusaki, Phys. Rev. Lett. **81**, 1588 (1998).
28. W. Kutschera, B. A. Brown and K. Ogawa, La Rivista del Nuovo Cimento **11**, 1 (1978).
29. J. B. French, E. C. Halbert, J. B. McGrory and S. S. M. Wong, Adv. Nucl. Phys. **3**, 193 (1969).
30. J. P. Elliott and T. H. R. Skyrme, Proc. R. Soc. London Ser A **232**, 561 (1955).
31. S. Gartenhaus and C. Schwartz, Phys. Rev. **108**, 482 (1957).
32. P. Navratil and B. R. Barrett, Phys. Rev. C **54**, 2986 (1996).
33. B. A. Brown, A. Etchegoyen, W. D. M. Rae, N. S. Godwin, W. A. Richter, C. H. Zimmerman, W. E. Ormand and J. S. Winfield, MSU-NSCL Report No. 524, 1985.
34. H. Sagawa and B. A. Brown, Nucl. Phys. **A430**, 84 (1984).
35. H. Sagawa and B. A. Brown, Phys. Lett. **150B**, 247 (1985).
36. A. Poves and A. P. Zuker, Phys. Rep. **70**, 235 (1981).
37. A. Poves, J. Sanchez-Solano, E. Caurier and F. Nowacki, Phys. Rev. C, to be published.
38. D. J. Dean, M. T. Ressell, M. Hjorth-Jensen, S. E. Koonin, and A. P. Zuker, Phys. Rev. C **59**, 2474 (1999).

39. Y. Utsuno, T. Otsuka, T. Mizusaki and M. Honma, Phys. Rev. C **60**, 054315 (1999).
40. R. R. Whitehead, A. Watt, B. J. Cole and I. Morrison, Adv. Nucl. Phys. **9**, 123 (1977).
41. E. Caurier et al., shell-model code ANTOINE, CRN, Strasbourg, 1989; C. A. Ur et al., Phys. Rev. C **58**, 3163 (1998).
42. A. Schmidt et al., Phys. Rev. C **62**, 044319 (2000).
43. T. Mizusaki, RIKEN Accel. Prof. Rep. **33**, 15 (2000).
44. D. Zwarts, Comp. Phys. Comm. **38**, 365 (1985).
45. E. Caurier et al., shell-model code NATHAN, unpublished.
46. B. A. Brown, Phys. Rev. Lett. **85**, 5300 (2000).
47. S. Cohen and D. Kurath, Nucl. Phys. **A101**, 1 (1967).
48. T. Sebe and J. Nachamkin, Ann. of Phys. **51**, 100 (1969).
49. R. R. Whitehead, Nucl. Phys. **A182**, 290 (1972).
50. S. E. Koonin, D. J. Dean and K. Langanke, Phys. Rep. **577**, 1 (1996).
51. S. E. Koonin, D. J. Dean and K. Langanke, Annu. Rev. Nucl. Part. Sci. **47**, 463 (1997).
52. T. Otsuka, M. Honma, T. Mizusaki, N. Shimizu and Y. Utsuno, Rep. Prog. Phys., to be published.
53. T. Mizusaki, T. Otsuka, Y. Utsoni, M. Honma and T. Sebe, Phys. Rev. C **59**, R1846 (1999).
54. M. Horoi, A. Volya and V. Zelevinsky, Phys. Rev. C **50**, 2064 (1999).
55. T. Mizusaki, T. Otsuka, M. Honma and B. A. Brown, Phys. Rev. C **63**, 044306 (2001).
56. J. Dobaczewski et al., Nucl. Phys. **A422**, 103 (1984).
57. P. H. Heenen, P. Bonche, J. Dobaczewski and H. Flocard, Nucl. Phys. **A561**, 367 (1993).
58. P. Bonche, J. Dobaczewski, H. Flocard and P. H. Heenen, Nucl. Phys. **A530**, 149 (1991).
59. A. Petrovici, K. W. Schmid and A. Faesler, Nucl. Phys. **A665**, 333 (2000).
60. K. W. Schmid, F. Grümmer and A. Faesler, Ann. Phys. **180**, 1 (1987).
61. B. A. Brown, C. Bronk and P. E. Hodgson, Jour. Phys. G10, 1683 (1984).
62. M. Hjorth-Jensen, T. T. S. Kuo and E. Osnes, Phys. Rep. **261**, 125 (1995).
63. A. G. M. van Hees, J. G. L. Booten and P. W. M. Glaudemans, Phys. Rev. Lett. **62**, 2245 (1989).
64. T. Hoshino, H. Sagawa and A. Arima, Nucl. Phys. **A481**, 458 (1988).
65. T. Hoshino, H. Sagawa and A. Arima, Nucl. Phys. **A506**, 271 (1990).
66. T. Otsuka, N. Fukunishi and H. Sagawa, Phys. Rev. Lett. **70**, 1385 (1993).
67. J. M. G. Gomez, C. Prieto and A. Poves, Phys. Lett. B **295**, 1 (1992).
68. B. A. Brown, RIKEN Review **26**, 53 (2000).
69. B. A. Brown and W. A. Richter, Phys. Rev. C **58**, 2099 (1998).
70. W. E. Ormand and B. A. Brown, Nucl. Phys. **A491**, 1 (1989).
71. W. E. Ormand and B. A. Brown, Nucl. Phys. **A440**, 274 (1985).
72. W. E. Ormand and B. A. Brown, Phys. Lett. B **174**, 128 (1986).
73. E. K. Warburton and B. A. Brown, Phys. Rev. C **46**, 923 (1992).
74. L. Jaqua, M. A. Hasan, J. P. Vary and B. R. Barrett, Phys. Rev. C **46**, 2333 (1992).
75. P. G. Hansen and B. M. Sherrill, “Reactions and Single-Particle Structure of Nuclei Near the Drip Lines”, Nucl. Phys. A (to be published).
76. H. Sagawa and K. Asahi, Phys. Rev. C **63**, 064310 (2001).
77. D. J. Millener, Nucl. Phys. A, to be published (2001).
78. K. Bennaceur, F. Nowacki, J. Okołowicz and M. Płoszajcew, Nucl. Phys. **A671**, 203 (2000).
79. M. Sakakura, A. Arima and T. Sebe, Phys. Lett. **61B**, 335 (1976).
80. E. Ormand, private communication (2001).

81. A. de Shalit and I. Talmi, *Nuclear Shell Theory*, (Academic Press, 1963).
82. M. Honma, B. A. Brown, T. Mizusaki and T. Otsuka, Nucl. Phys. A, to be published.
83. A. Arima, S. Cohen, R. D. Lawson and M. H. MacFarlane, Nucl. Phys. **A108**, 94 (1968).
84. W. Chung, Pd. D. thesis, Michigan State University (1976).
85. P. J. Brussaard and P. W. M. Glaudemans, *Shell Model Applications in Nuclear Spectroscopy*, (North Holland, 1977).
86. G. Bertsch, J. Borysowicz, H. McManus and W. G. Love, Nucl. Phys. **A284**, 399 (1977).
87. N. Anantaraman, H. Toki and G. F. Bertsch, Nucl. Phys. **A398**, 269 (1983).
88. Hosaka A., Kubo K. I. and Toki H., Nucl. Phys. **A444**, 76 (1985)
89. M. Hjorth-Jensen, private communication.
90. B. A. Brown, W. A. Richter, R. E. Julies and B. H. Wildenthal, Ann. Phys. **182**, 191 (1988).
91. A. G. M. van Hees and P. W. M. Glaudemans, Z. Phys. **A315**, 223 (1984).
92. I. Talmi, Helv. Phys. Acta **25**, 185 (1952).
93. G. A. Lalazissis, J. König and P. Ring, Phys. Rev. C **55**, 540 (1997).
94. R. E. Julies, W. A. Richter and B. A. Brown, South African Jour. Phys. **15**, 35 (1992).
95. J. B. McGrory, Phys. Rev. C **8**, 693 (1973).
96. W. A. Richter, M. G. Van der Merwe, R. E. Julies and B. A. Brown, Nucl. Phys. **A523**, 325 (1991).
97. D. J. Millener and D. Kurath, Nucl. Phys. **A255**, 315 (1975).
98. E. K. Warburton, J. A. Becker, D. J. Millener and B. A. Brown, BNL report 40890 (1987).
99. E. K. Warburton, J. A. Becker, and B. A. Brown, Phys. Rev. C **41**, 1147 (1990).
100. J. Retamosa, E. Caurier, F. Nowacki and A. Poves, Phys. Rev. C **55**, 1266 (1997).
101. T. R. H. Skyrme, Philos. Mag. **1**, 1043 (1956); Nucl. Phys. **9**, 615 (1959); **9**, 635 (1959).
102. D. Vautherin and D. M. Brink, Phys. Rev. C **5**, 626 (1972).
103. W. Kohn and L. J. Sham, Phys. Rev. **140** A1133 (1965).
104. R. M. Dreizler and E. K. U. Gross, “Density Functional Theory: An Approach to the Quantum Many-Body Problem”, (Springer, Berlin, 1990).
105. F. Tondeur, S. Goriely, J. M. Pearson, and M. Onsi, Phys. Rev. C **62**, 024308 (2000).
106. M. M. Sharma, G. Lalazissis, J. Konig and P. Ring, Phys. Rev. Lett. **74**, 3744 (1995).
107. B. Friedman and V. R. Pandharipande, Nucl. Phys. **A361**, 502 (1981).
108. B. A. Brown, Phys. Rev. Lett. **85**, 5296 (2000).
109. S. Typel and B. A. Brown, Phys. Rev. C **64**, 027302 (2001).
110. B. A. Brown, W. A. Richter and R. Lindsay, Phys. Lett. B **483**, 49 (2000).
111. J. D. Walecka, Ann. Phys. (N. Y.) **83**, 491 (1974).
112. A. G. M. van Hees, A. A. Wolters and P. W. M. Glaudemans, Nucl. Phys. **A476**, 61 (1988).
113. T.T.S. Kuo and G.E. Brown, Nucl. Phys. **85**, 40 (1966)
114. T.T.S. Kuo, Nucl. Phys. **A103**, 71 (1967).
115. B.H. Wildenthal, E.C. Halbert, J.B. McGrory and T.T.S. Kuo, Phys. Rev. C **4**, 1266 (1971).
116. B.H. Wildenthal in *Elementary Modes of Excitation in Nuclei*, Proceedings of the International School of Physics Enrico Fermi, course 69, edited by A. Bohr and R.A. Broglia (North-Holland, 1977), p. 383; B.H. Wildenthal and W. Chung in *Mesons in Nuclei*, edited by M. Rho and D.H. Wilkinson, (North-Holland, 1979), p. 723.
117. M. W. Kirson, Phys. Lett. **47B**, 110 (1973).
118. K. Klingenbeck, W. Knupfer, M. G. Huber and P. W. M. Glaudemans, Phys. Rev. C **15**, 1483 (1977).

119. K. Yoshinada, Phys. Rev. C **26**, 1784 (1982), and references therin.
120. T. T. S. Kuo and G. E. Brown, Nucl. Phys. **A114**, 235 (1968).
121. J. B. McGrory, B. H. Wildenthal and E. C. Halbert, Phys. Rev. C **2**, 186 (1970).
122. D. Rudolf et al., Phys. Rev. Lett. **82**, 3763 (1999).
123. P. von Neumann-Cosel, A. Poves, J. Retamosa and A. Richter, Phys. Lett. B **443**, 1 (1998).
124. E. Caurier, K. Langanke, G. Martinez-Pinedo and F. Nowacki, Nucl. Phys. **A653**, 439 (1999).
125. W. A. Richter, M. G. Van der Merwe, R. E. Julies and B. A. Brown, Nucl. Phys. **A577**, 585 (1994).
126. J. W. Olness, E. K. Warburton, D. E. Alburger, C. J. Lister, and D. J. Millener, Nucl. Phys. **A373**, 13 (1982).
127. T. Suzuki and T. Otsuka, Phys. Rev. C **56**, 847 (1997).
128. E. K. Warburton, I. S. Towner and B. A. Brown, Phys. Rev. C **49**, 824 (1994).
129. E. K. Warburton, D. E. Alburger, J. A. Becker, B. A. Brown and S. Raman, Phys. Rev. C **34**, 1031 (1986).
130. E. K. Warburton, Phys. Rev. C **35**, 2278 (1987); G. Wang, E. K. Warburton and D. E. Alburger, Phys. Rev. C **35**, 2272 (1987).
131. E. K. Warburton and J. A. Becker, Phys. Rev. C **39**, 1535 (1989); Phys. Rev. C **40**, 2823 (1989).
132. T. Siiskonen, P. O. Lipas and J. Rikovska, Phys. Rev. C **60**, 034312 (1999).
133. E. Caurier, F. Nowacki, A. Poves and J. Retamosa, Phys. Rev. C **58**, 2033 (1998).
134. S. Kahana, H. C. Lee and C. K. Scott, Phys. Rev. **180**, 956 (1969).
135. J. Duflo and A. P. Zuker, Phys. Rev. C **59**, R2347 (1999).
136. S. Nummela et al., Phys. Rev. C **63**, 044316 (2001).
137. A. Watt, R. P. Singhal, M. H. Storm and R. R. Whitehead, J. Phys. G **7**, L145 (1981).
138. A. Poves and J. Retamosa, Phys. Lett. B **184** 311 (1987).
139. A. Poves and J. Retamosa, Nucl. Phys. **A571**, 221 (1994).
140. N. Fukunishi, T. Otsuka and T. Sebe, Phys. Lett. B **296**, 279 (1992).
141. T. Otsuka and N. Fukunishi, Phys. Rep. **264**, 297 (1996).
142. M. Fauerbach, et al., Phys. Rev. C **53**, 647 (1996).
143. D. Guillemaud-Mueller et al., Phys. Rev. C **41**, 937 (1990).
144. P. G. Reinhard, D. J. Dean, W. Nazarewicz, J. Dobaczewski, J. A. Maruhn and M. R. Strayer, Phys. Rev. C **60**, 014316 (1999).
145. D. Goeckner and L. Zamick, Phys. Rev. C **14**, 1662 (1976).
146. S. O. Backman, G. E. Brown and J. A. Niskanen, Phys. Rep. **124**, 1 (1985).
147. C. Mahaux, P. F. Bortignon, R. A. Broglia and C. G. Dasso, Phys. Rep. **120**, 1 (1985).
148. I. Hamamoto, H. Sagawa and X. Z. Zhang, Phys. Rev. C **64**, 024313 (2001).
149. Y. Utsuno, T. Otsuka, T. Mizusaki and M. Honma, Phys. Rev. C **64**, 011301 (2001).
150. F. Pougheon et al., Europhys. Lett. **2**, 505 (1986).
151. H. Sakurai et al., Phys. Lett. B **448**, 180 (1999).
152. T. Otsuka, R. Fujimoto, Y. Utsuno, B. A. Brown, M. Honma and T. Mizusaki, Phys. Rev. Lett. (2001) to be published.
153. J. I. Prisciandaro et al., Phys. Lett. B **510**, 17 (2001).
154. S. Pittel, Phys. Lett. B **82**, 303 (1985).
155. G. Audi and A. H. Wapstra, Nucl. Phys. **A595**, 409 (1995).
156. F. Sarazin et al., Phys. Rev. Lett. **84**, 5062 (2000).
157. D. Lunney et al., Phys. Rev. C, to be published.

158. A. Volya, B. A. Brown and V. Zelevinsky, Phys. Lett. B. **509**, 37 (2001).
159. G. Martinez-Pinedo, A. P. Zuker, A. Poves and E. Caurier, Phys. Rev. C **55**, 187 (1997).
160. M. Wiescher, J. Gorres and F. K. Thielemann, Astrophys. J. **326**, 384 (1988).
161. A. Garcia et al., Phys. Rev. C **43**, 2012 (1991).
162. R. Sherr and H. T. Fortune, Phys. Rev. C **58**, 3292 (1998).
163. D. W. Bardayan et al., Phys. Rev. Lett. **83**, 45 (1999).
164. J. A. Nolen and J.P. Schiffer, Ann. Rev. Nucl. Sci. **19**, 471 (1969).
165. C. Titin-Schnaider and P. Quentin, Phys. Lett. **49B**, 397 (1974).
166. T. Suzuki, H. Sagawa and A. Arima, Nucl. Phys. **A536**, 141 (1992)
167. B. J. Cole, Phys. Rev. C **54**, 1240 (1996).
168. Phys. Rev. C **58**, 2831 (1998).
169. W. E. Ormand, Phys. Rev. C **55**, 2407 (1997).
170. A. Bulgac and V. R. Shaginyan, Nucl. Phys. **A601**, 103 (1996).
171. A. Bulgac and V. R. Shaginyan, Phys. Lett. B **469**, 1 (1999).
172. A. Bulgac and V. R. Shaginyan, Eur. Phys. J. A **5**, 247 (1999).
173. R. Sherr and G. Bertsch, Phys. Rev. C **32**, 1809 (1985).
174. B. A. Brown, A. Csoto and R. Sherr, Nucl. Phys. **A597**, 66 (1996).
175. G. A. Miller, B. M. K. Nefkens and I. Slaus, Phys. Rep. **194**, 1 (1990).
176. G. Q. Li and R. Machleidt, Phys. Rev. C **58**, 3153 (1998).
177. R. B. Wiringa, V. G. J. Stoks and R. Schiavilla, Phys. Rev. C **49**, 2950 (1995).
178. C. Harzer, H. Muther and R. Machleidt, Phys. Lett. B **459**, 1 (1999).
179. K. Tsushima, K. Saito and A. W. Thomas, Phys. Lett. B **465**, 36 (1999).
180. C. J. Horowitz and J. Piekarewicz, Phys. Rev. C **63**, 01330(R), (2000).
181. B. A. Brown and P. G. Hansen, Phys. Lett. B **391** (1996).
182. H. Schatz et al., Phys. Rep. **294**, 167 (1998).
183. H. T. Fortune, R. Sherr and B. A. Brown, Phys. Rev. C **61**, 057303 (2000).
184. H. Herndl, J. Goerres, M. Wiescher, B. A. Brown and L. Van Wormer, Phys. Rev. C **52**, 1078 (1995).
185. B. A. Brown, A. Arima and J. B. McGrory, Nucl. Phys. **A277**, 77 (1977).
186. H. Nakada and T. Otsuka, Phys. Rev. C **49**, 886 (1994).
187. H. Kitagawa and H. Sagawa, Phys. Lett. B **299**, 1 (1993).
188. B. Davids et al., Phys. Rev. Lett. **86**, 2750 (2001), and references therin.
189. A. Navin et al., Phys. Rev. Lett. **81**, 5089 (1998).
190. O. V. Bochkarev et al., Nucl. Phys. **A505**, 215 (1989).
191. R. A. Kryger et al., Phys. Rev. Lett. **74**, 860 (1995).
192. F. C. Barker, Phys. Rev. C **59**, 535 (1999).
193. M. J. Chromik et al., Phys. Rev. C **55**, 1676 (1997).
194. J. Gomez del Campo et al., Phys. Rev. Lett. **86**, 43 (2001).
195. L. V. Grigorenko, R. C. Johnson, I. G. Mukha, I. J. Thompson and M. V. Zhukov, Phys. Rev. Lett. **85**, 22 (2000).
196. J. Giovannazzo et al., Eur. Jour. Phys. A **10**, 73 (2001).
197. F. C. Barker, Phys. Rev. C **63**, 047303 (2001).
198. W. Nazarewicz et al., Phys. Rev. C **53**, 740 (1993).
199. B. A. Brown and D. J. Millener, unpublished (2001).

200. M. Ichimura et al., Nucl. Phys. **A208**, 225 (1973).
201. N. Anyas-Weiss et al., Phys. Rep. **12C**, 201 (1974).
202. C. De Coster, B. Decroix and K. Heyde, Phys. Rev. C **61**, 067306 (2000).
203. K. Heyde et al., Physics Reports 102, 291 (1983).
204. K. Heyde et al., Phys. Rev. C **38**, 984 (1984).
205. K. Heyde et al., Nucl. Phys. **A484**, 275 (1988)
206. P.-H. Heenen, J. Dobaczewski, W. Nazarewicz, P. Bonche and T. L. Khoo, Phys. Rev. **57**, 1719 (1998).
207. I. Talmi and I. Unna, Phys. Rev. Lett. **4**, 469 (1960).
208. H. Sagawa, B. A. Brown and H. Esbensen, Phys. Lett. B **309**, 1 (1993).
209. M. Thoennessen et al., Phys. Rev. C **59**, 111 (1999).
210. M. Chartier et al., Phys. Lett. B **510**, 24 (2001).
211. L. Chen et al., Phys. Lett. B **505**, 21 (2001).
212. V. Guimaraes et al., Phys. Rev. C **61**, 064609 (2000).
213. A. Navin et al., Phys. Rev. Lett. **85**, 266 (2000).
214. W. C. Haxton and C. Johnson, Phys. Rev. Lett. **65**, 1325 (1990).
215. C. Thibault et al., Phys. Rev. C **12**, 644 (1975).
216. B. H. Wildenthal and W. Chung, Phys. Rev. C **19**, 164 (1979).
217. X. Campi et al., Nucl. Phys. **A251**, 193 (1975).
218. M. H. Storm, A. Watt and R. R. Whitehead, J. Phys. **G9**, L165 (1983).
219. A. Arima, H. Horiuchi and T. Sebe, Phys. Lett. **24B**, 129 (1967).
220. P. J. Ellis and T. Engeland, Nucl. Phys. **A144**, 161 (1970).
221. P. J. Ellis and T. Engeland, Nucl. Phys. **A181**, 368 (1972).
222. L. Zamick, Phys. Lett. **19**, 580 (1965).
223. R. D. Lawson, *Theory of the Nuclear Shell Model*, (Clarendon Press, Oxford, 1980).
224. G. E. Arenas Peris and P. Federman, Phys. Lett. B **173**, 359 (1986).
225. B. V. Pritychenko et al., Phys. Rev. C **62**, 05160 (2000).
226. B. V. Pritychenko et al., Phys. Lett. B **461**, 322 (1999).
227. B. V. Pritychenko et al., Phys. Rev. C **63**, 011305 (2001).
228. J. M. Bang, F. G. Gareev, W. T. Pinkston and J. S. Vaagen, Phys. Rep. **125**, 253 (1985).
229. “Spectroscopic Factors for Single Nucleon Transfer for $A = 21\text{--}44$ ”, P. M. Endt, Atomic and Nuclear Data Tables **19**, 23 (1977).
230. J. S. Winfield et al., Nucl. Phys. **A683**, 48 (2001).
231. P. G. Hansen, Phys. Rev. Lett. **77**, 1016 (1996).
232. V. Maddalena et al., Phys. Rev. C **63**, 024613 (2001).
233. T. Aumann et al., Phys. Rev. Lett. **84**, 35 (2000).
234. J. A. Tostevin, J. Phys. G **25**, 735 (1999).
235. D. Bazin et al., Phys. Rev. C **57**, 2156 (1998).
236. J. A. Tostevin, et al., to be published.
237. E. Sauvan et al., Phys. Lett. B **491**, 1 (2000).
238. F. C. Barker, J. Phys. **G2**, L45 (1976).
239. D. E. Alburger et al., Phys. Rev. C **17**, 1525 (1978).
240. H. T. Fortune, G. B. Liu and D. E. Alburger, Phys. Rev. C **50**, 1355 (1994).
241. H. Iwasaki et al., Phys. Lett. B **491**, 8 (2000).

242. H. Simon et al., Phys. Rev. Lett. **83**, 496 (1999).
243. S. Karataglides, P. G. Hansen, B. A. Brown, K. Amos and P. J. Dortmans, Phys. Rev. Lett. **79**, 1447 (1997).
244. M. Thoennessen, S. Yokoyama and P. G. Hansen, Phys. Rec. C **63**, 014308 (2001).
245. M. Labiche et al., Phys. Rev. Lett. **86**, 600 (2001).
246. W. N. Catford, L. K. Fifield, N. A. Orr and C. L. Woods, Nucl. Phys. **A503**, 263 (1989).
247. A. T. Reed et al., Phys. Rev. C **60**, 024311 (1999).
248. H. Herndl, R. Hofinger, J. Jank, H. Oberhummer, J. Goerres, M. Wiescher, F. K. Thielemann and B. A. Brown, Phys. Rev. C **60**, 064614 (1999).
249. I. Tanihata et al., Phys. Rev. Lett. **55**, 2676 (1985).
250. A. Ozawa et al., to be published (2001).
251. A. Ozawa, T. Suzuki and I. Tanihata, RIKEN preprint (2001).
252. G. F. Bertsch, B. A. Brown and H. Sagawa, Phys. Rev. C **39**, 1154 (1989).
253. B. A. Brown and W. A. Richter, Phys. Rev. C **54**, 673 (1996).
254. S. K. Charagi and S. K. Gupta, Phys. Rev. C **41**, 1610 (1990).
255. K. Bennaceur, J. Dobaczewski and M. Ploszajczak, Phys. Lett. B **496**, 154 (2000).
256. D. J. Millener, D. E. Alburger, E. K. Warburton and D. H. Wilkinson, Phys. Rev. C **26**, 1167 (1982).
257. H. Sagawa, T. Suzuki, H. Iwasaki and M. Ishihara, Phys. Rev. C **63**, 034310 (2001).
258. A. Bohr and B. R. Mottelson, *Nuclear Structure Volume II*, (W. A. Benjamin, Inc., 1975).
259. K. Matsuta et al., Phys. Rev. Lett. **86**, 3735 (2001).
260. M. Keim, U. Georg, A. Klein, R. Neugart, M. Neuroth, S. Wilbert, P. Lievens, L. Vermeeren and B. A. Brown, Eur. Phys. J. **A8**, 31 (2000).
261. S. Wilbert, et al., International Nuclear Physics Conference, August 24-28, 1998, Paris, France, p. 397.
262. S. Raman, C. W. Nestor, and P. Tikkanen, Atomic Data Nucl. Data Tables, to be published (2001).
263. K. Yoneda et al., Phys. Lett. B **499**, 223 (2001).
264. O. Sorlin et al., Nucl. Phys. **A669**, 351 (2000).
265. M. Hannawald et al., Phys. Rev. Lett. **82**, 1391 (1999).
266. M. Honma, private communication.
267. T. Motobayashi et al., Phys. Lett. B **346**, 9 (1995)
268. P. Federman and S. Pittel, Phys. Rev. **186**, 1106 (1969).
269. B. H. Flowers and L. D. Skouras, Nucl. Phys. **A136**, 353 (1969).
270. H. Scheit et al., Phys. Rev. Lett. **77**, 3967 (1996).
271. A. M. Bernstein, V. R. Brown and V. A. Madsen, Phys. Lett. **103B**, 255 (1981).
272. N. Alamanos, A. Pakou, A. Lagoyannis and A. Musumarra, Nucl. Phys. **A660**, 406 (1999).
273. A. M. Bernstein, V. R. Brown and V. A. Madsen, Comments Nucl. Part. Phys. **11**, 203 (1983).
274. B. A. Brown and B. H. Wildenthal, Phys. Rev. C **21**, 2107 (1980).
275. H. Scheit et al., Phys. Rec. C **63**, 014604 (2001).
276. F. Marechal et al., Phys. Rev. C **60**, 034615 (1999).
277. J. K. Jewell et al., Phys. Lett. B **454**, 181 (1999).
278. L. A. Riley et al., Phys. Rev. Lett. **82**, 4196 (1999).
279. W. E. Ormand and B. A. Brown, Phys. Rev. C **52**, 2455 (1995).
280. G. Savard et al., Phys. Rev. Lett. **42**, 1521 (1995).

281. The 1995 Chalk River compilation, I. S. Towner, private communication.
282. W. E. Ormand and B. A. Brown, Phys. Rev. Lett. **62**, 866 (1989); Phys. Rev. Lett. **63**, 103 (1989).
283. F. C. Barker, B. A. Brown, W. Jaus and G. Rasche, Nucl. Phys. **A540**, 501 (1992).
284. I. S. Towner, Nucl. Phys. **A540**, 478 (1992).
285. B. A. Brown and B. H. Wildenthal, Atomic Data Nucl. Data Tables **33**, 347 (1985). The $B(GT)$ as defined in the present work is related to the $M(GT)$ of this references by $B(GT) = [M(GT)/1.251]^2/(2J_i + 1)$.
286. J. Rapaport and E. Sugarkar, Annu. Rev. Nucl. Part. Sci. **44**, 109 (1994).
287. B. D. Anderson et al., Phys. Rev. C **27**, 1387 (1983).
288. E. Caurier, G. Martinez-Pinedo, F. Nowacki, A. Poves, J. Retamosa and A. P. Zuker, Phys. Rev. C **59**, 2033 (1999).
289. I. S. Towner, Phys. Rep. **155**, 264 (1987).
290. A. Arima, K. Schimizu, W. Bentz and H. Hyuga, Adv. Nucl. Phys. **18**, 1 (1987).
291. B. A. Brown and B. H. Wildenthal, Nucl. Phys. **A474**, 290 (1987).
292. B. H. Wildenthal, M. S. Curtin and B. A. Brown, Phys. Rev. C **28**, 1343 (1983).
293. M. J. Lopez-Jimenez et al., Eur. Phys. J. A **10**, 119 (2001).
294. W. Trinder, et al., Phys. Lett. B **348**, 331 (1995); Nucl. Phys. **A620**, 191 (1997).
295. A. Garcia, et al., Phys. Rev. Lett. **67**, 3654 (1991).
296. B. D. Anderson, et al., Phys. Rev. C **54**, 602 (1996).
297. B. A. Brown, Phys. Rev. Lett. **69**, 1034 (1992).
298. W. Trinder et al., Phys. Lett. B **459**, 67 (1999).
299. M. J. G. Borge et al., Z. Phys. **332**, 413 (1989).
300. K. Langanke and G. Martinez-Pinedo, Nucl. Phys. **A673**, 481 (2000).
301. A. Piechaczek et al., Nucl. Phys. **A584**, 509 (1995).
302. B. Blank et al., Nucl. Phys. **A615**, 52 (1997).
303. S. Czajkowki et al., Nucl. Phys. **A628**, 537 (1998).
304. V. Banerjee et al., Phys. Rev. C **63**, 024307 (2001).
305. J. C. Thomas et al., private communication.
306. F. Pougheon et al., Nucl. Phys. A **500**, 287 (1989).
307. T. Bjornstad et al., Nucl. Phys. A **443**, 283 (1985).
308. B. Blank et al., Z. Phys. **A357**, 247 (1997).
309. V. Borrel et al., Nucl. Phys. **A531**, 353 (1991).
310. G. Canchel et al., private communication.
311. D. Bazin et al., Phys. Rev. C **45**, 69 (1993).
312. H. O. U. Fynbo et al., Nucl. Phys. **A677**, 38 (2000).
313. B. Blank et al., Phys. Rev. C **54**, 572 (1996).
314. B. A. Brown, Phys. Rev. Lett. **65**, 2753 (1990).
315. K. Muto, E. Bender and T. Oda, Phys. Rev. C **43**, 1487 (1991).
316. D. J. Morrissey, et al., Nucl. Phys. **A627**, 222 (1997).
317. M. S. Pravikoff, et al., Nucl. Phys. **A528**, 225 (1991).
318. E. K. Warburton, J. A. Becker, D. J. Millener and B. A. Brown, Ann. Phys. **187**, 471 (1988).
319. W. T. Chou, E. K. Warburton and B. A. Brown, Phys. Rev. C **47**, 163 (1993). The $B(GT)$ as defined in the present work is related to the $M(GT)$ of this reference by $B(GT) = [M(GT)/1.264]^2/(2J_i + 1)$.

320. M. J. G. Borge et al., Z. Phys. **340**, 255 (1991).
321. D. Mikolas et al., Phys. Rev. C **37**, 766 (1988).
322. N. Auerbach, G. F. Bertsch, B. A. Brown and L. Zhao, Nucl. Phys. **A556**, 190 (1993).
323. B. A. Brown and K. Rykaczewski, Phys. Rev. C **50**, R2270 (1994).
324. B. A. Brown, Nucl. Phys. **A577**, 13c (1995).
325. I. Hamamoto and H. Sagawa, Phys. Rev. C **48**, R960 (1993).
326. K. Langanke and G. Martinez-Pinedo, Phys. Lett. B **453**, 187 (1999).
327. A. Klein, et al., Nucl. Phys. **A607**, 1 (1996).
328. W. F. Rogers, et al., Phys. Rev. C **62**, 044312 (2000).
329. M. Schafer et al., Phys. Rev. C **57**, 2205 (1998).
330. M. Fukuda et al., Phys. Lett. B **307**, 278 (1993).
331. P. Kappertz et al., AIP Conference Proceedings **455**, 110 (1998).
332. M. Huhta et al., Phys. Rev. C **57**, R2790 (1998).
333. K. Matsuta et al., Nucl. Phys. **A588**, 153c (1995).
334. B. A. Brown and B. H. Wildenthal, Phys. Rev. C **28**, 2397 (1983).
335. H. Okuno et al., Phys. Lett. B **354**, 41 (1995).
336. H. Ueno et al., Phys. Rev. C **53**, 2142 (1996).
337. W. Geithner et al., Phys. Rev. Lett. **83**, 3792 (1999).
338. I. Talmi, *Simple Models of Complex Nuclei*, (Harwood Academic Publishers, 1993).
339. R. F. Casten and N. V. Zamfir, J. Phys. G **22**, 1521 (1996).
340. H. Hu, et al., Phys. Rev. C **60**, 024315 (1999).
341. M. Karny et al., Nucl. Phys. A **690**, 367 (2001).